Methane Reforming on Single Atom Catalysts

Yu Tang

Submitted to the graduate degree program in Chemical & Petroleum Engineering and the Graduate Faculty of the University of Kansas in partial fulfillment of the requirements for the degree of Doctor of Philosophy

_____

Chair: Franklin (Feng) Tao

_____

Co-chair: Raghunath V. Chaudhari

_____

Michael Rubin

_____

Juan J. Bravo Suarez

_____

Kevin Leonard

Date Defended:_____

The dissertation committee for Yu Tang certifies that this is the approved version of the following dissertation

Methane Reforming on Single Atom Catalysts

_____

Chair: Franklin (Feng) Tao

_____

Co-chair: Raghunath V. Chaudhari

Date approved:

Abstract

Heterogenous catalysis is a key process in chemical conversion and energy application. The catalytic performance is determined by the structure and properties of catalytic active sites under working conditions, which are difficult to be characterized by conventional techniques. Studies of structure of a catalyst at atomic level could help to build up correlation between the catalyst structure and its corresponding catalytic performance. Then, new catalyst with better performance and long-life time could be rationally designed. In-situ/operando techniques, such as near ambient XPS, in-situ XAS and Environmental TEM, have been developed and discussed in Chapter 2 to resolve the structure and chemical state of the active sites during catalysis condition.

Methane has been an inexpensive source to provide fuels and chemicals in recent decades. It attracted much attention to catalytically convert methane to high value intermediate and chemical products. A major challenge is, how to design a catalyst which could activate C-H bond of methane effectively to from ideal intermediate compound for chemical industries. In the research work of dissertation catalysts containing singly dispersed transition metals on oxide support were designed. They effectively convert methane to syngas. Methane reforming with water and CO_2 can readily be catalyzed over Rh_1/CeO_2 catalyst, with a significantly lowered activation energy barrier compared to Rh nanoparticles supported on CeO_2. In-situ XAS and NAP-XPS reveals chemical state of Rh_1/CeO_2 catalyst. Moreover, a catalyst containing two sets of singly dispersed single metal atoms, $(Ni_1+Ru_1)/CeO_2$ was designed for methane reforming. The synergistic effect on catalytic activity between the two sets of metal cations were exhibited. Computational studies suggest that the synergistic effect is originated at that (1) the different role of Ni_1 and Ru_1in terms of activations of $CH_4$to form CO on Ni_1 site and dissociation of CO_2 to CO on Ru_1 site, respectively, and at (2) the sequential role in terms of *first* forming H atoms through activation of CH_4 on Ni_1 site and *then* coupling H atoms to formH_2 on Ru_1 site.

Acknowledgement

I would like to thank my advisor, Prof. Franklin (Feng) Tao, for his support and supervising during my graduate program. His enthusiastic and hardworking attitude is always inspiring me. I would like to thank my advisory committee, Prof. R. V. Chaudhari, Prof. Michael Rubin, Prof. Kevin Leonard and Prof. Juan Bravo-Suarez, for their valuable suggestion and discussion during my preliminary exam and comprehensive exam. I would like to acknowledge my coworkers in the research group, Dr. Luan Nguyen and Yuting Li, for their assistance and discussion in research. I also want to thank the faculties and staffs in the C&PE family at KU for their support and help during my graduate career. I would like to thank the collaborators from other universities and national labs for the exciting work we have done.

Lastly, I would like to thank my parents and Ms. Lijun Chen for their unconditional love and support for my study.

Table of contents

List of Figures

Figure 5.4 Catalytic performance of $Ce_{0.95-x-y}Ni_xRu_yO_2$ catalysts for dry reforming of CH_4. (a) conversion of CH_4, (b) selectivity to product of H_2, and (c) H_2/CO ratio.

Figure 5.5 the Arrhenius plot of the activation energy barrier in term of the rate to produce (a) H_2 and (b) CO catalyzed by the $Ce_{1-x-y}Ni_xRu_yO_2$ catalysts: (blue) $Ce_{0.95}Ni_{0.025}Ru_{0.025}O_2$, (black) $Ce_{0.95}Ru_{0.05}O_2$ and (red) $Ce_{0.95}Ni_{0.05}O_2$.

Figure 5.6 Turnover frequency (TOF) of reforming CH_4 with CO_2 in term of hydrogen production.

Figure 5.7 Ce3d, O1s, Ru3p, and Ni2p photoemission features from AP-XPS studies of $Ce_{0.95}Ni_{0.025}Ru_{0.025}O_2$ during reforming CH_4 with CO_2: (a1, b1, and c1) before catalysis, (a2, b2, and c2) 450^{o}C and (a3, b3, and c3) 550^{o}C. The reactant mixture is composed by 0.5 Torr CO_2 and 0.5 Torr CH_4.

Figure 5.8. Operando studies of $Ru_{0.025}Ni_{0.025}Ce_{0.95}O_2$ during catalysis and reference samples (Ni foil, Ru foil, NiO powder and RuO_2 powder) using X-ray absorption spectroscopy (XANES and EXAFS) and corresponding Fourier transformed radical distribution function of Ru K edge and Ni Kedge. (a) Energy space of Ru K edge of $Ru_{0.025}Ni_{0.025}Ce_{0.95}O_2$ and Ru foil reference; (b) energy space of Ni K edge of $Ru_{0.025}Ni_{0.025}Ce_{0.95}O_2$ and Ni foil reference. (c) Experimental (black) and fitting (red) **r**-space spectra of Ru K edge of $Ru_{0.025}Ni_{0.025}Ce_{0.95}O_2$. (d) Experimental (black) and fitting (red) **r**-space spectra of Ni K edge of $Ru_{0.025}Ni_{0.025}Ce_{0.95}O_2$. (e) r-space spectrum of reference sample Ru foil. (f) r-space spectrum of reference sample Ni foil. (g) r-space spectrum of reference sample NiO. (h) r-space spectrum of reference sample RuO_2. All r-space spectra are shown without phase correction. (i)Coordination environments of Ni_1 and Ru_1 atoms of $Ru_{0.025}Ni_{0.025}Ce_{0.95}O_2$ during catalysis.

Figure 5.9 The most stable surface structure representing surface of $Ru_{0.025}Ni_{0.025}Ce_{0.95}O_2$ during catalysis. (a) Top view of CeO_2 (110) anchored with a Ni_1 atom. (b) Side view of CeO_2 (110) anchored with the Ni_1 atom. (c) Top view of CeO_2 (110) anchored with a singly dispersed Ru_1 atom. (d) Side view of CeO_2 (110) anchored with the singly dispersed Ru atom. (e) The marked neighbor atoms (black arrows) coordinated with Ni_1 site. (f) The marked neighbor atoms (black arrows) coordinated with Ru_1 site. Ce, Ni, and Ru are shown in yellow, blue, and green, respectively. Red balls stand for oxygen atoms. These notations are used throughout this work. It is the most stable surface among four optimized surface structure with different binding environment of Ni_1 and Ru_1 atoms.

Figure 5.10. Top views and side views of transition state geometries of CH_4 activation and intermediate structures of formed CH_3 and H on Ni_1 and Ru_1 sites on CeO_2. (a and b) Top and side views of transition state geometries of CH_4 activation on Ni_1. (c and d) Top and side views of transition state geometries of CH_4 activation on Ru_1. (e and f) Top and side views of intermediate geometries of CH_3 and H formed on Ni_1 site. (g and h) Top and side views of intermediate geometries of CH_3 and H formed on Ru_1 site.

Figure 5.11. Top views and side views of transition state geometries of CH_3 dehydrogenation or CH_3 oxidation on Ni_1 or Ru_1 site on CeO_2. (a and b) Top and side views of transition state geometry of CH_3 dehydrogenation on Ni_1. (c and d) Top and side views of transition state geometry of CH_3 oxidation on Ni_1. (e and f) Top and side views of transition state geometry of CH_3 dehydrogenation on Ru_1. (g and h) Top and side views of transition state geometry of CH_3 oxidation on Ru_1.

Figure 5.12. Top views and side views of transition state geometries of CO_2 dissociation and the final state geometries on Ni_1 and Ru_1 sites on CeO_2. (a and b) Top and side views of transition state geometries of CO_2 dissociation on Ni_1 site. (c and d) Top and side views of transition state geometries of CO_2 dissociation on Ru_1 site. (e and f) Top and side views of final state of CO_2 dissociation on Ni_1 site. (g and h) Top and side views of final state of CO_2 dissociation on Ru_1 site.

Figure 5.13. Top views and side views of transition state geometries of hydrogen coupling on Ni_1 site (a and b) and on Ru_1 site (c and d).

Figure 6.1. Evolution of photoemission feature of (a) Co 2p and (b) O 1s of CoO surface phase during CO oxidation in 0.4 Torr CO and 1.0 Torr O_2 in the temperature range of 60-220 ºC. (a1, b1) 60 ºC, (a2, b2) 100 ºC, (a3, b3) 140 ºC, (a4, b4) 180 ºC, and (a5, b5) 220 ºC.

Figure 6.2. Schematics showing the evolution of as-synthesized Co_3O_4 nanoparticles (a), reduced at 250 ºC in 5%H_2/Ar for 2 hrs (b), and then used for CO oxidation in the temperature range of 60-140ºC (c), followed by CO oxidation in the temperature range of 160-200ºC (d).

Figure 6.3. TEM studies of Co_3O_4 before and after a treatment including both a reduction in 50 mL/min of 5%H_2/Ar at 250 °C for 2 hrs to form a CoO surface phase and then CO oxidation on the formed CoO in the mixture of 20 mL/min of 5%CO/Ar and 50 mL/min of 5%O_2/Ar at 140 °C. (a) and (b) BFTEM image and SAED pattern of Co_3O_4 before reduction in 5% H_2 at 250ºC. (c) and (d) BFTEM image and SAED pattern of cobalt oxide which experienced two steps: reduction of Co_3O_4 at 250ºC in 5% H_2 for forming CoO surface phase and then catalysis of CO oxidation at 140ºC on the CoO.

Figure 6.4. Coexistence of surface phase CoO and bulk phase Co_3O_4 in catalyst nanoparticles (formed from two steps: reduction of Co_3O_4 nanoparticles in 5% H_2 at 250ºC for two hours and then CO oxidation at 140ºC) during CO oxidation with 20 mL/min of 5%CO/Ar and 50 mL/min of 5%O_2/Ar at 140 ºC. (a) The unprocessed HRTEM image and corresponding FFT (a inset) of catalyst nanoparticles. (b) The bandpass filtered FFT (inset) and iFFT of image of catalyst nanoparticle in (a). (c) iFFT image of the FFT (c inset) that has been masked to remove the (200) planes of CoO to remain only the fringes of Co_3O_4 phase. (d) iFFT image of the FFT (inset) in which (400) of Co_3O_4 planes were masked to remain only fringes of CoO.

Figure 6.5. Evolution of reactant CO and products CO_2 during CO oxidation (0.4 Torr CO + 1 Torr O_2) on CoO (formed by reduction of Co_3O_4 in 5% at 250ºC) in the temperature range of 60-220ºC when the surface of CoO was simultaneously monitored with AP-XPS. The partial pressures of CO and CO_2 were measured with on-line mass spectrometer. It is noted that these observed partial pressures in the UHV chamber of mass spectrometer are much lower than the actual

pressure in the reaction cell since only a tiny amount of gas near to surface of catalysts in the reaction cell was sampled to another UHV chamber where the mass spectrometer was installed.

Figure 6.6. Arrhenius plots of CO oxidation over CoO (formed by reducing Co_3O_4 in 5% H_2 at 250ºC) at 80-120 ºC and Co_3O_4 formed from CoO during catalysis at 160-200 ºC. Pretreatment: 5%H_2/Ar, 250 ºC, 2 h. Reaction condition: 2.8 mg of Co_3O_4 nanoparticles pellets + 0.1 g of quartz sands, 10 mL/min of CO+O_2 (CO:O_2=1:2.5) at 80-120 ºC, 80 mL/min of CO+O_2 (CO:O_2=1:2.5) at 160-200 ºC.

Figure A1 experiment setup to measure catalytic activity and selectivity for methane reforming. From left to right: on-line GC, fixed bed reactor, mass flow controller units and data processing PC.

Figure B1 deconvoluted Ce3d spectrum of Rh_1/CeO_2 catalyst. (a) in UHV, (b) reduced at 300ºC, in steam reforming at (c) 500 ºC and (d) 650ºC, in dry reforming at (e) 500ºC and (f) 650ºC.

Figure C1 stability test of methane reforming catalyzed by $(Ni_1+Ru_1)/CeO_2$ catalyst.

Figure C2 carbon balance of methane reforming catalyzed by $(Ni_1+Ru_1)/CeO_2$ catalyst.

List of Tables

Chapter 1 Introduction

1.1 Significance of fundamental understanding of catalysis in designing new and efficient catalysts

Heterogenous catalyst is the essential key for industrial chemical conversion and energy application. Defined by Ostwald, a catalyst accelerates a chemical reaction without affection the reaction equilibrium.[1-2] The chemical reaction rate is readily boosted by participating of catalyst compared with the case of no catalyst. It is achieved by reducing the reaction activation energy barrier, in other words, changing the reaction pathway, as demonstrated in the **Figure 1.1**. Thus, the reaction mechanism with catalyst participating is different from the collision of free molecules which is the case of no catalyst.

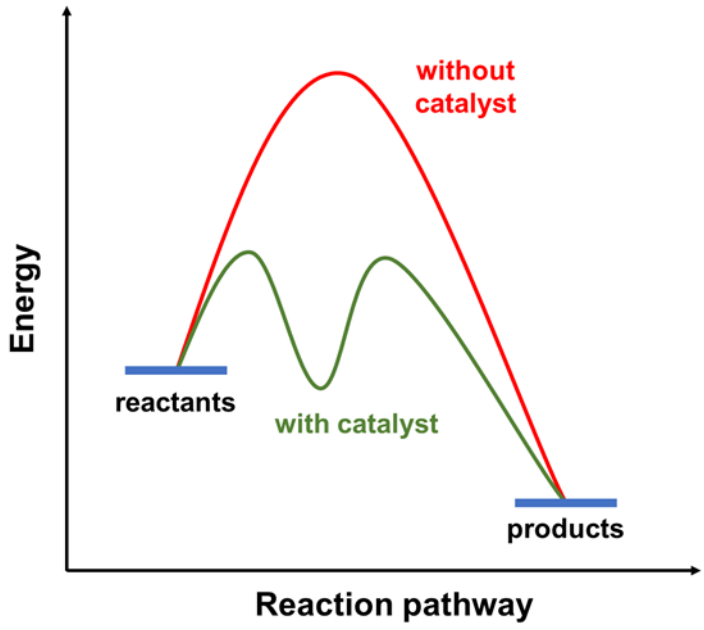

Figure 1.1 scheme of energy profile during catalysis with (green) and without catalyst (red).

In the fundamental understanding, heterogenous catalysis is a surface phenomenon. Reactants molecules are absorbed on the surface layer atoms from the catalyst firstly, then convert to product via intermediates or transition states at desired temperature and pressure; finally, the product molecules desorb and leaves the surface of catalyst. Fundamental studies of surface science, such as the adsorption, desorption, and the reactivity of surface adsorbates, help to the understand of heterogenous catalysis in atomic level.[3-4]

Mechanism for the heterogenous catalysis on the model surface has been deeply discussed. It always begins with the adsorption of reactions in term of surface coverage as the function of the partial pressure of reactions in the surrounding environment, which can be deduced from the Langmuir equation. Then, in a typical reaction such as $A + B = C + D$ (the stoichiometric coefficients are omitted), the reactions on the surface adsorbates follows three mechanism, which are known as Langmuir-Hinsholwood mechanism, Rideal-Eley mechanism and Mars-Van Krevelen mechanism.

In the Langmuir-Hinsholwood mechanism, both reactants A and B adsorbed on the surface of catalyst before undergoing surface reaction. The adsorption kinetics of both reactants influence the following reaction rate. Both adsorption rate should be evaluated for the catalysis study. For the Rideal-Eley mechanism, one reactant, molecule A, adsorbed on the surface of catalyst, and then another reactant, molecule B, attacks the adsorbed A on the surface to perform the catalysis reaction. Thus, only the surface adsorption of one reactant influence the reaction kinetics. In the third mechanism, Mars-Van Krevelen mechanism, one reactant A adsorbs on the surface of catalyst, and then consume the reactive species from the surface of catalyst. Another reactant compensate the consumption of catalyst by another surface reaction,[5] which is usually reported for the oxidation reaction over oxide-based catalyst[6-7] and electron transfer process[8].

Historically, heterogenous catalysis was described as a black-box due to the complexity of the catalytic process and the difficulty to study it.[9] However, it's essential to understand the catalytic mechanism from the atomic level since the surface reaction mechanism determines the catalyzed reaction pathway. Only in this way, people can understand how does a catalyst work. The insights obtained from the fundamental study of the catalytic mechanism help people to design catalyst rationally, which has better catalytic performance, longer life time and lower cost.

1.2 Surface structure at atomic scale: essential component in fundamentally understanding catalysis

Not every atom from the catalyst participates a catalytic reaction. Those atoms embedded deeply in the bulk materials are always fully coordinated with the surrounding atoms, making them hard to be accessed by the reactant molecules. As the result, the contribution from the bulk atoms to catalytic performance is neglectable. Only the first layer atoms on the surface interacts with the reactants and then participate catalytic pathway directly. The top layer atom determines the catalytic performance.[4] It's also reported that although sub-surface layers atoms don't interact with reactants directly, they can influence the electronic properties of the top layer atoms and then consequently influence the catalytic properties.[10] In short, the catalytic performance is majorly dominated by the a few layers atoms on the surface of the catalyst. Understanding of the structure and properties of the atoms of surface layers is essential.

First of all, surface atoms are not coordination saturated compared with the atoms in bulk. The coordination unsaturation of the surface atoms makes them much more active. For example, the coordination number of metal atoms, such as Pt, in face centered cubic structure is 12, which means

there are 12 equivalent atoms coordinate with center atoms. However, coordination number (CN) of atoms on the surface layer is usually lower than 12. CN of Pt atoms on the (100) surface is 8, CN of Pt on (111) surface is 9. The un-coordinated bonds increase the total energy of the surface, making the surface tender to be thermodynamically unstable, in other words, more reactive. The elevated surface energy could be compensated by adsorption of molecules. Thus, it can de deduced that the coordination unsaturation status impacts the adsorption process, then influence the catalytic performance consequently.[11-12] Secondly, the surface element composition is another key factor since the binding of adsorbates on different element are expected to be different. By tuning the surface element composition, the surface properties such as electron density, redox properties, and binding force with the adsorbates can be controlled precisely. Bimetallic catalysts,[13-15] such as alloy and intermetallic, have been reported for the controllable catalytic performance in thermal catalysis and electro catalysis.

1.3 Hypothesis: breaking continuously packed site to discontinuously packed site

Catalytic elementary reaction occurs on active sites in the case of heterogeneous catalysis. Typically, a catalytic site accelerates the reaction by lowering the activation barrier through creating a new reaction pathway. In most cases, there are two reactants A and B in a catalytic reaction. In a Langmuir-Hinshelwood mechanism, which most reactions of heterogeneous catalysis reactions follow, the first step of a catalytic reaction is the chemisorption of reactant molecules on catalyst surface, which could happen by dissociative or molecular adsorption. In dissociative adsorption, one intramolecular chemical bond is cleaved; in terms of molecular adsorption, molecular structure remains intact although its geometry is typically deformed. In

some cases, such as CO oxidation, only one reactant such as oxygen molecule needs to dissociate upon adsorption. In many cases, molecules of all reactants of a catalytic reaction must dissociate before these dissociated species (also called derivatives of reactants) could couple to form a series of intermediates eventually leading to the reaction product molecules; for instance, both ethane and oxygen molecules in oxidative dehydrogenation (ODH) of ethane need to be dissociated into derivatives before these dissociated species can couple to form intermediates toward formation of final products.[16-17]

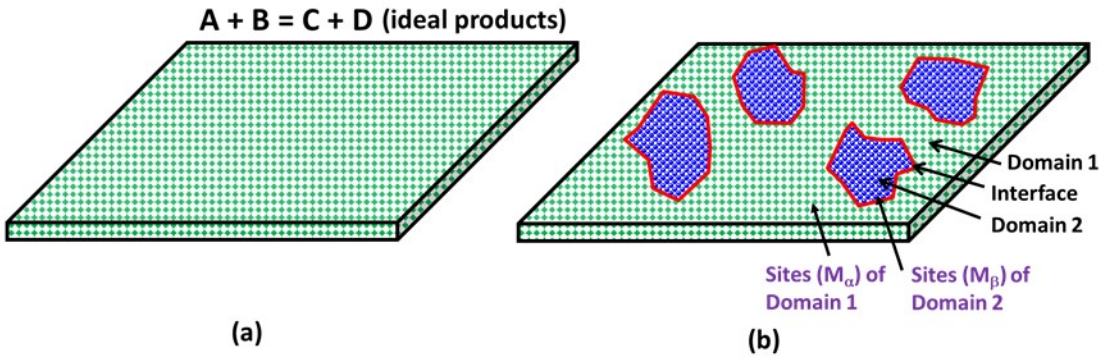

Figure 3.2 Schematics of two different types of catalysts. (a) Surface of a catalyst consisting of one type of sites. (b) Surface a catalyst consisting of two types of different domains; each domain provides one type of sites.

Compared with homogenous catalyst, heterogenous catalyst usually exhibits lower selectivity to product since the active domain are not uniform in heterogenous catalyst as shown in **Figure 1.2b**. The catalytic domain of M_β may be different greatly in the particle size, shape and surface structure. It will further make the catalyst complicated.[11] Meanwhile, only a limited portion of atom M_β is exposed to the reactant environment, which makes the utilization of M_β is not efficient. The cost of the catalyst will be increased if M_β is a noble metal. Singly dispersed catalyst, which refer to the isolated catalytic cations on support as shown in **Figure 1.3b**, has been widely

studied from 2012.[18] The unique advantages of singly dispersed catalyst make it a promising star for both scientific research and industrial application.[19-21] The primary advantage is the highly isolated catalytic sites. The electronic state and properties of singly dispersed sites are unique and different from the nanoparticle counterpart. Secondly, the singly dispersed catalytic sites are highly uniform in the atomic structure. The selectivity is expected to be much better than the catalyst containing various catalytic domain. *Inspired by the progress, herein we propose to design a catalyst containing singly dispersed transition cations on support for the methane reforming to produce hydrogen as the first hypothesis.* The singly dispersed catalytic sites is designed to activate the C-H bond of methane but avoid over oxidation as discussed in chapter 3 and 4.

In principle, the same type of sites (such as Pt atoms of a surface of a catalyst particle) can activate both reactants A and B such as dissociating O_2 and chemisorbing CO. In most cases, however reactants A and B of a catalytic reaction exhibit different adsorption energies and activation barriers for dissociation on the *same type of active sites of a catalyst which only has one type of active sites* (**Figure 1.2a**). Thus, the adsorptions of different reactants are competitive. In most cases, one of the reactants is preferentially chemisorbed on the catalyst surface. A potential consequence is that the other reactants cannot be efficiently chemisorbed if their adsorption energies are lower or of their activation barrier of chemisorption of the reactant is higher than those of the preferentially adsorbed reactant, respectively. As a result, such a competitive adsorption and binding of different species on the same type of sites prevent the catalyst surface from offering high activity and selectivity for formation of ideal products. In other words, if chemisorption of one of the species (either reactant molecules or its derivative) is obviously stronger than other reactants or their derivatives, it could poison the catalyst active site at certain temperature range when the preferentially bound species cannot desorb. Thus, to provide different sites for the two

reactants, one possibility is to offer two types of domains that would coexist on the surface a catalyst (**Figure 1.2b**). In many cases, the two components of a "bi-functional catalyst" (**Figure 1.2b**) are metal and oxide. On such a bi-functional catalyst, typically metal nanoclusters are supported on oxide particle, or oxide nanoclusters on metal (called reverse catalyst). For example, in the case of WGS, CO molecules are adsorbed on sites of a metal domain and H_2O molecules on sites of a reducible oxide which typically are oxygen vacancies; the chemisorbed reactant molecules such as CO of WGS or dissociated species such as OH derived from H_2O molecules couple at the interface of the two domains toward formation of product molecules.[22-23] In the case of a catalyst consisting of two domains (**Figure 1.2**), it is generally acknowledged that the coupling of these active species is performed at the interface of the two types of domains (typically oxide and metal).

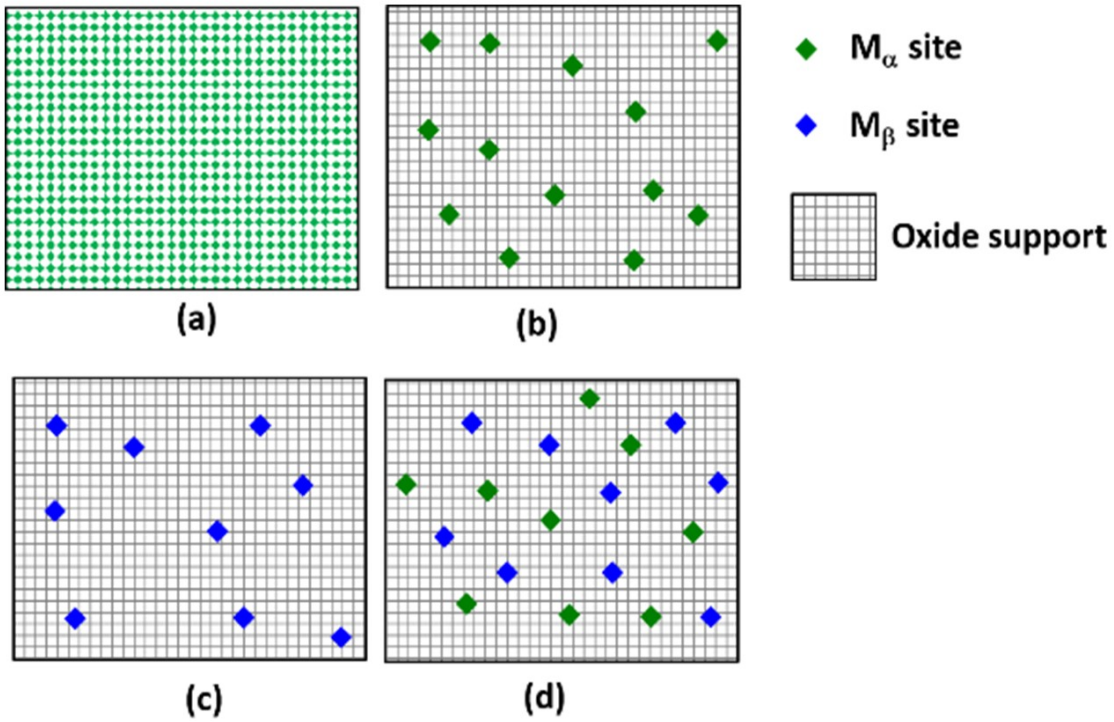

Figure 1.3 Schematic of surface of catalysts. (a) Oxide surface with exposed oxygen anion (not shown) and M_α cations (green square); on this surface M_α cations are "continuously" packed in a pattern of -M_α-O- M_α-O- M_α-O-. (b) Catalyst surface with singly dispersed M_α cations (green squares) anchored on an oxide support (black mesh). (c) Schematic of M_β cations singly dispersed on oxide support. (d) Schematic of M_α+ M_β /oxide on which both M_α (green square) and M_β (blue square) are singly dispersed on oxide support.

In many cases, however, only one domain and one type of sites (**Figure 1.2a**) are provided for dissociating molecules of reactants A and B of a catalytic reaction before they can couple to form an intermediate and lead to products. A self-competition dissociation or adsorption is then obvious. For example, Pt surface can dissociate molecular oxygen at room temperature or even a lower temperature.[24] As binding energy of CO molecules on Pt surface is larger than oxygen atoms, the strong adsorption of CO largely occupy most sites of Pt surface and thus prevent it from dissociating molecular O_2 on Pt surface at room temperature. When the mixture of CO and O_2 is introduced on a Pt catalyst, the surface is mostly covered with CO molecules. There are very few sites available for dissociating molecular O_2 and thus no CO_2 can form at room temperature.

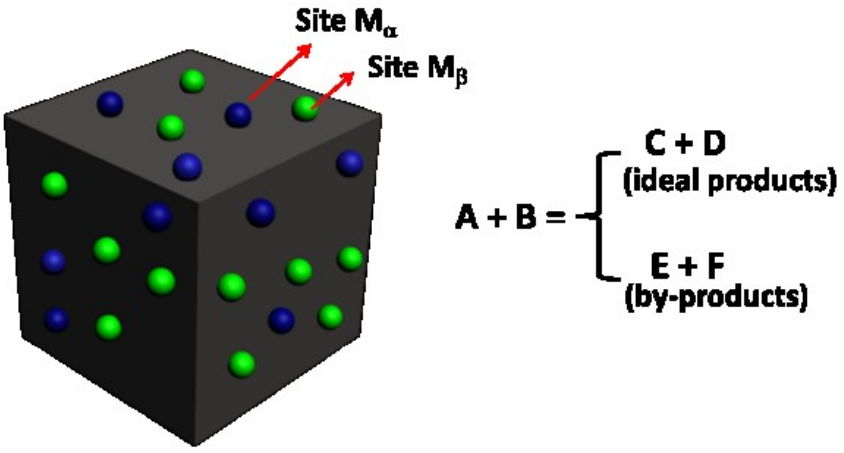

Figure 1.4. Schematic of coexistence of two type of sites (M_α and M_β) which chemisorb reactants A and B, respectively.

To avoid the self-poisoning effect of one of the reactants of a catalytic reaction, *one hypothesis is to immobilize of two different types of single sites (M_α responsible for chemisorbing molecule A and M_β for chemisorbing molecule B), on the same surface of a catalyst particle* ***(Figure 1.3d)***. It could result in a synergistic effect between the two sites in a catalytic cycle and thus enhance catalytic activity and selectivity for this reaction on such a catalyst, compared to cases with only sites, M_α or M_β. We termed such a catalyst "catalyst of dual single sites". Here a single site, M_1O_n, is defined as a site formed by a metal cation boning to oxygen atoms, but without neighboring M-O units; it is termed to distinguish from the continuously packed …M-O-M-O… structure in metal oxide catalysts. **Figures 1.4** schematically present the continuously packed M-O bonds on the surface of a metal oxide and the isolated single site (M_1O_n) anchored on a substrate, respectively. As single sites M_α and M_β (**Figure 1.3** and **1.4**) will take care of the dissociation of molecules A and B, respectively, dissociations of A and B will be performed spatially separately but temporally simultaneously on the surface of dual single site catalysts. In cases where site M_α could dissociate both A and B, the internal competition of A and B on site M_α will result in a preferential interaction with A on the M_α; in this way, B will not be able to dissociate on M_α site. Parallel to a catalyst with only M_α sites, a catalyst with only M_β sites will preferentially dissociate molecules of reactant B. However, integration of both sites M_α and M_β on the same substrate of a catalyst (**Figure 1.3** and **1.4**) will allow reactants A and B to dissociate on M_α and M_β simultaneously within minimal competition and thus the reaction can be performed without any "poisonous effect" on such a catalyst of dual single sites. We expect that such a catalyst consisting

of M_α and M_β on a support surface will exhibit definitely higher selectivity for the same catalytic reaction than catalysts containing only M_α or M_β.

1.4 Catalytic methane activation

Methane is one of the major fuel resources on Earth. As the discovery of shale gas, annual production of methane is increasing, while the price keeps going down. Thus, it attracts more and more attention in the utilization of methane for chemical intermediate production and energy application. However, one primary challenge in catalytic conversion of methane is the difficult to activate C-H bond in methane molecules. It requires 439 kJ/mol to dissociate the first C-H bond in *sp3* hybridization from methane, while the energies needed to dissociate the other C-H bonds of methane are even lower. The high dissociation energy of C-H bond needs harsh reaction condition such as high temperature, which would very likely to dissociate the rest C-H bond consequently. Thus, the precise control on the activation of molecule methane is necessary, otherwise it would undergo deep oxidation, or combustion of methane, to produce CO_2 and H_2. Numerous efforts were dedicated to the selective activation of methane via heterogenous and homogenous catalysis.[25-26] An ideal catalyst for methane conversion should satisfy one or more following expectations 1) it should be readily active in methane conversion, while high selectively is also favored; 2) it can operate at lower reaction temperature to reduce energy consumption and slow down the deactivation of the catalyst; 3) the cost of the catalyst should be reasonable.

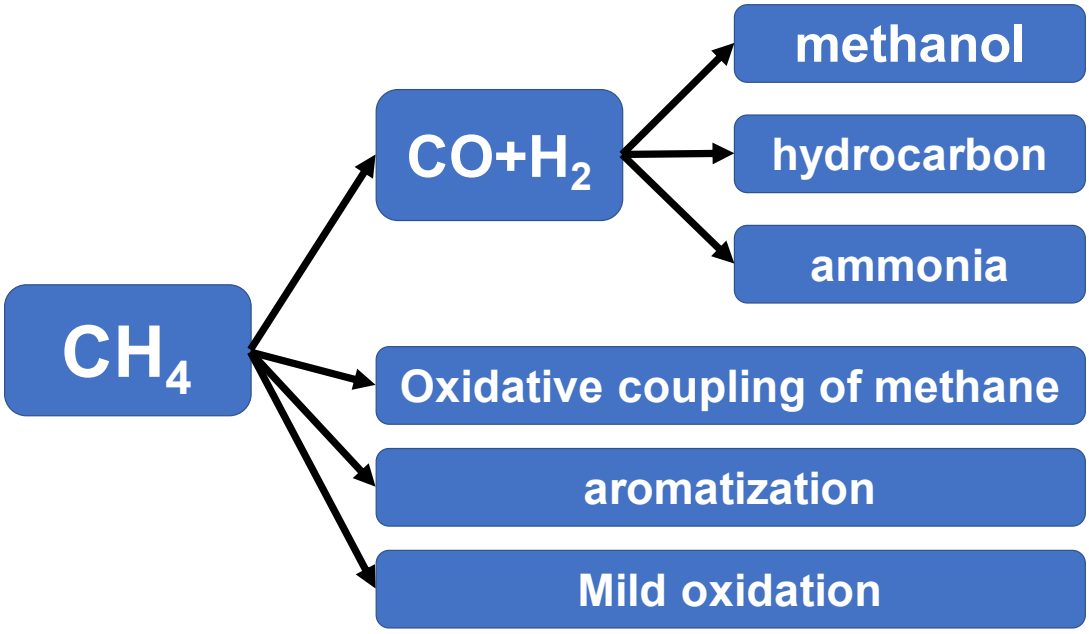

Figure 1.5 scheme of methane conversion processes.

Generally, the proposed heterogenous catalysis strategies include in-direct conversion of methane and direct conversion of methane as shown in **Figure 1.5**. For the in-direct conversion, methane is reformed to produce the mixture of $CO+H_2$. The mixture is also known as syngas, which is an important industrial chemical intermediate to for other process, such as methanol-to-olefin,[27-28] Fisher-Tropsch synthesis[29-31] , aromatics[32-34] and ammonia synthesis.[35] Methane can be reformed by water, CO_2 and O_2, while the process is usually performed at high temperature. The reforming processes consumes significant energy. On the other hand, direct conversion of methane refers to oxidative coupling,[36-41] aromatization,[42-47] and mild oxidation.[48-52] These studies represent significant progress has been made and all strategies are promising for the application. However, developing novel catalyst is still required.

Chapter 2 Experiment methods

2.1 Ex-situ characterization and techniques

2.1.1 X-ray photoelectron spectroscopy in vacuum

X-ray photoelectron spectroscopy, which is also known as Element Surface Chemical analysis (ESCA), is developed on the photoelectron effect, which refers to a photoelectron could be 'knocked out' from a subshell of an atom when the atom is irradiated by incident photon flux.[53-54] By analyzing the kinetics energy of the leaving photoelectron, the binding energy of the electron could be obtained. The energy equation of photoelectron effect is written as:

$$hv = E_b + E_k + \phi$$

where hv is the energy of incident photon, ϕ is work function, E_b is the binding energy of the subshell and E_k is the kinetics energy of leaving photoelectron. Experimentally, soft X-ray and UV light are used as the photon sources in photoelectron spectroscopy, which are generally known as X-ray photoelectron spectroscopy (XPS) and Ultraviolet Photoelectron spectroscopy (UPS), respectively. By using soft X-ray source such as Mg Kα and Al Kα, people can collect photoelectron from subshell of an atom, which could provide information such as the chemical state and local structure of the atoms.[53-54]

As a photon-in and electron-out technique, XPS has quite high surface sensitivity to study surface chemistry of samples. This is due to short mean free path of photoelectron when travelling through sample in condensate state. Mean free path of electron is defined as the average moving distance of electron between collisions. For the photoelectron with kinetics energy of 100-1400 eV travelling in solid phase sample, the mean free path is about a few nanometers. The signal intensity

of photoelectron *I(x)* after travelling through the sample with profile distance ***x*** is given by the equation:

$$I(x) = I_0 * e^{-x/\lambda}$$

where λ is the mean free path of the photoelectron, and I_0 is the initial intensity of photoelectron. Clearly, the intensity of photoelectron decreases exponentially when ***x*** increases. Moreover, the total photoelectron signal collected from the surface of sample is available from the integration of the above equation:

$$I = \int_{x=0}^{x=infinite} I(x)dx = \int_{x=0}^{x=infinite} I_0 * e^{-\frac{x}{\lambda}}dx = \lambda * I_0$$

Then, the signal contribution from the depth between x_1 and x_2 over total signal is defined as below:

$$P = \frac{\int_{x1}^{x2} I(x)dx}{\int_0^{infinite} I(x)dx} = e^{-\frac{x1}{\lambda}} - e^{-\frac{x2}{\lambda}}$$

In the case of x_1=0, the signal contribution from the surface to profile distance x_2 is deduced as below equation. In a typical case when x_2=3λ, the signal portion is 95%.

$$P = \frac{\int_0^{x2} I(x)dx}{\int_0^{infinite} I(x)dx} = 1 - e^{-\frac{x2}{\lambda}}$$

In other words, the surface layer of thickness of 3λ contributes to 95% of the total XPS signal. Thus, XPS is a very surface sensitive technique. Since most of catalysis processes occurs on the surface of catalyst, this unique advantage help people to focus in the surface chemistry information from catalyst.

In photoelectron spectroscopy, the binding energy measured in a wide range spectrum contains all the characteristic features of surface elements. Qualitatively information such as the element composition of the sample is available from wide scanning of the photoelectron spectroscopy. This survey scan provides the general chemical information of the sample.

More quantitative information is feasible from zoom-in scan of photoelectron spectroscopy. It's also known as the high-resolution spectrum of the most intensive features of elements, such as *2p* feature for *3d* transition metal, *3d* feature for *4d* transition metal and *4f* feature for *5d* transition metal. Due to shielding effect, the local electron density can influence the apparent binding energy of the photoelectron. Atoms at higher oxidation state will exhibit higher binding energy due to lower electron density. Thus, people can analyze the chemical state of the target element from the shift of binding energy in XPS. It's also possible to tell the target element coordination environment by comparing with reference database. Currently, there is a few databases summarized the XPS data from common samples.[55]

The relative surface atomic ratio of the sample is another quantitative information available from XPS. The intensity of photoelectron (*I*) is given by equation below, where ***n*** is the surface atom number in unit volume and ***S*** is the surface sensitivity factors.[55]

$$I = n * S$$

Then the surface atomic ratio between element 1 and element 2 is given by equation below. It could also be used to calculate the ratio of a specific component in the total photoelectron feature. As a typical example, the ratio of Ce^{3+} over all surface Ce species could be obtained from the deconvoluted Ce*3d* spectrum. The components of u0, v0, u1 and v1 are assigned to Ce^{3+} while the

components of u, v, u2, v2, u3 and v3 are assigned to Ce^{4+}.[56-58] Then the surface Ce^{3+} ratio is derived from the corresponding area ratio.

$$\frac{n_1}{n_2} = (\frac{I_1}{S_1})/(\frac{I_2}{S_2})$$

2.1.2 X-ray absorption spectroscopy

X-ray absorption spectroscopy (XAS) is a widely used technique to characterize solid material. It reveals the chemical state, electronic state and local coordination state of the target atoms.[59] It is a plot of the absorption coefficient of the sample in term of the X-ray photon energy. The spectrum feature includes an absorption edge jump and the consequently oscillation. The mechanism of XAS fine structure was not understood until 1970s, which was proposed by Sayers, Stern and Lytle.[59-62]

By absorption of an X-ray photon, one core-shell electron is excited and then leaves the atom in the form of photoelectron. A sharp absorption edge jump in the XAS spectrum is observed when the energy of incident X-ray photon matches with the binding energy of the core level electron. The leaving photoelectron behaviors the wave properties and then could be scattered by surrounding atoms and finally interferences with the original X-ray photons, either constructively or destructively. The oscillation feature after absorption edge is formed by the combination of the constructive and destructive interferences.[59-63]

XAS spectrum is generally discussed in two region, which are X-ray absorption near edge structure (XANES) and extended X-ray absorption fine structure (EXAFS).[64] XANES refers to the fine structure of the edge jump and until ~100 eV above the absorption edge, while EXAFS focus on

oscillation feature after XANES region and until ~1000eV above the edge. The information deduced from the XANES and EXAFS are assigned to different aspects of the absorption atoms.

In the XANES spectrum, the main feature is the edge jump of the absorption coefficient, which is directly correlated with the excitation of a core shell electron to higher unoccupied orbitals. Similar to the chemical shift in the binding energy of XPS, the photon energy of edge jump is determined by the electron density on the atom. The energy of the edge upshifts when the atom is at higher oxidation state and lower electron density. As the shielding effect influences more to the excitation of core shell electron than subshell electron, the chemical shift of XAS edge is usually greater than the binding energy in XPS.[55, 65] Thus, XAS is more sensitive in quantitative analysis of the chemical state change and electron density different of the sample. Any subtle change of the element of interested can be captured by XANES.[66] Spectrum feature of the edge jump is mainly contributed from the electric-dipole allowed transitions ($\Delta l=\pm 1$), such as $1\boldsymbol{s}\rightarrow(n+1)\boldsymbol{p}$ in K edge, while the selection rule forbidden transition is also possible to be detected in the form of a weak pre-edge, which is $1\boldsymbol{s}\rightarrow n\boldsymbol{d}$ for K edge if there is ***p-d*** hybridization.[59, 61-62] Thus, by comparing the XANES spectrum of the sample with the reference material, more detailed information about the coordination geometry, the unoccupied state and orbital hybridization of the absorption atoms are expected.[63]

On the other hand, EXAFS focus on the oscillation feature which is usually in the region of 100-1000 eV above the absorption edge. It's correlated to the excitation of a core-shell electron to continuum. The oscillation feature is influenced by surrounding coordination atoms. So, the local coordination information, such as the distance $\boldsymbol{R}$, coordination number $\boldsymbol{N}$ and disorderness σ^2 can be obtained from the resolving of the oscillation spectrum. The EXAFS equation is given as below.

The spectrum is considering the overall signal as the summation of interferences from all coordination pathway.

$$\chi(k) = \sum_i \frac{N_i * S_o^2 * f_i(k) * e^{-\frac{2*R_i}{\lambda(k)}} * e^{-2*k^2*\sigma_i^2}}{k * R_i^2} * \sin[2kR_i + \delta_i(k)]$$

In the general data processing protocol,[60, 65] the oscillation of the EXAFS is firstly converted to ***k***-space, and then Fourier transformation is performed to get the ***r***-space spectrum. The ***r***-space spectrum is also known as the radical function of EXAFS, whereas the peak component in ***r***-space is corresponding to nearby coordination shell. It's necessary to point out that the distance of the peak in the ***r***-space plot is usually 0.3-0.5 Å shorter than the authentic coordination distance, which is brought by the phase correction term $\delta_i(k)$ in the EXAFS equation. The ***r***-space spectrum of EXAFS could be further analyzed and fitted to resolve the coordination information.[60, 65]

Notably, XAS analyze all the absorbing atoms in the whole sample to produce the spectrum. In other words, XAS is not a surface sensitive technique but a bulk technique. This surface insensitively feature limits the application of XAS in catalytic study, particularly for the low dispersion catalyst, such as the catalyst containing large domain (> 10 nm) of active species. The information extracted from XAS need to be carefully analyzed since the signal from surface a few layers of atoms is always mixed with all the bulk atoms in the same. On the other hand, single atom dispersed catalyst[18, 49, 67] is one kind of 'perfect' samples to be studied by XAS as all the atoms of active species are exposed on the surface of the catalyst. All the information obtained from XAS are contributes to the surface atom exclusively. As the advance of single atom catalyst, XAS has becoming one of the essential characterization techniques for catalysis community.[19, 21, 64]

2.1.3 Electron microscopy

The local structure of a real catalyst is usually very sophisticated due to the complicity of the material. It's necessary but challenge to build up the local structure model of catalytic active sites in atomic scale. Among those techniques, electron microscopy could capture the image of material up to sub-Angstrom resolution, making it a powerful tool in the characterization of catalyst.

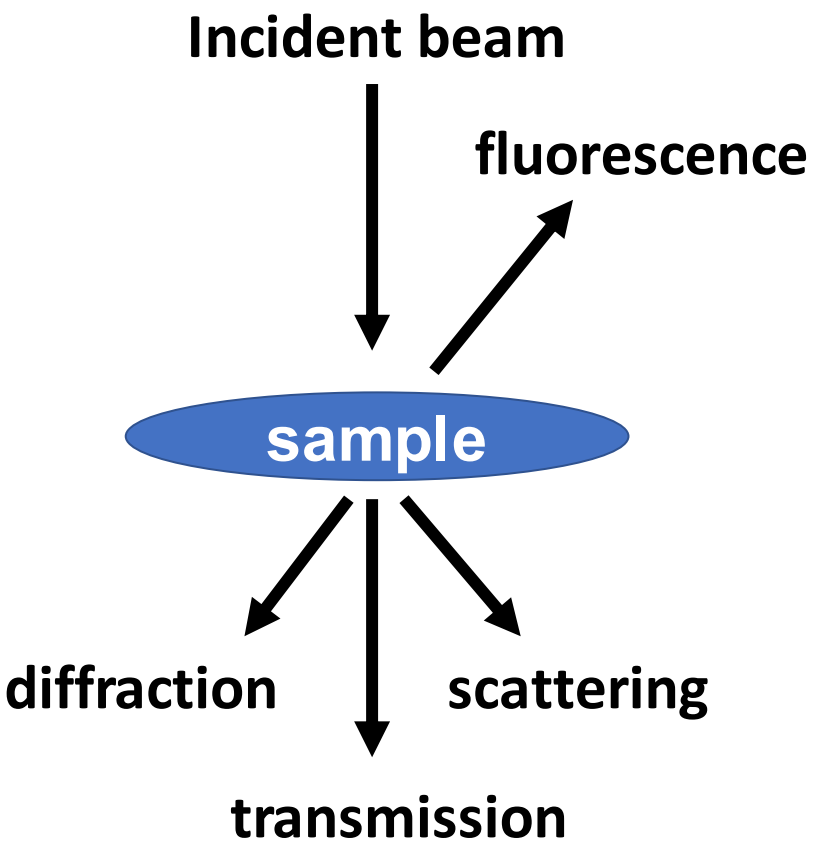

Figure 2.4 demonstration of interactions between incident electron beam and sample.

In electron microscopy, an electron beam is accelerated by high voltage and then hit on the solid sample. multiple interactions occur between electron beam and sample as shown in **Figure 2.1**.

Firstly, Elastic scattering between indecent electron and sample atoms changes the moving direction of electron. Then the transmission pattern of electron beam will change consequently. This is the general principle of transmission electron microscopy (TEM). Images captured from transmission mode is usually known as the bright field TEM (BF-TEM).

Secondly, the incident electron beam can be diffracted by the ordered crystal structure as shown in **Figure 2.1**. Diffraction patterns follow Bragg equation. By collecting the diffraction patterns, people can tell: 1) whether the sample is single crystal or not, 2) what's the crystal phase of the selected diffraction zone. It's also useful to identify the local crystal structure of nanomaterial due to the high spatial resolution from the focused electron beam spot.[68] It is also known as the selected area electron diffraction (SAED).

Thirdly, high resolution Z-contrast image collected from the scattering atoms is another powerful tool developed recently.[69-70] It's also known as high angle angular dark filed scanning transmission electron microscope (HAADF-STEM). The contrast of the image is proportional to square of atom density and atomic number, making it a very sensitive tool to detect low concentration and heavy element species on support. It can also distinguish two different elements if the atomic number are significant different. Now it has been widely applied in the study of supported catalyst and singly atom catalyst.[69-70]

Lastly, characteristic X-ray fluorescence line can be generated when the sample is exposed to high energy excitation source such as the electron beam. By analyzing the fluorescence spectra line, people can obtain the quantitative element information from the sample. The distribution of element is visualized by moving focused electron beam on sample and then evaluate the element concentration spatially.

In short, electron microscope not only capture the image of the local structure of the catalyst, moreover, it actually works as a platform which integrated with other characterization techniques correlated with electron interaction with material such as diffraction, scattering and element analysis.

2.2 In-situ/operando characterization and techniques

2.2.1 Significance of in situ/operando studies

From the view of fundamental understanding, heterogenous catalysis is a surface phenomenon, where the reactant molecules react with the surface atoms of a catalyst and then form the product molecules. To understand catalysis mechanism at atomic level, it's necessary but changeling to understand the local structure of the catalytic active sites during reaction. The structure of the catalytic active sites, particularly the surface of the catalyst, is conventionally characterized by *ex-situ* studies, which is usually done before and after reaction. However, the authentic catalyst structure before or after reaction is different from the working condition in many cases.[9] The origin of the difference between a catalyst surface during catalysis and before/after catalysis is complicated. The partial pressure of the reactants and products around the catalyst surface may change the chemical potential of the system, then consequently change the chemicals state of the catalyst under reaction condition. A well-known example is the supported metal nanoparticle catalyst for CO oxidation. It is not only vulnerable to be oxidized by molecule oxygen from the reactant, but also change the surface structure by coordinate with another reactant, molecule CO.[71-72] To establish a direct correlation between the active surface of a catalyst, in-situ/operando studies of the catalyst is required.

In situ and operando studies are two terms proposed and discussed a lot in the literature of catalysis and surface science.[9, 70, 73-78] Both terms aim to study the structure of the surface, subsurface, and bulk of catalyst particles in the working condition of the catalyst. For operando studies, catalytic activity or reaction rates should be measured. In this thesis, in-situ/operando studies is referred to charactering the catalyst surface or bulk when the catalyst is in a gas (or liquid) phase of one or more reactants under the reaction temperature and pressure.

In principle, in situ/operando study should be done for all chemical processes if the information of reactants or/and products of a chemical reaction such as the surface of a catalyst is necessary for monitoring the production process, measuring yields during production process and understating the catalytic mechanism at a molecular level.[9] Be specific, people could have performed in-situ/operando studies of heterogeneous catalysis by using electron-based techniques. However, most electron-based analytical techniques could not be applied to analyze structure or chemistry of a material under its existing condition (mostly ambient pressure at room temperature) and working condition. Thus, high vacuum environment is necessary for applying these electron-based techniques to analyze materials such as a catalyst. This by-pass strategy provides information of a material under ultra-clean environment, ultrahigh vacuum (UHV) which is distinctly different from its existing environment or working environment. If information achieved through characterization in UHV is the same as those of existing or working environment, the approach of UHV is fine.[77] For example, the crystallographic structure of a mineral or a synthesized nanoparticle examined with TEM in UHV is the same as the authentic structure of the materials in air. However, for a chemical process performed on surface of a material such as a catalytic reaction performed at a solid–gas, solid–liquid, or even solid–liquid–gas interface, the information

achieved in UHV may not be the authentic information of the material in its existing or working environment

As mentioned above, typically the topmost atomic layer of a catalyst participates into the elementary steps of a catalytic cycle. The termination of crystallographic lattice at surface of a catalyst particle obviously makes atoms of the topmost layer highly active due to the low coordination numbers of the topmost layer. Surface energy of such a surface can be readily decreased by chemisorbing reactant molecules, which is surface reconstruction. One example is the surface oxidation of a metal, that is, oxidation of most transition metal by air. More interestingly, surface structure of a metal could be changed by the existence of a gas phase of a reactant above the catalyst surface.

2.2.2 Near ambient pressure X-ray photoelectron spectroscopy (NAP-XPS)

Among those well developed and under developing techniques, in-situ/operando XPS is a promising candidate to study the catalyst surface under existing and working condition due to the superior surface sensitively as discussed. XPS provide information from only a few layers of atoms on the top surface of the catalyst, which contribute to the catalytic actively exclusively. The atoms from deep layers, or in the bulk of the material, contributes neglectable signal to XPS spectrum. However, a significant challenge for developing in-situ/operando XPS for catalysis is the pressure gap. The conventional XPS is a UHV technique while most of heterogenous catalysis reactions occur at the interface between solid-liquid and solid-gas phases. The existence of the gas/liquid phase above solid catalyst reduce the photoelectron signal greatly. Moreover, the core device of XPS instrument such as electron energy analyzer and X-ray source can only work in UHV condition. Thus, to resemble a reactor on the UHV system, it required lots of efforts in instrumental

development to handle the pressure, temperature and flow of the fluidic reactant. Many strategies and efforts were reported in last two decades.[73, 78-80]

The pioneer attempting of studying the surface of a catalyst was achieved by installing another preparation chamber on the UHV system. Then the catalyst is pretreated in the reactant gases environment with certain pressure and temperature before transferred to UHV chamber. The XPS spectrum is still collected in UHV. People reported the surface chemistry changes under pretreatment protocols. However, since the surface of catalyst is still in UHV when collecting the spectrum, it's not considered as a real in-situ/operando method.

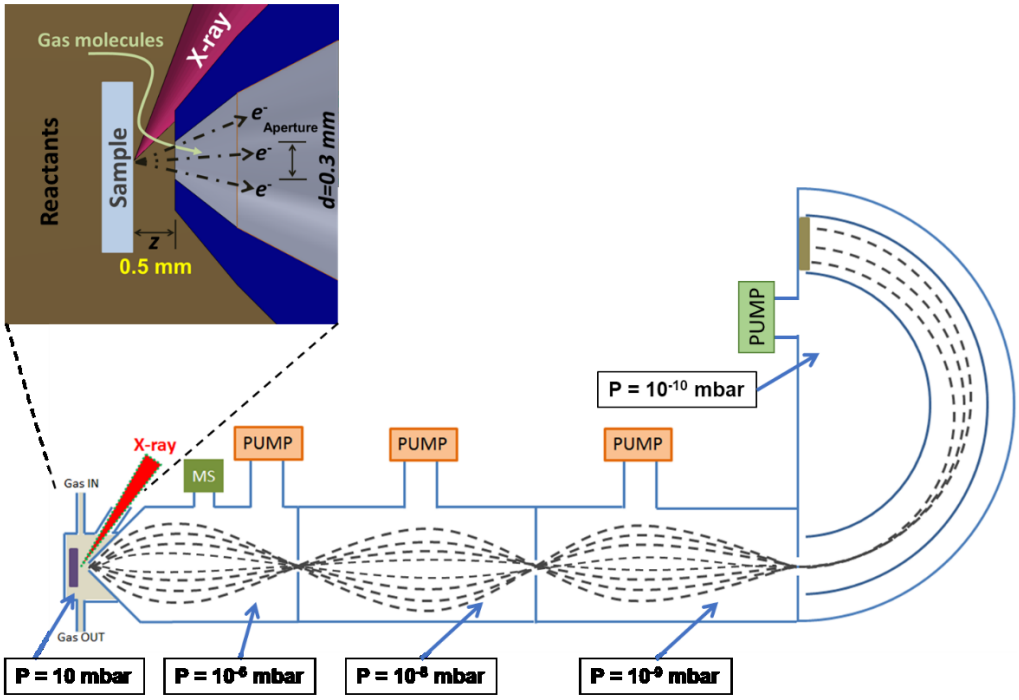

Figure 2.2 demonstration of a typical NAP-XPS instrument setup, including the in-situ reaction cell, differential pumping stage, static lens and analyzer.

As the development of the X-ray source device and the using of differential pump, a significant progress on the instrumental design and application of Near ambient pressure X-ray photoelectron spectroscopy (NAP-XPS) in heterogenous catalysis have been achieved in synchrotron Lightsource and laboratories. A typical NAP-XPS system[77, 79] is as shown in **Figure 2.2**. The sample is installed in an in-situ reaction cell with gas inlet and outlet. It's the only part pressurized with the reactant gases in the whole system. X-ray beam goes through a thin Si_3N_4 window which isolates the X-ray source from the near ambient pressure in the cell. A corn aperture is adapted with the in-situ reaction cell as shown in the zoom-in scheme in **Figure 2.2**. Thus, photoelectrons are collected by the aperture and then entering the energy analyzer. A differential pumping stage is used to pump out the gas molecules in the analyzer. Eventually, the pressure decreases from a few mbar in the cell to UHV at the energy analyzer. Meanwhile, a static electric lens, or focusing lens, is used to control the moving trajectory of the photoelectron without changing the kinetics energy of it.

So far, there are a few general strategies summarized from the instrumental design of NAP-XPS. The first strategy is only creating a local near ambient pressure gas environment above the catalyst. An in-situ reaction cell is designed for the purpose. The gas inlet and outlet, thermal couple and heating unit are integrated with the in-situ reaction cell. An alternative kind of 'back filling' mode has also been also used to full fill the analysis chamber with gases in some NAP-XPS design.[77] However, this back-filling mode is not the optimized choice for in-situ/operando studies of catalysis since the there is very limited flow in the full filled chamber. It takes much longer time to refresh the gaseous reactants and products, which is not ideal to simulate the process in the reactor.

The second strategy is keeping a short distance between sample surface and aperture of energy analyzer. The purpose of keeping a short distance is to minimize the photoelectron intensity decay when travelling though the layer of gas between sample and aperture. The photoelectron intensity I_p after travelling through a gas layer of thickness z and pressure p is given by the equation below:

$$\frac{I_p}{I_0} = e^{\frac{-z*\sigma*p}{k*T}}$$

where I_0 is the original intensity of the photoelectron, σ is the electron scattering cross section of a gas of gas mixture at an electron kinetics energy, k is the Boltzmann constant and T is temperature. In a typical quantitative analysis for an electron with kinetics energy of 500 eV and z=0.5 mm, I_p/I_0 is 83% after traveling in 1 Torr of water vapor at 25°C,[56, 77] but it's only 15% in 10 Torr of water vapor under same condition. Moreover, I_p/I_0 further decays to 65% and 3%, respectively, when z= 1.0 mm. In other words, the signal intensity decays greatly under near ambient pressure when z > 1 mm. This result shows the importance of keeping a short distance between sample and aperture.

The third strategy is using of the focusing lens as shown in **Figure 2.2**. Due to the geometry of the cone aperture and the small opening on it , the portion of photoelectron collected by analyzer is limited. It's necessary to measure the photoelectron entered the analyzer as more as possible. Here the focus lens can change the moving trajectory of photoelectron and then send most of them to the hemisphere analyzer. By using of focus lens, the signal intensity is increased by 1-2 order of magnitude.

The last strategy is using high flux density X-ray source. From the discussion above, it's clear that the signal intensity of NAP-XPS suffers more loss than conventional XPS in UHV setup. The

signal loss is originated from multiple steps: 1) the X-ray is slightly absorbed by the Si3N4 window and the light path in the gas phase; 2) photoelectron generated from the surface of the catalyst need to travel through the gas phase layer; 3) the geometry of the aperture limits the photoelectron collection. Thus, X-ray source with high flux density (brightness, photons per unit time per unit area) is favored in the NAP-XPS experiment as it can generate more photoelectron from the sample surface. There are two type of high flux density X-ray source at current stage, including the synchrotron light source which is usually built in national laboratories, and advanced high flux density X-ray tube.

Combining all above strategies, many NAP-XPS instruments have been built up in synchrotron centers and general labs. They have been applied in the in-situ studies in the heterogenous catalysis, from the fundamental understanding of catalysis mechanism, identification of the catalytic active sites, capture of the reaction intermediate, to designing of novel catalyst.[9, 73, 75-78, 80]

2.2.3 In-situ X-ray absorption spectroscopy

X-ray absorption near edge structure (XANES) and extended X-ray absorption fine structure (EXAFS) provide information on oxidation state and coordination environment of interested elements of catalysts during catalysis. So far, they are widely used in the study of heterogeneous catalysis, particularly in situ/operando studies of catalysts during catalysis. In early 1990s', Clausen *et al*. designed an in-situ cell made of quartz tube which simulated a plug flow reactor and used it for in-situ X-ray diffraction studies.[81] Inspired by this reaction cell, a similar quartz tube cell were widely applied in XAS studies since XAS is also a photon-in and photon-out technique. Typically, the X-ray transmitted through sample was collected for studying XAS spectrum under transmission mode. As a complimentary method, the fluorescence line generated from sample can be also collected for XAS studies. The XAS experiment can be feasibly done

under catalysis condition, where the catalyst is remained at the same temperature in flowing gas of reactant.[74, 82] Besides quartz tube,[81, 83-86] h-BN[87-89] and Kapton[82] could also be used for the in-situ XAS cell for their low X-ray absorption.

Actually, none of them is a perfect material for in-situ XAS cell. People need to choose the proper material based on the experiment parameters. Quartz tube can be heat up to 950°C in most gaseous reactants, but it absorbs more X-ray than other h-BN and Kapton, especially for low energy photons (< 10 keV). Thus, it works best for the absorption edge higher than 10 keV. h-BN tube is stable in oxidizing environment for up to 850 °C, but it's hard to machine it to be thin wall tube. As the results, the absorption of h-BN tube at photon energy < 10keV is not neglectable. It can be used as the complimentary for quartz tube. On the other hand, Kapton can't be heated above 400°C, while its X-ray transmittance is much better than other two materials. It's usually used for the elements with absorption edge lower than 10 keV.

There is also another type of cell has been developed by Nashner and Adler recently for in-situ/operando catalysis.[90] In a typical Nashner cell, catalyst powder is pressed into pellet and clamped on a sample holder, which is heated by a filament cartridge installed at the ambient side the reactor. This specific configuration in fact limits the temperature that the sample can be heated to. This cell cannot heat sample to 500°C or above. The transmission of low energy X-ray (<10 KeV) has no problem with the Nashner cell.

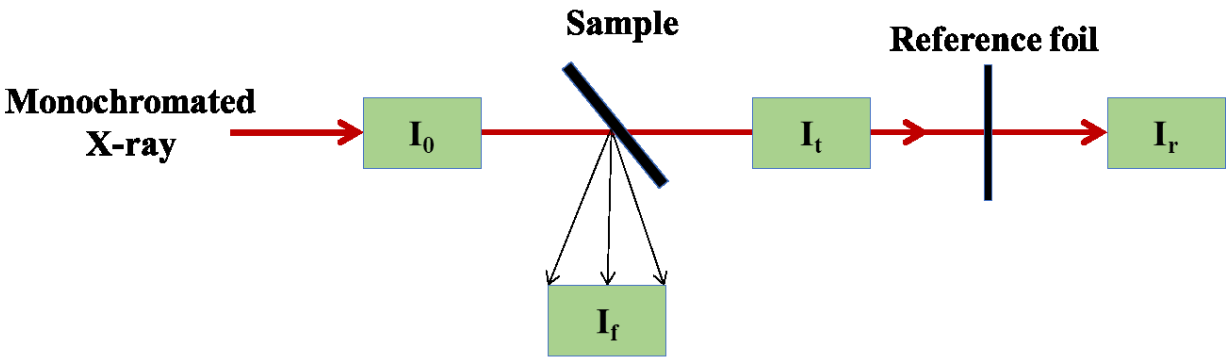

Figure 2.3 scheme of a typical XAS experiment setup in synchrotron center.

A typical XAS experiment setup is summarized in **Figure 2.3**. The X-ray beam is monochromated and focused firstly. The intensities of X-ray beam are commonly measured by gas ionic chamber detectors in I_0, I_t and I_r. The fluorescence signal I_f from the sample could be collected by dedicated detector such as solid-state detector and Lytle detector. One piece of the reference foil is also measured with the sample at the same time, which will be used to calibrate the photon energy. The absorption coefficient for the sample collected by transmission mode (μ_t) and fluorescence mode (μ_f) is deduced by Beers law and shown by equations below.

$$\mu_t = \ln(\frac{I_0}{I_t})$$

$$\mu_f \propto \frac{I_f}{I_0}$$

Depends on the catalysis condition, reactants properties, absorption edge energy of element of interested and other experiment parameters, many similar and revised cells have been proposed and tested for the in-situ/operando XAS studies.[74, 82, 91-94] It has been approved as another powerful

tool to study the chemical state and coordination environment of catalytic species in thermal catalysis, electrocatalysis and biocatalysis.

2.2.4 Environmental TEM

Conventional TEM analyzes either "fresh" or "post-process" catalysts in high vacuum. It visualizes the local structure of the catalytic active sites ex-situ, which may be or not be same to the catalyst under working conditions. The knowledge about the catalyst under working condition is still unclear from the conventional TEM. As discussed in the significance of in-situ/operando studies, TEM characterization should also be performed under catalytic conditions. This is the only way to identify the authentic local structure of the real catalyst. It would be highly desirable to quantitatively measure the activity and selectivity of the catalyst simultaneously so that a structure catalytic performance relation can be established.[95] However, for many heterogenous catalysis and homogenous catalysis reactions, the reactant and product gases is not compatible with the UHC requirement of the TEM instrument. The primary challenge of the in-situ/operando studies of TEM is how to create the localized gas/liquid environment around the sample while the other parts of TEM need to be kept in UHV.

The first environmental cell (E-TEM cell) was prepared by Marton at 1935.[96] A biological sample was sandwiched between two pieces of thin aluminum foils and then installed on a sample holder. A localized living environment for the sample was maintained between the foils. The electron transparent window allows the direct observation of the sample in the desired environment rather than in UHV.[97-98]As the advancement of the TEM technique after 2000s', resolution of TEM has been greatly improved to be Angstrom or sub-Angstrom. Catalysis community began to utilize TEM to resolve the atomic structure of catalyst, in the conventional style. Observation of the

catalyst in the working environment was expected. Thus, many similar but more dedicated E-TEM cells have been inspired and utilized in the in-situ/operando studies for the catalytic materials.[95]

To create the gas environment above the sample, there are two common strategies. (1) window approach. The gas/liquid fluid mixture is confined around the sample by using thin films which are electron transparent. This approach can isolate the local fluid with the UHV chamber. However, the fluid between the thin films are static . To drive the fluid flow though the sample, the cell needs to be designed with the fluid inlet and outlet. (2) the second approach is using the differential pumping which is similar to the setup used in NAP-XPS in **Figure 2.2**. The differential pumping could bridge local environment of sample and UHV chamber. So far, E-TEM has exhibit great potential in the in-situ studies of the structure evolution of the catalyst under working conditions.[95, 99-111]

2.3 Summary

Conventional and in-situ/operando techniques in the studies of catalysis have been discussed in this chapter, including XPS, TEM and XAS. Due to the complexity of the heterogenous catalysis, it's a challenge to characterize the catalyst under working conditions. However, to understand the catalytic reaction in the fundamental level, the correlation of the catalyst structure and catalytic performance need to be revealed. In-situ/operando techniques have been developed in recent decades to study the working catalyst. The principle, application and strategies for in-situ/operando development are discussed.

Chapter 3 Singly dispersed Rh cations anchored on ceria catalyzed methane dry reforming

3.1 Introduction

Methane has attracted much attention as the feedstock for energy purpose and chemical intermediate.[26] As the increasing of annual globe production of methane and decreasing of methane price, there is a strong demand for catalytic converting of methane to higher value products. A common route of methane conversion follows an indirect pathway: methane is firstly reformed to syngas, the mixture of CO and hydrogen, which is a typical chemical intermediate for many chemical engineering processes. Then the syngas is converted to other higher value chemicals. Supported Ni catalyst has been widely studied in the reforming of methane to produce syngas. However, rapid deactivation of Ni catalyst is still a challenge.[112-114]

Two reasons contribute to the rapid deactivation of methane reforming catalyst.[115] Firstly, metal nanoparticles would aggregate under high temperature, which is also known as sintering. As the results, the size of metal nanoparticles will increase, and the specific surface area decrease significantly. The portion of metal atoms exposed at the surface of the nanoparticles would decrease dramatically. The deactivation is the consequence result of less surface metal sites number. On the other hand, the metallic nanoparticles, such as Ni NP, is an excellent catalyst for the rapid decomposition of methane. The formation of coke over the metal catalyst will block the accessing of reactant to active sites, which is another reason for deactivation. To cope with this problem, a rational designed catalyst should be stable over high temperature catalysis. Meanwhile, the formation metallic nanoparticles could be avoided.

Here, the catalyst of singly dispersed Rh cations on the ceria oxide support has been proposed for the methane reforming by CO_2. The singly dispersed Rh cations on CeO_2 was prepared by precipitation-deposition method. The formation of Rh metallic nanoparticles is avoided due to the highly dispersion.[67] Moreover, as an oxygen storage support[116-117], CeO_2 helps to suppress the formation to coke during catalysis.

3.2 Experiment section

CeO_2 nanorods was prepared by a hydrothermal method as reported in literature.[118-119] In a typical synthesis, 1.736 g $Ce(NO_3)_3$*$6H_2O$ was dissolved in 10 mL deionized water, then added into a concentrated NaOH solution (19.2 g NaOH dissolved in 70 mL DI water) dropwisely. The mixed solution was kept under vigorous stirring for 30 min before transferred to Teflon-lined stainless-steel autoclave for hydrothermal treatment at 100 ºC for 24 hrs. Then the autoclave was cooled to room temperature. The yellow powder was washed by deionized water until the pH is neutral. Finally, the powders were dried at 60 ºC for 10 hrs.

Rh_1/CeO_2 catalyst was synthesized by deposition-precipitation method.[67] In a typical synthesis, 1.0 gram of CeO_2 nanorods was dispersed in 50 mL deionized water. The mixture was sonicated for 10 mins and kept at stirring at 400rpm for 1hr. Then rhodium nitrate precursor (containing 2 mg Rh metal for nominal 0.2% weight percent) was dissolved in 20 mL DI water. The rhodium solution was introduced into the ceria oxide dispersion by syringe pump at the flow rate of 0.2 mL/min. The mixture of rhodium and ceria was continuously stirred for another 3 hours. The pH value of the mixture was carefully adjusted to 9.5 by gradually introducing ammonium hydroxide solution, followed by stirring for another 5 hrs. Then the mixture was centrifuged at 3000 rpm for 5 mins, the upper layer was decanted**.** The solid product was dried at a 60 ºC oven overnight, and

a following calcination in muffle furnace at 250 ºC for 2h to obtain the as synthesized Rh_1/CeO_2 catalyst. The actual loading amount of Rh was evaluated by ICP-AES, which was found to be 0.17% weight percent.

Characterization: The *ex-situ* XAS experiment was performed in SSRL beamline 2-2. The Rh K-edge signal was collected under fluorescence mode by a Ge-13 channel detector. One piece of Rh reference foil was measured consequently for the energy calibration purpose. The data was calibrated, merged and analyzed in the Athena and Artemis software package with the standard protocol.[65] The in-situ XAS studies was performed in beamline 2-2, SSRL and beamline 36UL, Spring-8. The catalyst powder was loaded in the capillary quartz tube and then installed on the Clausen cell.[120] Then the mixture of reactant gases was introduced into the cell by mass flow controller. The cell was heated up and then kept at desired temperature for half hour. The Ru K edge spectrum was collected in-situ in the reactant gases environment and catalysis temperature. The data processing and analysis was performed under standard protocol.[65]

The surface chemistry of catalyst was studied with the lab-based ambient pressure X-ray photoelectron spectrum (AP-XPS) system.[79] The reaction cell is integrated with a monochromated Al K-alpha X-ray source and energy analyzer. The mixture of reactant gases (0.5 Torr CH_4 + 0.5 Torr CO_2) was introduced to the reaction cell through a gas manifold where all reactant gases were mixed, and pressures were measured. The total pressure of reactant gases in the reaction cell was the average of the measured pressures by a capacitance gauge located between the gas manifold and tubing to the entrance port of the reaction cell and another capacitance gauge connected to tubing of exit port of the reaction cell. All gases used for AP-XPS studies had a purity of 99.99% or higher. To make sure that the average pressure of the gas in the reaction cell measured at the entrance and exit ports of the reaction cell represents the pressure of gas above the catalyst surface

in the reaction cell, the distance between the sample surface and the aperture was kept twice or more of the aperture size (0.8 mm). The distance was measured with a high-resolution video camera enhanced with an optical lens. The images of the aperture and sample surface shown on the same computer screen allow us to measure the sample-aperture distance by comparing the appeared sample-aperture distance to the appeared diameter of the aperture on the screen. The XPS data was analyzed by CasaXPS software. All the spectrum peaks were calibrated by Au $4f_{7/2}$ peak to 84.0 eV.

DRIFT spectrum of CO absorbed catalyst was collected on a Nicolet Nexus 670 FTIR spectrometer using an MCT/A detector with a spectra resolution of 4 cm^{-1} integrated with a diffuse reflectance reaction cell (Pike Technologies, Model HC-900). The gas-switching experiment was performed using an Agilent Cary 670 FTIR equipped with a linearized MCT detector, a Harrick diffuse reflectance accessory, and a Praying Mantis high-temperature reaction cell. The catalyst was mounted in the cell without dilution. It was pretreated in helium flow to remove surface adsorbates before experiment.

Catalytic performance evaluation the reforming of methane was performed in a fixed bed tubular reactor. In a typical test, 100 mg catalyst was mixed with 0.3 g amorphous silica gel particles (40-60 mesh), then loaded into a quartz tubular reactor. A K-type thermal couple contacted with the catalyst bed for the monitoring of the temperature. The flow rate of methane and carbon dioxide (10% in argon, Matheson) by mass flow controller. The product was analyzed by an on-line GC (SRI-8630C, USA) equipped with a TCD detector.

In the kinetics study, the usage of catalyst was reduced to 5-20 mg to decrease the conversion of methane below 20 %, which falls into the kinetics-controlled regime.[68] The activation energy was

obtained in the typical Arrhenius plot, which is plotting the natural log of the reaction rate as the function of one over temperature in Kelvin. The activation energy could be calculated from the slope of the Arrhenius plot.

3.3 Data and results

3.3.1 identification of the singly dispersion of Rh cations

The concentration of Rh in the catalyst was determined by ICP-AES firstly. The authentic concentration of Rh is 0.17wt% in the catalyst, which is consistent with the nominal concentration of 0.2wt%. The high dispersion is expected as the Rh concentration is low and the deposition - precipitation was well controlled. Due to the relatively low Rh concentration in the catalyst, Rh_1/CeO_2 catalyst remains the light-yellow color of the original CeO_2 support.

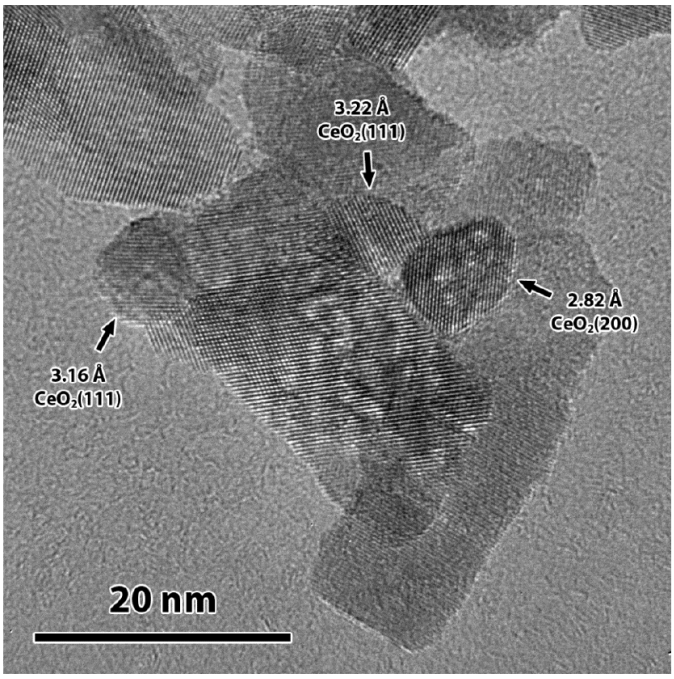

Figure 3.1 Representative HR-TEM images of the Rh_1/CeO_2 catalyst after steam reforming.

A typical HR-TEM image of the Rh_1/CeO_2 catalyst after dry reforming is shown in the **Figure 3.1**. Deposition of Rh cations on the surface of CeO_2 doesn't change the morphology of the CeO_2 nanorods.[119] Moreover, the CeO_2 NR substrate remains the nanorods morphology after thermal catalysis. The representative lattice fringes in the graph are proper assigned to fluorite CeO_2 crystal plane. The fringe of 2.82 Å and 3.22 Å could be assigned to the (200) and (111) of CeO_2, respectively. Here we didn't find any particles or crystal fringes could be assigned to metallic Rh or RhO_x, suggesting the Rh species are highly dispersed. Although HAADF-STEM has been widely used to distinguish supported metal species on oxide support in literature,[121] it's still hard to get conclusive image in this case of Rh_1/CeO_2 catalyst. It is due to the atomic number of ceria is higher than Rh. As the result, the image of ceria support in dark field is much brighter than Rh species, making it's very difficult to tell Rh cations from the support.

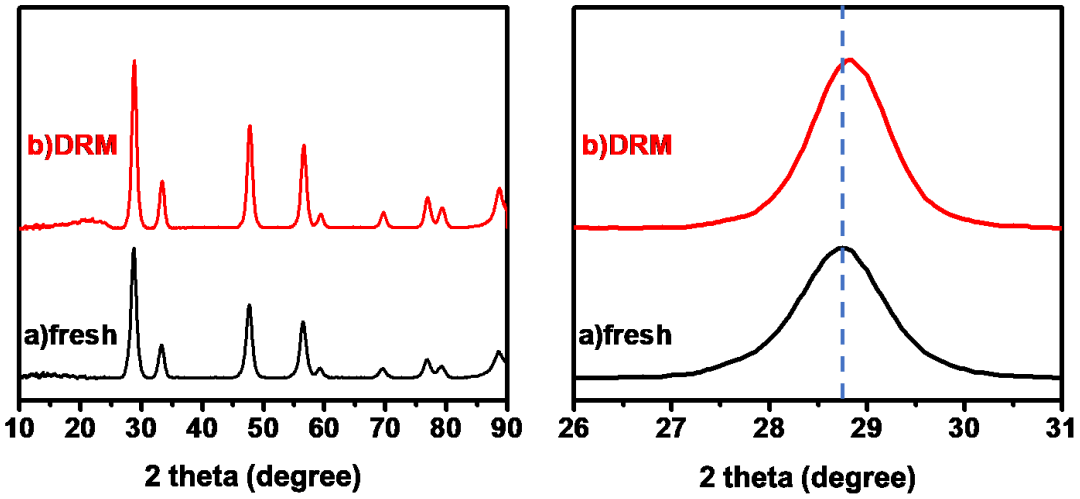

Figure 3.2 XRD pattern of (a) fresh Rh_1/CeO_2 catalyst and (b) Rh_1/CeO_2 after dry reforming.

On the other hand, the XRD patterns of the Rh_1/CeO_2 catalyst (**Figure 3.2**) show a typical CeO_2 fluorite structure. All the diffraction peaks are assigned to CeO_2 structure. The XRD pattern remains well after the thermal catalysis of methane dry reforming, suggesting there is no crystal phase change in the catalyst after reaction. A small bump is observed in 20-30° for the used catalyst, which is result from the amorphous silica gel in the catalyst. There is no metallic Rh or RhO_x peak detected in the XRD. Thus, the aggregated form of Rh species is excluded from the catalyst. The zoom-in spectra at 26-31° is demonstrated in the **Figure 3.2b**, which is the (111) diffraction peak for ceria oxide support. A minor upshift of the diffraction peak position from 28.7° to 28.8° is observed, which is due to the incorporation of Rh into surface lattice of ceria. As the radius of Rh cations is smaller than ceria cations,[122] this surface incorporation will result in the shrinkage of the crystal parameter. Thus, the diffraction peak will upshift according to Bragg equation. Combining the HR-TEM and XRD results, Rh species are highly dispersed on the ceria substrate. The formation of Rh or RhO_x crystal structure could be excluded. Moreover, the catalyst after dry reforming of methane exhibit same diffraction pattern as shown in **Figure 3.2b** and **Figure 3.2c**, suggesting the catalyst remains its CeO_2 structure, without any characterization peak from metallic Rh or RhO_x. In other words, the aggregation of Rh species after could be excluded after catalysis.

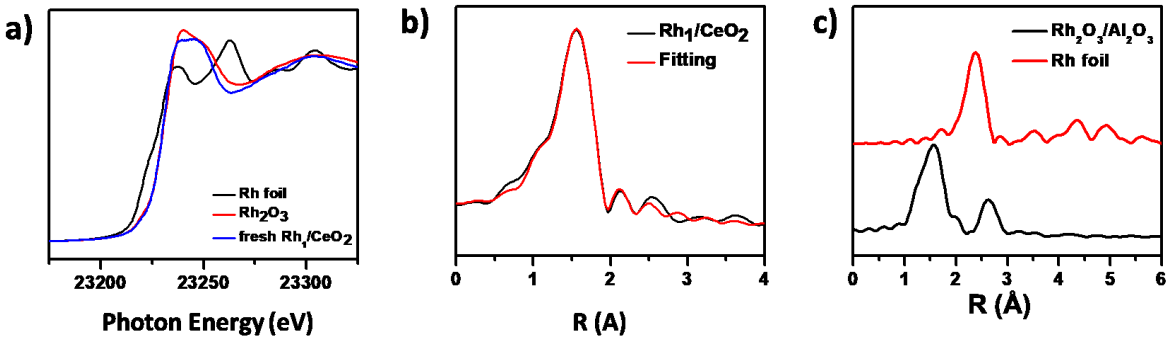

	CN	Distance(A)	ss
Rh-O	6.725±0.380	2.030±0.005	0.003317

Figure 3.3 XANES spectrum of (a) as synthesized Rh_1/CeO_2 catalyst compared with Rh foil and oxide reference, (b) r-space spectrum of EXAFS of Rh K edge for Rh_1/CeO_2 catalyst and (c) the r-space spectrum of Rh foil and oxide reference. Fitting results of r-space spectrum of EXAFS of Rh K edge for Rh_1/CeO_2 catalyst is summarized in the table below.

To further study the Rh state in the catalyst, X-ray absorption spectroscopy was applied to study the chemical state and coordination environment of Rh. As shown in the **Figure 3.3**, The energy of Rh K edge is very similar to the oxide reference, indicating the Rh species in the fresh catalyst are in the oxidized state. In other words, the Rh species exist in cationic form. The Fourier transferred ***r***-space spectrum of the EXAFS spectrum provide direct evidence for the singly dispersion of Rh cations as shown in **Figure 3.3b**. There is only one major peak observed in the range of 0-4 Å, which is properly assigned to the 1st shell coordination with surrounding O atoms. The absence of the 2nd shell coordination of (Rh-O-Rh) at 2.63 Å (as shown the reference spectrum in **Figure 3.3c**) readily excludes the formation of RhO_x clusters. The ***r***-space spectrum data of the fresh catalyst was fitted by IFFEFF program.[65] The coordination number of the first shell (Rh-O) is 6.73±0.38, which is higher than the theoretical CN of (Rh-O) in the bulk rhodium oxide. It could be understood as the Rh cations are partial doped/incorporated into the surface layer of ceria oxide. Thus, the surface doped Rh cations follow the coordination geometry of CeO_2, which has the first shell coordination number of 8. Since XAS is a bulk technique, the apparent coordination number of first shell (Rh-O) is the average of all Rh atoms in the sample. The CN of Rh-O is higher than bulk rhodium oxide. In summary, from the EXAFS results, no doubt the Rh species are *singly dispersed* on the CeO_2 NR substrate.

DRFIT spectrum of CO absorbed catalyst also supports the singly dispersion of Rh cations on the surface of CeO_2. As reported in literature, there are three types of absorption geometry for CO

molecular on Rh sites[121, 123]: (a) one CO absorbed on two adjacent Rh sites in the bridge geometry as a broad and intensive peak at 1900-1800 cm^{-1}; (b) linear absorption of one molecular on one Rh site, which is usually a sharp and intensive peak at ~2050 cm^{-1}. (c) one pair of twin peak in 2100-2000 cm^{-1}, which is assigned to two CO molecule absorbed on one Rh site in a germinal geometry. As the feature **a** is associated with Rh-Rh bond, it's the conclusive evidence for the existing of Rh metallic nanoparticles in the catalyst. On the other hand, the germinal geometry of CO absorption over isolated Rh sites on ZrO_2, ZnO and TiO_2 has been reported.[121, 124-126]

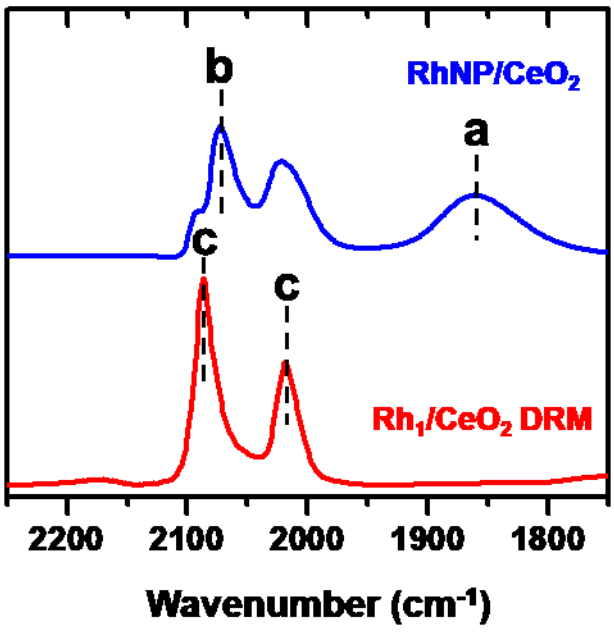

Figure 3.4 DRIFT CO spectrum of Rh_1/CeO_2 catalyst compared with $RhNP/CeO_2$ reference. The CO peaks are labeled by CO absorption geometry: (a) one CO molecule absorbed on two adjacent Rh-Rh sites, (b) linear absorption of one CO molecule over one Rh site; (c) two CO molecule absorbed on one Rh sites.

As shown in **Figure 3.4**, the DRIFT spectrum of CO absorbed catalyst after dry reforming exhibits a pair of twin peak at 2086 and 2018 cm^{-1}, which is assigned to two CO molecule absorbed

on one Rh site in the germinal geometry. There is no peak in 1800-1900 cm^{-1}, which is corresponding to one CO molecule absorbed on two Rh sites in the bridge form as shown in the RhNP reference sample. Thus, the singly dispersion of Rh cations in the sample is not only in the fresh catalyst, but also remains well after dry reforming catalysis. From the above discussion, the singly dispersion of the Rh cations on the ceria support has been proved by multiple ex-situ characterization techniques, such as XRD, TEM, XAS and DRIFT CO spectrum.

3.3.2 Catalytic performance of Rh_1/CeO_2 catalyst

Catalytic dry reforming promoted by Rh_1/CeO_2 catalyst was investigated in the thermal catalysis reactor. The influence of pretreatment temperature is investigated carefully as shown in **Figure 3.5**. Generally, the Rh_1/CeO_2 catalyst could convert methane readily to hydrogen with high conversion and high yield. The conversion of methane and selectivity to hydrogen is increasing as the temperature increases. The effect of pretreatment temperature plays a minor role on the catalytic performance. In other word, the catalytic performance is not affected by pretreatment temperature, except at 600 and 700ºC. It could be deduced that the catalytic active center of Rh_1/CeO_2 is quite stable to the reductive pretreatment conditions. The slightly activity loss at 600 and 700ºC might be due to the sink of Rh atoms into the CeO_2 substrate to form solid oxide solution at high reduction temperature. In general, pure CeO_2 was found to be a catalytic inactive material for this reaction. By anchoring 0.17wt% Rh cations on the surface, CeO_2 changes to be very active for the reforming of methane. This significant change of the catalytic properties is attribute to enhanced C-H bond activation ability by Rh cations, which is similar to theoretical studies on the similar system.[127]

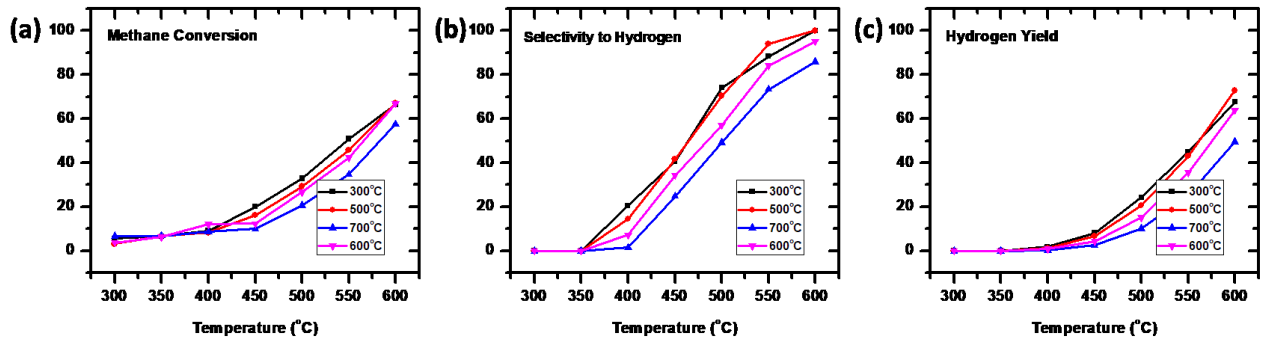

Figure 3.5 catalysis performance of the Rh_1/CeO_2 catalyst in term of (a) the conversion of methane, (b) selectivity to hydrogen and (c) yield of hydrogen. Pretreatment was performed before catalysis test, which was reduced by 5% H_2 for 30 min at given temperature.

The activation energy of the catalyst was measured in the kinetics-controlled regime, where the conversion of methane is less than 20%. In a typical experiment, 30 mg Rh_1/CeO_2 catalyst was used. The catalyst was calcined in air at 250ºC and then reduced in 5% hydrogen at 300ºC for 1hr before test. Kinetics controlled reaction rate was measured from 450ºC to 550ºC. The kinetics studies from both methane conversion rate and hydrogen production rate show an activation energy barrier at 40~50 kJ/mol (**Figure 3.6**). This apparent activation energy barrier is much lower than the value reported in literature from those supported transition metal nanoparticles catalyst such as Ni, Ru, Pd, Rh, Pt and Ir, which is usually higher than 100 kJ/mol.[128-133] The greatly decreased activation energy barrier for the methane reforming is assigned to the unique electronic state of the single Rh cations, which facilize the activation of C-H bond of CH_4.[127] It suggests the reaction mechanism of methane reforming over Rh_1/CeO_2 catalyst is different from the mechanism catalyst by supported transition metal nanoparticles.[128-133]

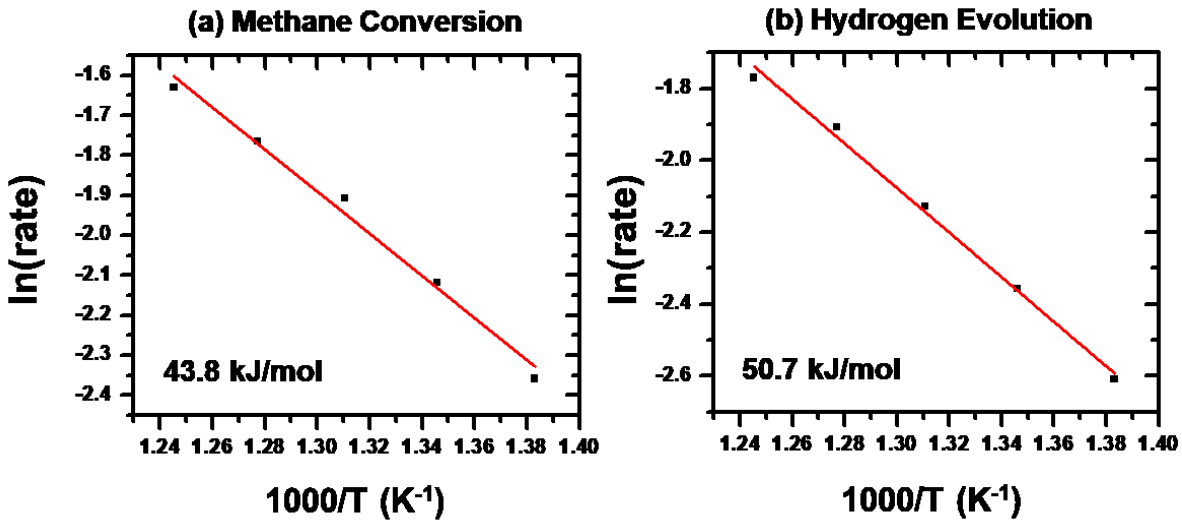

Figure 3.6 Arrhenius plot of the Rh_1/CeO_2 catalyst for methane dry reforming in term of (a) rate of methane conversion and (b) rate of hydrogen production.

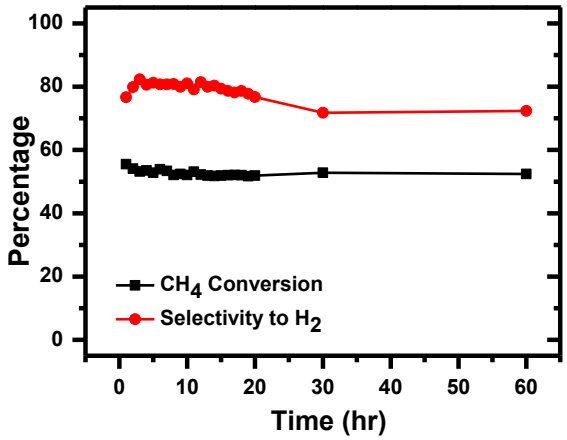

Figure 3.7 stability of methane dry reforming over Rh_1/CeO_2 catalyst

The long-term stability test of the Rh_1/CeO_2 catalyst shows superb stability of the catalyst. The methane conversion and hydrogen yield remain well after 60 hrs reaction. No deactivation was found in the catalyst up to 3 day. The outstanding stability is assigned to the highly dispersion of Rh cations on the CeO_2 support. The coke formation is suppressed since there is lacking of metallic

Rh-Rh bond, which is very active in breaking the C-H bond in methane.[134] Moreover, the strong interaction of Rh cations with CeO_2 support limits the mobilizing of Rh cations at high temperature of catalysis. Thus, the sintering of Rh species could be also avoided.

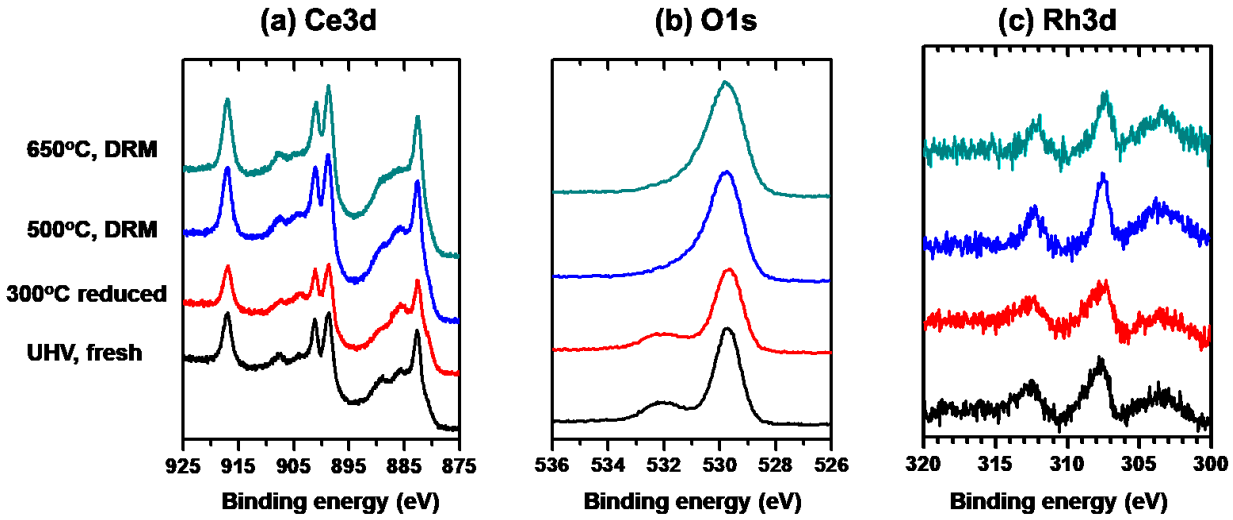

Figure 3.8 Photoemission feature of (a) Ce*3d*, (b) O*1s* and (c) Rh*3d* from the Rh_1/CeO_2 catalyst in fresh catalyst, be reduced and during dry reforming at 500°C and 650°C. 0.5 Torr CH_4 mixed with 0.5 Torr CO_2 was introduced into reaction cell for dry reforming.

3.3.3 In-situ spectroscopy studies of methane reforming catalyzed by Rh_1/CeO_2

The surface chemistries of the Rh_1/CeO_2 catalyst in reactant conditions were studied by ambient pressure XPS.[79] As shown in **Figure 3.8**, the Ce*3d*, O*1s* and Rh*3d* features were collected for the fresh catalyst, 300 °C pretreatment, and dry reforming at 500 °C and 650 °C. As shown in the **Figure 3.8a**, the surface oxygen vacancy concentration which could be quantitatively determined by the surface $Ce^{3+}/(Ce^{3+}+Ce^{4+})$ ratio since the origination of the surface oxygen vacancy is the Ce^{3+} species.[56, 58] The surface oxygen vacancy is 33%, 43%, 34% and 32% for the fresh sample, 300 °C reduced, dry reforming at 500 °C and 600 °C, respectively. The initial surface of the catalyst

exhibits a relative high concentration of Ce^{3+}, which is induced by doping of Rh cations into the surface CeO_2 lattice. The mismatch of doped Rh cations results into high concentration of oxygen vacancy, which is accompanied by high Ce^{3+} concentration. The surface oxygen vacancy increased by in reductive environment and remained at 32~34% under dry reforming conditions. For the O*1s* spectra in the **Figure 3.8b**, there is one major peak at 529.5 eV which is contributed from the lattice oxygen in the CeO_2 support. Another minor component at 532.0 eV was found for the fresh catalyst and 300 ºC reduced condition, which is the from oxygen in the surface hydroxyl group. This minor component disappeared at dry reforming condition since the surface hydroxyl group could be removed under high temperature. In the **Figure 3.8c**, Rh*3d* at UHV and 300ºC reduced could be deconvoluted to two components, one at 307.4 eV and another at 308.4 eV. There is also another peak at 303 eV, which is assigned to the M_3VV Auger peak of Ce.[135] The 308.4 eV component is assigned to the Rh in oxygen surrounding environment, it was disappeared at dry reforming condition. The 307.4 eV component is still 0.2 eV higher than metallic state. In summary, the surface of the catalyst is rich in oxygen vacancy and the Rh maintain the cationic chemicals state during dry reforming of methane.

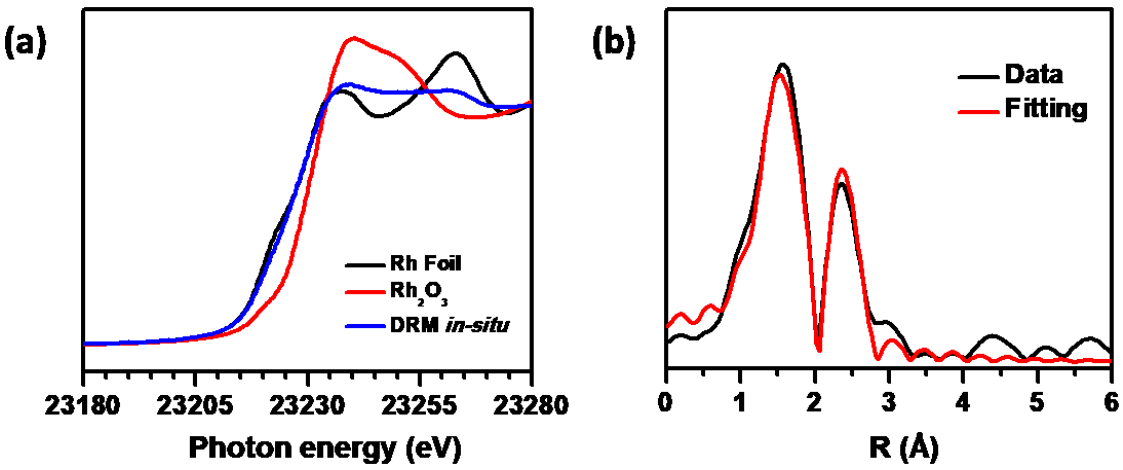

(c)

bond	CN	Distance(A)	ss
Rh-O	4.28±0.93	2.03±0.02	0.00711
Rh-Rh	2.57±1.08	2.65±0.02	0.00711

Figure 3.9 in-situ XAS studies of the Rh_1/CeO_2 catalyst. (a) XANES of the Rh K edge of Rh_1/CeO_2 catalyst compared with foil and oxide reference; (b) fitting of r-space spectrum of EXAFS from the Rh K edge of Rh_1/CeO_2 catalyst, (c) the fitting parameters summarized.

The in-situ XAS studies of the catalyst during dry reforming of methane is shown in **Figure 3.9**. The XANES of Rh K edge of the used catalyst is compared with Rh foil and oxide reference in **Figure 3.9a**. The energy of the Rh K edge of the used catalyst is between foil and oxide, but closer to foil. It suggests Rh is not in the oxide or metallic state, but an intermediate state. The Fourier transformed r-space spectrum could be fitted by the insight as shown in **Figure 3.9b**. There are two peaks in the r-space spectrum. The first peak is located at ~1.5Å, which is the typical Rh-O coordination pathway as reported in literature. The second peak at about 2.3 Å is assigned to the Rh-Rh coordination pathway. The fitting results is summarized in the table in **Figure 3.9c**. The coordination number (CN) of the first shell Rh-O is 4.28±0.93, while the bond length is 2.03±0.02. The bond length is consistent with the Rh-O bond in literature. The CN is lower than the CN of

the fresh catalyst, suggesting the surface of catalyst is oxygen lacking. This is consistent with the Ce*3d* spectra of AP-XPS results. Another minor peak is also fitted with Rh-Ce coordination pathway with CN of 2.57±1.08. The coordination distance is 2.65±1.02 Å. From this fitting results, the local structure of Rh species during catalysis is proposed to be small Rh cluster composed of a few Rh atoms supported on CeO_2.

In summary, in-situ spectroscopy studies of the methane dry reforming over Rh_1/CeO_2 catalyst reveal the chemical state of the catalytic sites during reaction condition. The surface oxygen vacancy ratio is 32-34% in the dry reforming, in other words, the surface lattice oxygen is removed during catalysis. Meanwhile, Rh nanoclusters containing a few atoms are formed during catalysis, which is the catalytic active sites for methane reforming.

3.4 Conclusion

The Rh_1/CeO_2 catalyst was proposed and successfully synthesized. The singly dispersion of Rh cations on CeO_2 support was confirmed by TEM, XRD, DRIFT spectrum and XAS. The Rh_1/CeO_2 catalyst is active for the methane dry reforming with CO_2. The superior stability of this catalyst was confirmed and assigned to the highly dispersion of Rh cations on CeO_2. The surface chemistry and coordination environment of the active sites was studied by in-situ XAS and AP-XPS.

Chapter 4 Methane steam reforming over Rh_1/CeO_2 catalyst

4.1 Introduction

Methane is firstly reformed with steam to produce syngas, which is the mixture of CO and H_2. Then syngas could be converted to other chemical intermediate and products via methanol-to-olefin (MTO) process, Fisher-Tropsch synthesis and other processes.[26, 113] The steam reforming is catalyzed with supported nickel catalyst at a temperature higher than 800ºC. Unfortunately, this high temperature pathway requests significant amount of energy supply. In addition, coke formation is another major problem. This is because that Ni atoms at metallic state can chemisorbe CH_n (n=0-3) strongly; more importantly, the continuous packed Ni atoms allows coupling of chemisorbed CH_n species which are the precursors of coke. To suppress the coke formation during methane reforming, it is essential to break the metallic nanoparticles and clusters, by which the CH_n species could not couple to form precursors of coke. Here, the catalyst of singly dispersed Rh cations on the ceria oxide support was prepared for reforming methane with water. The singly dispersed Rh cations on CeO_2 were prepared by precipitation-deposition method. The Rh cations are singly dispersed to avoid the formation of metallic Rh-Rh bond, which makes it a potential catalyst for methane conversion.

4.2 Experiment

CeO_2 nanorods was prepared by a hydrothermal method as reported in literature.[118-119] In a typical synthesis, 1.736 g $Ce(NO_3)_3*6H_2O$ was dissolved in 10 mL deionized water, then added into a concentrated NaOH solution (19.2 g NaOH dissolved in 70 mL DI water) dropwisely. The mixed solution was kept under vigorous stirring for 30 min before transferred to Teflon-lined stainless-steel autoclave for hydrothermal treatment at 100 ºC for 24 hrs. Then the autoclave was cooled to

room temperature. The yellow powder was washed by deionized water until the pH is neutral. Finally, the powders were dried at 60 ºC for 10 hrs.

Rh_1/CeO_2 catalyst was synthesized by deposition-precipitation method.[67] In a typical synthesis, 1.0 gram of CeO_2 nanorods was dispersed in 50 mL deionized water. The mixture was sonicated for 10 mins and kept at stirring at 400rpm for 1hr. Then rhodium nitrate precursor (containing 2 mg Rh metal for nominal 0.2% weight percent) was dissolved in 20 mL DI water. The rhodium solution was introduced into the ceria oxide dispersion by syringe pump at the flow rate of 0.2 mL/min. The mixture of rhodium and ceria was continuously stirred for another 3 hours. The pH value of the mixture was carefully adjusted to 9.5 by gradually introducing ammonium hydroxide solution, followed by stirring for another 5 hrs. Then the mixture was centrifuged at 3000 rpm for 5 mins, the upper layer was decanted**.** The solid product was dried at a 60 ºC oven overnight, and a following calcination in muffle furnace at 250 ºC for 2h to obtain the as synthesized Rh_1/CeO_2 catalyst. The actual loading amount of Rh was evaluated by ICP-AES, which was found to be 0.17% weight percent.

Characterization: The *ex-situ* XAS experiment was performed in SSRL beamline 2-2. The Rh K-edge signal was collected under fluorescence mode by a Ge-13 channel detector. One piece of Rh reference foil was measured consequently for the energy calibration purpose. The data was calibrated, merged and analyzed in the Athena and Artemis software package with the standard protocol.[65] The in-situ XAS studies was performed in beamline 2-2, SSRL and beamline 36UL, Spring-8. The catalyst powder was loaded in the capillary quartz tube and then installed on the Clausen cell.[120] Then the mixture of reactant gases was introduced into the cell by mass flow controller. The cell was heated up and then kept at desired temperaturefor half hour. The Ru K

edge spectrum was collected in-situ in the reactant gases environment and catalysis temperature. The data processing and analysis was performed under standard protocol.[65]

The surface chemistry of catalyst was studied with the lab-based ambient pressure X-ray photoelectron spectrum (AP-XPS) system.[79] The reaction cell is integrated with a monochromated Al K-alpha X-ray source and energy analyzer. The mixture of reactant gases (0.5 Torr CH_4 + 0.5 Torr H_2O) was introduced to the reaction cell through a gas manifold where all reactant gases were mixed, and pressures were measured. The XPS data was analyzed by CasaXPS software. All the spectrum peaks were calibrated by Au $4f_{7/2}$ peak to 84.0 eV.[55]

DRIFT spectrum of CO absorbed catalyst was collected on a Nicolet Nexus 670 FTIR spectrometer using an MCT/A detector with a spectra resolution of 4 cm^{-1} integrated with a diffuse reflectance reaction cell (Pike Technologies, Model HC-900). The DRIFT spectrum of CO absorbed catalyst was collected for the catalyst *ex-situ* and *in-situ*. In the ex-situ experiment, sample powder was loaded to the cell and then kept in Helium at 300^oC for 10 mins to remove surface absorbed molecules. Then it was cooled down to 25 ^oC before introducing CO. KBr window was used in the cell. For the *in-situ* experiment, The Rh_1/CeO_2 catalyst was mounted in the Harrick cell. Water vapor and CH_4 were introduced into the in-situ IR cell; then the catalyst was heated and kept at 550^oC for 30 mins. The catalyst was cooled down to 25 ^oC under helium flow. Then CO was introduced to the surface of the catalyst. The difference spectrum before and after chemisorption of CO was obtained. As the steam vapor would damage the KBr window, ZnSe window was used in this experiment

Catalytic performance evaluation the reforming of methane was performed in a fixed bed tubular reactor. In a typical test, 50 mg catalyst was mixed with 300 mg amorphous silica gel particles

(40-60 mesh), then loaded into a quartz tubular reactor. A K-type thermal couple contacted with the catalyst bed for monitoring temperature of the catalyst. The flow rate of methane was controlled by mass flow controller (10% in Ar, 20 mL/min). Water was introduced via a syringe pump in the format of water vapor formed through vaporization at 120°C before entering reactor. The mole flow rate of water was kept at two times of methane if there is no other notice. The product was analyzed by an on-line GC (SRI-8630C, USA) equipped with a TCD detector.

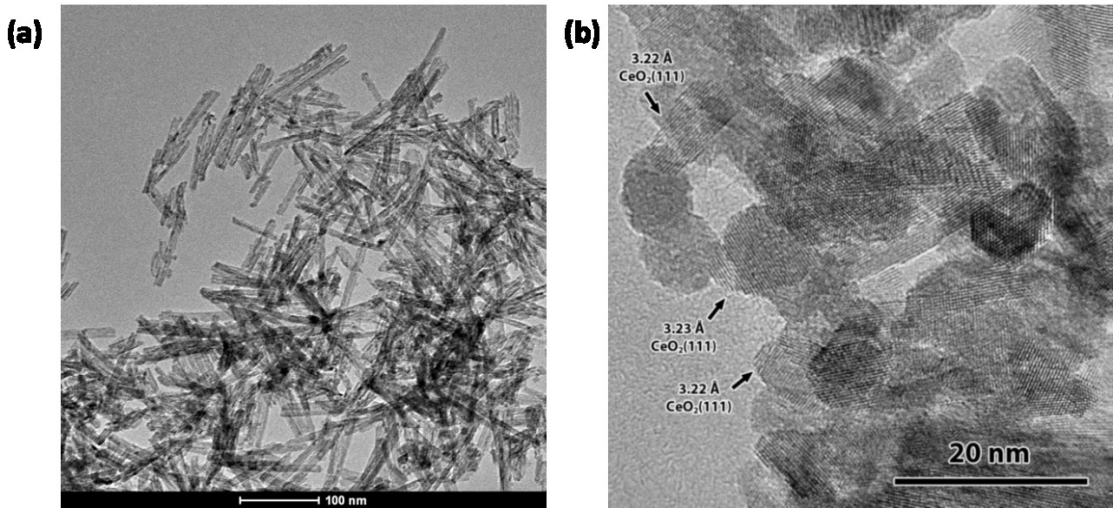

Figure 4.1 Representative TEM images of the Rh_1/CeO_2 catalyst: (a) as synthesized and (b) after steam reforming reaction.

In the kinetics study, the usage of catalyst was reduced to 5-20 mg to decrease the conversion of methane below 20 %, which falls into the kinetics-controlled regime.[68] The activation energy was obtained in a typical Arrhenius plot which is a plot of the natural log of the reaction rate as the function of reciprocal temperature in Kelvin. The activation energy was calculated from the slope of the Arrhenius plot.

4.3 Results and discussion

4.3.1 identification of Rh sites on ceria support

The Rh_1/CeO_2 catalyst was examined by TEM firstly. As shown in **Figure 4.1**, the Rh_1/CeO_2 catalyst exhibits morphology of nanorods, which is consistent with literatures.[118] The length of the nanorods is 100-200 nm while the diameter is 5-10 nm. There is no evidence for the formation of Rh or rhodium oxide nanoparticles under the TEM scope. Since the loading concentration of Rh is low, the highly dispersed of Rh species are expected. The lack of Rh metal nanoparticle and RhOx nanoparticles was confirmed by XRD patternof the catalyst. As shown in **Figure 4.2**, the fresh Rh_1/CeO_2 catalyst exhibits a typical fluorite diffraction pattern of CeO_2.[118] All the peaks in the figure can be assigned to specific CeO_2 lattice plane. The diffraction pattern of the used catalyst after steam reforming is also shown in **Figure 4.2**. Clearly, the fluorite type diffraction pattern remains after steam reforming test; there is no new peaks appeared other then peaks of CeO_2 nanorods., It suggests that there is no obvious peak of Rh or RhO_x nanoparticles found in the results. Both TEM and XRD results suggests that the Rh species are highly dispersed on the ceria .

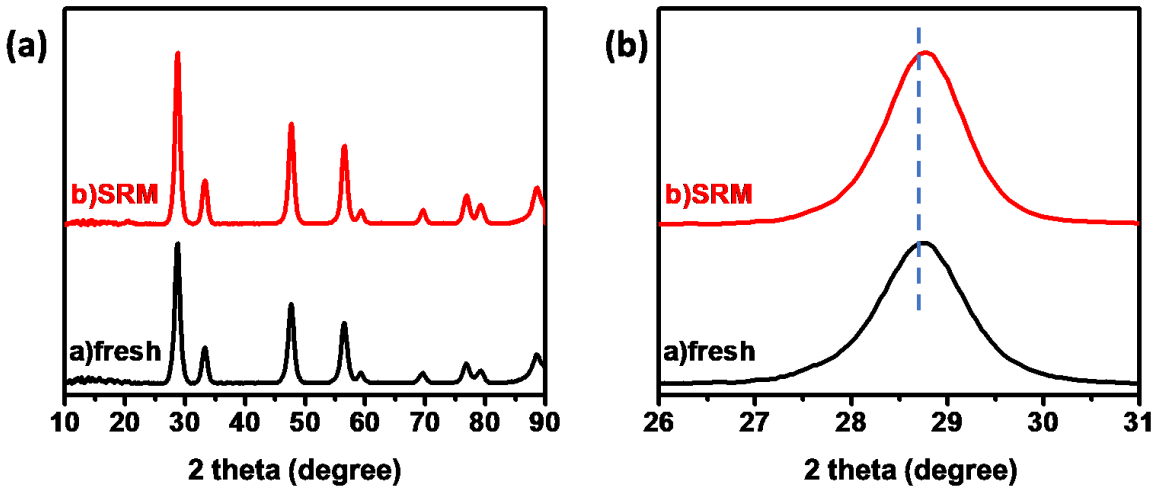

Figure 4.2 XRD pattern of (a) as synthesized Rh_1/CeO_2 catalyst, (b) Rh_1/CeO_2 after steam reforming and (c) Rh_1/CeO_2 after dry reforming.

The chemical state and coordination environment of Rh species were further studied by XAS. These results have been well discussed in the **Chapter 3.3.1** since this catalyst was used for steam reforming of CH4 as well. The single dispersion of Rh cations was clearly confirmed with EXAFS. In addition, the single dispersion of Rh cations was further confirmed by the DRIFT spectrum of CO absorbed on the Rh_1/CeO_2 catalyst in **Figure 4.3**. Experiment was performed via Harrick cell with KBr window. The observation of multiple peaksof CO absorbed on Rh NPs (red curve in Figure 4.3) are assigned to different absorbed geometry of CO molecules.[121, 123] Feature **a** in red curve of Figure 4.3 is the CO molecule absorbed on Rh NPs in a bridge configuration over two adjacent Rh atoms. It suggests there is Rh-Rh bond in the sample. Feature **b** is assigned to the CO molecule absorbed on top of one Rh atom in the linear geometry. The twin components **c** in red curve of Figure 4.3 appears a pair, which are assigned to two CO molecules absorbed on one Rh atom in the germinal geometry. All the three kinds of absorbed CO were found since CO could be absorbed on the surface of RhNP in various geometry. On the other hand, there is only feature c in the Rh_1/CeO_2 catalyst (black curve in Figure 4.3). The lacking of feature **a** in the Rh_1/CeO_2 catalyst excludes the formation of Rh-Rh coordination in the Rh_1/CeO_2 catalyst. Thus, the single dispersion of Rh cations on the surface of CeO_2 nanorods was suggested by TEM, XRD, XAS and DRIFT CO spectrum.

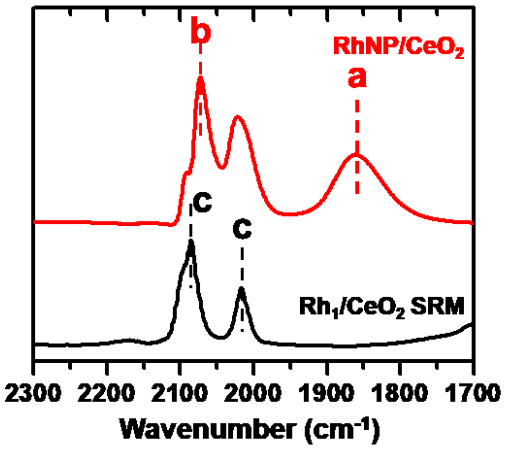

Figure 4.3 DRFIT spectrum of CO absorbed $Rh_1/CeO2$ catalyst after steam reforming and $RhNP/CeO_2$.

4.3.2 Catalytic performance on steam reforming of methane

Steam reforming of methane (SRM) catalyzed by Rh_1/CeO_2 catalyst was evaluated in a fixed-bed flow reactor. Figure 4.4 is the plot of methane conversion and hydrogen yield as the function of temperature. Catalyst was pretreated in $5\%H_2$ at desired temperature. The Rh_1/CeO_2 catalyst is active for the steam reforming of methane. The methane conversions and hydrogen yields increase along the increase of temperature. The catalytic performance was evaluated with different pretreatment temperature in hydrogen. The catalytic performances of catalysts treated at different temperatures are similar, suggesting that the pretreatment temperature is not an important term in determining catalytic performance.

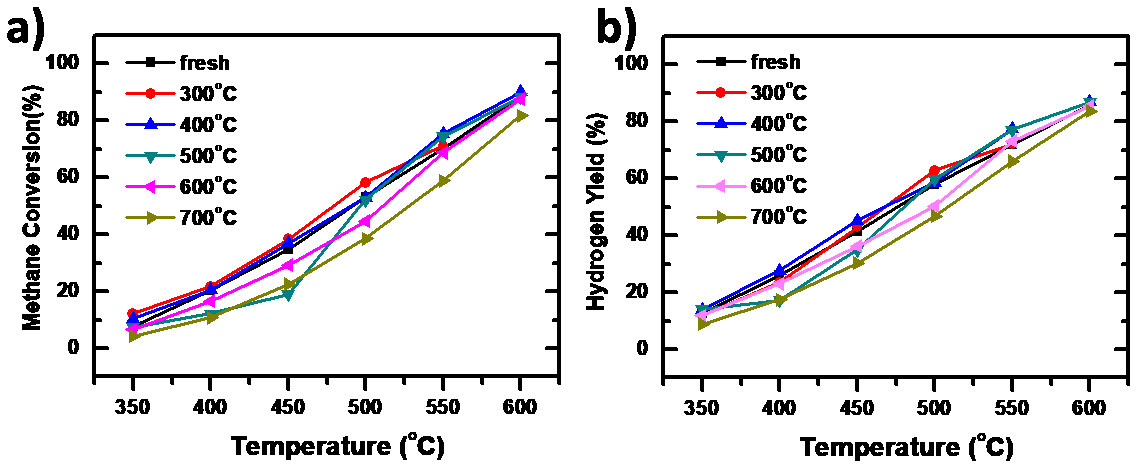

Figure 4.4 catalytic performance of of methane steam reforming over Rh_1/CeO_2 catalyst in term of (a) the methane conversion and (b) hydrogen yield as the function of temperature. Catalyst was reduced in 5%H2 at the labeled temperature before catalysis test.

The apparent activation energy barrier for the methane steam reforming over Rh_1/CeO_2 catalyst was evaluated by the Arrhenius plot in **Figure 4.5**. It is 40.8 kJ/mol in term of methane conversion while it is 45.2 kJ/mol in term of hydrogen evolution. The measured activation energy is much lower than the reported values of other catalysts,[130-131, 133, 136-138] indicating this Rh_1/CeO_2 catalyst is very active for the methane reforming. Similar activation energy test was performed with catalyst upon a higher pretreatment temperature. The activation energy doesn't change upon higher pretreatment temperature in hydrogen. Thus, the active sites of the Rh_1/CeO_2 catalyst is quite stable over the pretreatment temperature.

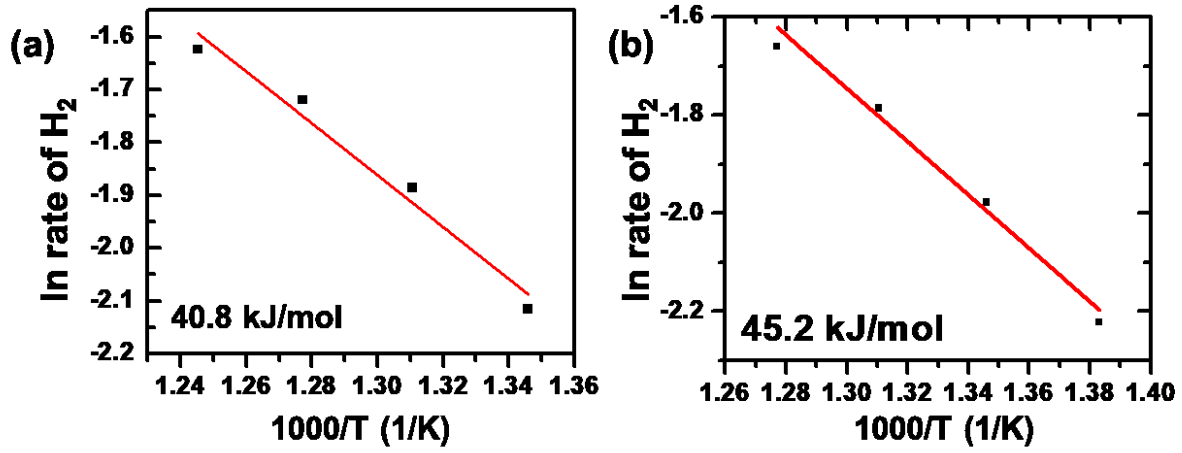

Figure 4.5 Arrhenius plot of the methane steam reforming over Rh_1/CeO_2 catalyst in term of hydrogen production rate with pretreatment at (a) 300ºC and (b) 500ºC

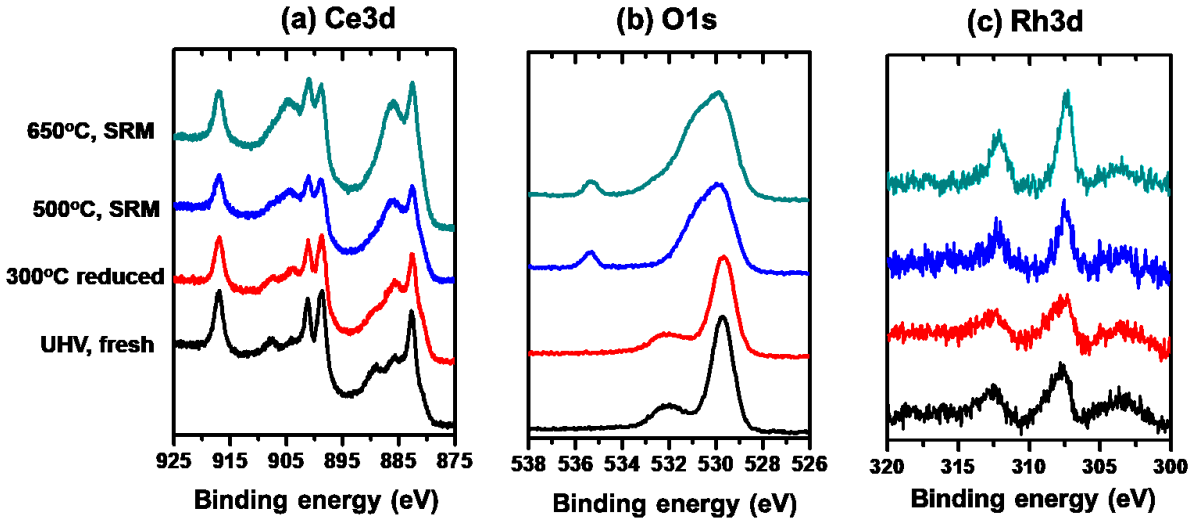

Figure 4.6 the photoemission features of (a) Ce3d, (b) O1s and (c) Rh3d of the Rh_1/CeO_2 catalyst collected in AP-XPS.

4.3.3 In-situ studies of the reaction mechanism

The surface chemistry of the steam reforming over the Rh_1/CeO_2 catalyst was studies by the AP-XPS.[79] The photoemission features of Ce3d, O1s and Rh3d are summarized in the **Figure 4.6**. The Ce3d in the **Figure 4.6a** could be deconvoluted to ten components from Ce^{3+} and Ce^{4+}.[56] The surface of the fresh catalyst contains 33% Ce^{3+}, which is associated with the surface oxygen vacancy sites. Thus, anchoring of Rh cations on the surface of the ceria support helps creating oxygen vacancy. The surface oxygen vacancy increases upon the hydrogen pretreatment and is even higher at steam reforming conditions. The surface dominated by Ce^{3+} at steam reforming condition, which is 53% and 55% at 500ºC and 650ºC, respectively. It suggests that significant number of surface vacancies was formed during catalysis conditions. In the O1s spectrum as shown in **Figure 4.6b**, there is one peak at 536 eV which is the XPS peak of gas phase of H_2O. This is the characteristic feature of the AP-XPS studies. The O1s spectrum of the fresh catalyst contains two peaks, a minor one at 532 eV which is assigned to surface hydroxyl group while the other one at 529.5 eV is from the oxygen atoms of the CeO_2 lattice. The hydroxyl group remains under 300ºC reduction but eventually is disappeared. The disappearance of OH groups is due to the removal of the surface hydroxyl group in the catalysis condition. Accompanied with the disappearance of the surface hydroxyl group, one component of O1s at 531 eV could be deconvoluted, which is assigned to the nonstoichiometric oxygen anions. The Rh3d feature is presented in the **Figure 4.6c**. The binding energy of Rh3d is 307.4 eV, which is slightly higher than metallic Rh.

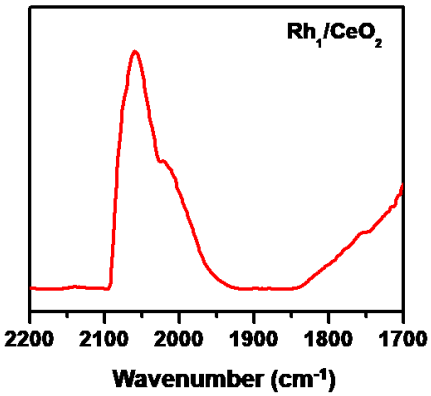

Figure 4.7 *In-situ* DRIFT spectrum of CO absorbed catalyst after catalysis.

In-situ DRIFT spectrum of CO absorbed on the catalyst was performed to study the dispersion of Rh cations during catalysis. As shown in **Figure 4.7,** the DRIFT spectrum of CO absorbed on the catalyst from the steam reforming catalysis exhibits one broad peak in the window of 1950 - 2100 cm^{-1}. These peaks are broader than the ex-situ data, due to the use of ZnSe window. The spectrum of 1900-1800 cm^{-1} is the base line only, without the molecule CO absorbed on the Rh-Rh sites. Thus, the Rh-Rh bond is excluded from the analysis of IR spectrum of catalyst in the steam reforming condition. Rh metallic nanoparticles or nanoclusters are not formed during catalysis. Notably, the main feature in 2100-1950 cm^{-1} in Figure 4.7 can be deconvoluted into one pair of twin peaks assigned to the germinal absorbed two CO molecules on a Rh single atom.

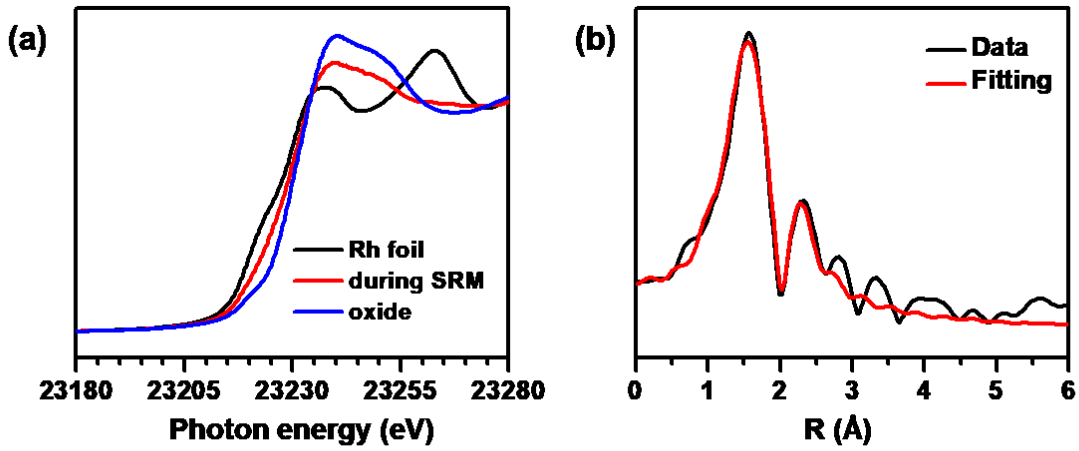

(c)

Pathway	CN	Distance(A)	ss
Rh-O	4.86±1.02	2.04±0.02	0.00516
Rh-Rh	1.16±0.49	2.57±0.04	0.00516

Figure 4.8 in-situ XAS spectrum of the Rh_1/CeO_2 catalyst after catalysis. (a) XANES spectrum and (b) r-space spectrum of Rh K edge during steam reforming of methane at 500°C. (c) the fitting parameters of ***r***-space spectrum.

In-situ/operando XAS experiment was performed to characterize the chemical state and coordination environment of Rh atoms of the catalyst during catalysis. The ex-situ spectrum of the Rh_1/CeO_2 catalyst after steam reforming is shown in the **Figure 4.8**. From the XANES spectrum of the Rh K edge from the catalyst after steam reforming, the energy of the Rh K edge is between Rh metallic foil and oxide, suggesting the Rh cations are in the chemical state between foil and oxide. The ***r***-space spectrum of the Rh K edge contains two peaks in **Figure 4.8b**. The primary peak is assigned to the first shell coordination of Rh-O, while the 2nd shell is assigned to Rh-Rh bond. The fitting parameters of the r-space spectrum of this Rh-O bond are summarized in Figure 4.8c. TAs shown in the fitting parameters, a Rh atom bonds with another Rh atoms, forming a Rh-

Rh dimer. In addition, the fitting of r-space of the Rh K-edge suggests that Rh atoms bond with oxygen atoms. Thus, the in-situ EXAFS studies suggest that Rh atoms exist in the format of anchored Rh-Rh dimer on surface.

4.4 Summary

Catalysis of CeO_2 with anchored singly dispersed Rh cations was prepared, characterized and evaluated for the methane steam reforming. The single dispersion of Rh cations was confirmed via TEM, XRD, XPS, DRIFT CO spectrum and XAS. The catalytic performance of Rh_1/CeO_2 for steam reforming of methane was evaluated. By anchoring 0.17% of Rh on the surface, the catalytic activity of ceria catalyst increases greatly. The apparent energy barrier of steam reforming over Rh_1/CeO_2 catalyst is 40-45 kJ/mol, which is much lower than literature reported results. It suggests the catalysis of methane reforming on the singly dispersed Rh cations follows a pathway different from Rh NPs-based catalysts. Computational studies are being performed to gain fundamental understanding molecular mechanism of steaming reforming on this catalyst.

Chapter 5 Synergistic effect of Ru and Ni cations co-anchored on ceria for dry reforming of methane

5.1 Introduction

Methane, the major component of natural gas and shale gas, has attracted much attention in production of chemical intermediates for making liquid fuels and high value chemicals.[26, 43, 113, 139-141] Due to the increasing annual global production of shale gas, chemical industries have started to progressively switch their raw materials from crude oil to shale gas components. Reforming methane with CO_2 or H_2O has been the most important pathway since it produces syngas, one of the most important intermediates for producing liquid fuels and synthesizing high value chemicals through established industrial processes.[26, 113, 141-142]

The current industrial process of methane reforming on supported Ni metal nanoparticle catalysts undergoes at a temperature higher than 800°C.[143-145] Unfortunately, it faces two challenges. Firstly, the catalyst is readily deactivated due to sintering of supported metallic Ni nanoparticles at high temperature in environment of reducing gases ($CO+H_2$);[146] The sintering significantly decreases dispersion of Ni atoms of a catalyst. As the result, the number of exposed Ni atoms of the catalyst decreases dramatically. Secondly, a side reaction of methane pyrolysis readily occurs on surface of metallic Ni nanoparticles.[147-148] Due to very high binding energy of C atoms of CH_n (n=0-3) species on Ni atoms of metallic Ni nanoparticles, metallic Ni nanoparticles are very active for breaking C-H bond of methane. The rapid catalytic pyrolysis produces layers of carbon atoms on surface of Ni catalyst, which is also known as coke.[134, 149] The formation of coke completely blocks methane from accessing to Ni atoms of the catalyst, making the catalyst completely deactivated. In addition, the quite high catalytic temperature (800°C or higher) requests to input

significant amount of energy. Facing these challenges, it would be ideal if methane reforming can be done at lower temperature without coke formation.[150-152]

To avoid the formation of coke on surface of Ni catalysts, we propose to design a catalyst with low binding energy to the dissociated species of reactant such as CH_n (n=0-3) and intermediates. It was reported recently that binding energy of methane molecule on a metal atom at cationic state is typically lower than that on a metal atom at a metallic state[67, 125, 153-155]. Inspired by this understanding, it's proposed to anchor Ni atoms of cationic state instead of Ni atoms of metallic state to activate methane or CO_2 molecules, avoiding strong binding to CH_n (n=0-3) species. In addition, to spatially limit any potential coupling between carbon atoms or CH_n (n=0-3) species adsorbed on Ni atoms to form precursor of coke layer, Ni atoms are spatially separately anchored on surface in the format of single-atom sites.

Ru is active in activating CO_2 through dissociating C-O of CO_2 to CO.[16, 26, 114, 143-144, 152-153, 156] Thus, they are chosen as guest metal atoms to activate CO_2. Surface of CeO_2 has high density of oxygen vacancies.[151, 157-158] It is expected that its oxygen vacancies could participate into activation of CO_2. In addition, the high affinity of surface lattice oxygen atoms to metal atoms can stabilize these guest cations. Thus, CeO_2 was chosen as a support to anchor the two sets of single atoms, Ni_1 and Ru_1.

Catalysts consisting of CeO_2 nanorods and two sets of single-atom sites, Ni_1 or/and Ru_1 were successfully synthesized in this work. Operando studies of chemical and coordination environments during catalysis revealed that both Ni and Ru cations are singly dispersed and remained at cationic state during catalysis. This catalyst is highly active for reforming methane with CO_2. The selectivity for producing H_2 reaches 98.5% at 600^{o}C. Synergy effects between

single-atoms sites Ni_1 and Ru_1 were proved. Computational studies proposed a molecular mechanism for the synergy effects of Ni_1 and Ru_1 sites in reforming CH_4 with CO_2. This work opened an avenue in designing new catalysts with high activity and selectivity at a relatively low temperature.

5.2 Experimental section

5.2.1 Preparation of materials

The $Ce_{1-x-y}Ni_xRu_yO_2$ nanorod catalysts: The Ce-based nanorod oxides were synthesized by a hydrothermal method as literature reported. Ni and Ru cations were anchored on the lattice of CeO_2 during the synthesis of CeO_2 nanorods. Typically, 4 mmol of metal nitrite precursors were dissolve in 10 mL deionized water and then added to 70 mL of NaOH solution (6 mol/L) dropwisely under vigorous stirring. Precipitation was formed immediately as the mixing of two solution. After stirring for 30 mins at room temperature, the slurry was transferred to a stainless-steel autoclave (100 mL) with PTFE lining and maintained at 120 °C for 24 h. Then the autoclave was cooled to room temperature naturally. The solid product in the autoclave was separated by centrifugation and washed by water until the pH was neutral. Then the solid product was dried at 80 °C for 12 h. Finally, the product was grinded into fine powder and then calcined at 400 °C for 2 h in air.

5.2.2 Characterization

The transmission electron microscope (TEM), high-resolution transmission electron microscope (HR-TEM) images and high angle annular dark field (HAADF) images in STEM mode were taken using a FEI Tecnai F20 XT. Powder X-ray diffraction (XRD) patterns were recorded on a Rigaku

Ultimate IV operating in reflection mode with Cu Kα radiation that was monochromated with a secondary graphite monochromator. The nitrogen sorption measurements were performed on a Micromeritics (2010 unit) at 77 K.

Extended X-ray absorption fine structure spectrum (EXAFS) at Ru K-edge and Ni K-edge were collected in beamline 2-2, Stanford Synchrotron Radiation Laboratory (SSRL). The Ru and Ni K edge absorption were measured under fluorescence mode with Ge 13 element detector. Multiple scans were collected and averaged for analysis. The EXAFS signal amplitude factors were calibrated by Ni or Ru foil as the reference and then applied in the data analysis. Data analysis was performed with Demeter XAS package.[65] The obtained EXAFS data traces were calibrated and aligned carefully. ***r***-space of k^2 weight data was obtained from the Fourier transformation of k space in the range of 3~14 $Å^{-1}$.

The surface chemistry of catalyst was studied with the lab-based ambient pressure X-ray photoelectron spectrum (AP-XPS) system.[79] The reaction cell is integrated with a monochromated Al K-alpha X-ray source and energy analyzer. The mixture of reactant gases was introduced to the reaction cell through a gas manifold where all reactant gases were mixed and pressures were measured. The total pressure of reactant gases in the reaction cell was the average of the measured pressures by a capacitance gauge located between the gas manifold and tubing to the entrance port of the reaction cell and another capacitance gauge connected to tubing of exit port of the reaction cell. All gases used for AP-XPS studies had a purity of 99.99% or higher. Typically, the total flow rate of the mixture of pure reactant gases in the reaction cell is about 4 mL/min. To make sure that the average pressure of the gas in the reaction cell measured at the entrance and exit ports of the reaction cell represents the pressure of gas above the catalyst surface in the reaction cell, the distance between the sample surface and the aperture was kept twice or more of the aperture size

(0.8 mm). The distance was measured with a high-resolution video camera enhanced with an optical lens. The images of the aperture and sample surface shown on the same computer screen allow us to measure the sample-aperture distance by comparing the appeared sample-aperture distance to the appeared diameter of the aperture on the screen. The XPS data was analyzed by CasaXPS software. All the spectrum peaks were calibrated by Au $4f_{7/2}$ peak to 84.0 eV. The Ce*3d* spectrum was deconvoluted to components corresponding to Ce^{3+} and Ce^{4+}, respectively.[56-57] The oxygen vacancy ratio, or the Ce^{3+} ratio, was determined by the related peak areas.

5.2.3 Measurement of catalytic performance

The dry reforming of methane reactions was carried out in a fixed bed reactor with a quartz tube (inner diameter of 4 mm) which was filled with 0.05 g of catalysts and 0.5 g of quartz sand, mobilized by quartz wools. A K-type thermal couple was inserted to the fixed bed reactor and contacted with the quartz wools to monitor the actual temperature during reaction. Then a gas mixture of CH_4 and CO_2 (total flow rate 50 mL/min, the concentration of both reactants in the mixture is 0.5%) was introduced to the reactor by mass flow controller. The catalytic tests were carried out from 250 to 700 °C. The product gas components were analyzed by online gas chromatography equipped with a TCD detector. Catalytic activity is evaluated by calculated with the decrease (Δc_{CH4}) of CH_4 concentration on the downstream of fixed-bed flow reactor.

To determine the apparent activation energies, the kinetic experiments were carried out using 5 mg catalyst (unless otherwise mentioned) in a fixed-bed quartz reactor (ca. 4mm i.d.). Activation of the catalyst involved reductive treatment with hydrogen (10% in Ar, flow rate of 30 ml/min) at 300 ºC for 60 min. Kinetic experiments were conducted using appropriate feed flows to obtain significantly lower conversions (<20%) than those defined by thermodynamic equilibrium. The

reactant feed flows of CH_4 (1% in Ar) and CO_2 (1% in Ar) are 40 ml/min, respectively. The reaction was carried out over a temperature range of 500–560 ºC.

To determine the turnover frequency (TOF) of the methane reforming, the catalytic data in the kinetics-controlled regime further analyzed. The TOF in term of hydrogen production could be obtained from the hydrogen productivity (molecule per time) over number of active sites. The number of surface active sites was determined by the quantitative analysis of the AP-XPS data.[159]

5.2.4 DFT calculation

In this work, all the DFT calculations were carried out with a periodic slab model using the Vienna *ab initio* simulation program (VASP) [160-163]. The generalized gradient approximation (GGA) was used with the Perdew-Burke-Ernzerhof (PBE) [164] exchange-correlation functional. The projector-augmented wave (PAW) method [165-166] was utilized to describe the electron-ion interactions, and the cut-off energy for the plane-wave basis set was 450 eV. For the calculations of CeO_2, due to the strong correlation effect among the partially filled Ce 4f states, we used the Hubbard parameter, U, for the Ce 4f electrons to illustrate the on-site Coulomb interaction, which is the well-known DFT+U method [167]. According to previous work, the value of U-J of 4.5 eV [150] was applied on CeO_2. Furthermore, to illustrate the long-range dispersion interactions between the adsorbates and catalyst surfaces, we employed the D3 correction method by Grimme et al.[168]. Brillouin zone integration was accomplished using a 3×4×1 Monkhorst-Pack k-point mesh. All the adsorption geometries were optimized using a force-based conjugate gradient algorithm, while transition states (TSs) were located with a constrained minimisation technique [169-171]. According to the experiment results, CeO_2(110) was chosen; a typical surface model with a periodic six-layer p(1×2)

model with the 3 lower layers fixed and 3 upper layers relaxed were used. The entropy contributions of gas phase species including CO_2, CH_4, CO, and H_2 were evaluated using Shomate equation at 500°C, while the entropy contributions of adsorbates were ignored.

5.3 Results and discussion

5.3.1 Identification of the singly dispersed of the catalyst

Three type of catalysts Ru_1/CeO_2, Ni_1/CeO_2, and Ru_1+Ni_1/CeO_2 were prepared with a detailed, reproducible protocol. The loading concentration of Ru, Ni, and the Ru and Ni in the three catalysts are 5.0wt% for $Ce_{0.95}Ru_{0.05}O_2$, 5.0wt% $Ce_{0.95}Ni_{0.05}O_2$and 2.5wt%+2.5wt% for $Ce_{0.95}Ru_{0.025}Ni_{0.025}O_2$, respectively. Morphology and lattice fringes of used Ru_1/CeO_2, Ni_1/CeO_2, and Ru_1+Ni_1/CeO_2 catalyst were examined with HRTEM. Morphology and lattice fringe of used Ru_1/CeO2, Ni_1/CeO2, and Ru_1+Ni_1/CeO_2 were examined with TEM. As shown in **Figure 5.1**, the used Ru_1+Ni_1/CeO_2 remains the CeO_2 nanorod shape, suggesting that the catalyst has robust structural stability even after catalysis at 600-700 °C. The high resolution TEM images of used catalyst Ru_1+Ni_1/CeO_2 allow for identifying lattice fringes with spacing of 2.7 Å which corresponds to (200) planes of fluorite structure of CeO_2. It is noted that there is no any NiO or RuO_2 nanoparticles observed on the surface of nanorod oxides even at different orientations of rods of a catalyst, suggesting the Ru and Ni cations are highly dispersed.

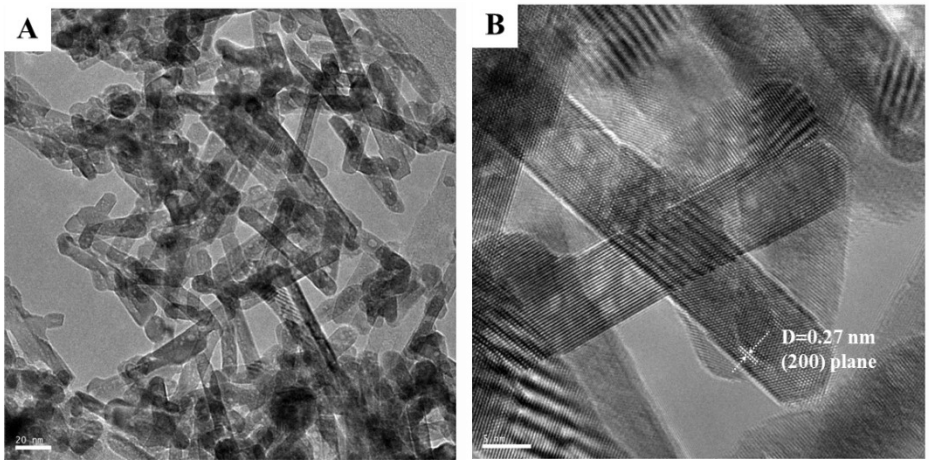

Figure 5.1 TEM (A) and HRTEM (B) images of used $Ce_{0.95}Ni_{0.025}Ru_{0.025}O_2$ catalyst after dry reforming of methane.

Aberration-corrected HAADF-STEM images of a used $Ce_{0.95}Ni_{0.025}Ru_{0.025}O_2$ catalyst is shown in **Figure 5.2**. The catalyst remains nanorod morphology after reaction in Figure 5.**2A**. **Figure 5.2B** provides clear two-dimension lattice fringe. with the inter-planar distance of the nanorod of the used catalyst $Ce_{0.95}Ni_{0.025}Ru_{0.025}O_2$ are 2.8 and 1.9 Å which correspond to the (200) and (220) planes of fluorite structure of CeO_2.[118] It could be deduced that the CeO_2 nanorods expose (110) plane on the surface, which is consistant with literatures. As Ni and Ru atoms have low atomic number than a Ce atom, it is challenging to distinguish Ni or Ru atoms from Ce atoms of CeO_2 nanorods by HAADF-STEM technique. Many efforts were made in checking whether NiO or/and RuO_2 could be supported on surface of CeO_2 nanorods. The catalysts nanoparticles were observed at different tilting angles of specimens during studies using HAADF-STEM. However, no any NiO or RuO_2 nanoparticles was observed on the surface of nanorod oxides even at different tilting angles of specimens. These structural characterizations of catalysts used for reforming CH_4 with CO_2 suggest that Ru and Ni cations are highly dispersed. In fact, they are singly dispersed. Their

single dispersions in terms of single-atom sites of Ni_1 and Ru_1 of these used catalysts were confirmed with operando studies using EXAFS to be presented in following sections

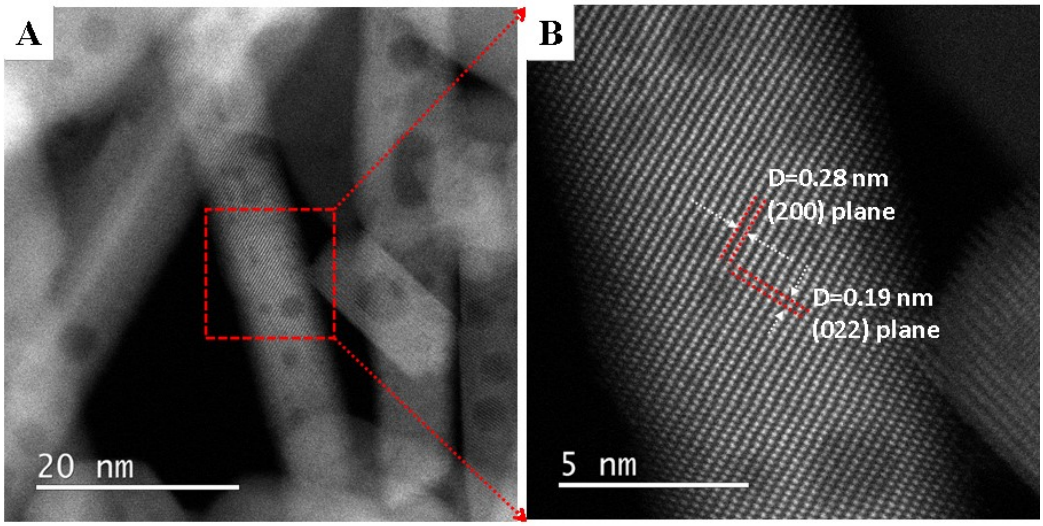

Figure 5.2 Aberration-corrected STEM images of used $Ce_{0.95}Ni_{0.025}Ru_{0.025}O_2$ catalyst for dry reforming of methane.

To confirm the crystal phase structures of $Ce_{1-x-y}Ni_xRu_yO_2$, XRD patterns were collected in **Figure 5.3**. The observed diffraction peaks of $Ce_{1-x-y}Ni_xRu_yO_2$ catalysts can be indexed to the (111), (200), (220), (311), (400), (331), (420) and (422) crystal panels, which correspond to a typical fluorite structure of CeO_2 (JCPDS 43-1002). As shown in **Figure 5.3**, no characteristic diffraction peaks belonging to NiO and RuO_2 nanoparticles were detected, confirming the single dispersion of Ni and Ru atoms in $Ce_{1-x-y}Ni_xRu_yO_2$ catalysts.

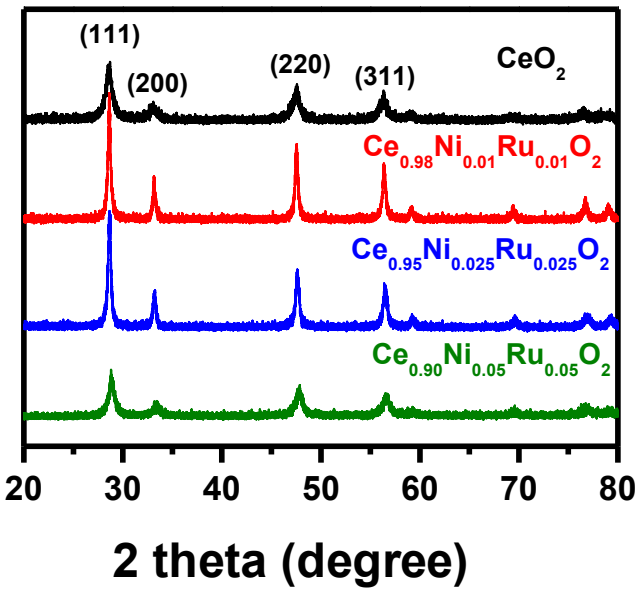

Figure 3 XRD patterns of $Ce_{1-x-y}Ni_xRu_yO_2$ catalysts: CeO_2, $Ce_{0.95}Ni_{0.05}O_2$, $Ce_{0.95}Ru_{0.05}O_2$ and $Ce_{0.95}Ni_{0.025}Ru_{0.025}O_2$.

5.3.2 Catalytic performance of Ru and Ni cations on ceria support

The catalytic performances of $Ce_{1-x-y}Ni_xRu_yO_2$ catalysts for dry reforming of methane in terms of conversion of CH_4 and selectivity for production of H_2 and ratio of H_2 to CO were studied with a fixed-bed flow reactor in the temperature range of 250-600°C. CH_4 decomposition reaction and reverse water–gas shift reaction are two side reactions which potentially decreases selectivity for production of ideal products H_2 and CO. As shown in **Figure 5.4**, the H_2 selectivity of $Ce_{0.95}Ni_{0.05}O_2$ and $Ce_{0.95}Ru_{0.05}O_2$ catalysts for dry reforming of methane are 80.0 and 82.9% respectively. Compared to $Ce_{0.95}Ni_{0.05}O_2$ and $Ce_{0.95}Ru_{0.05}O_2$, $Ce_{0.95}Ni_{0.025}Ru_{0.025}O_2$ exhibits a higher selectivity of 98.5% for producing of H_2 at 600°C. In addition, the conversion of CH_4 on 50 mg $Ce_{0.95}Ni_{0.025}Ru_{0.025}O_2$ is obviously higher than the average of conversions on 50 mg

$Ce_{0.95}Ru_{0.05}O_2$ and that of 50 mg of $Ce_{0.95}Ni_{0.05}O_2$ (**Figure 5.5b**). It suggests a synergy effect of Ni and Ru cations on reforming CH_4 with CO_2. Here we assume that the number of sites (Ni_1 or Ru_1) on topmost layer of CeO_2 is proportional to the nominal composition of the three catalysts. In other words, we assume that the numbers of Ni_1 and Ru_1 sties of $Ce_{0.95}Ni_{0.025}Ru_{0.025}O_2$ are half of the number of Ni_1 sites of $Ce_{0.95}Ni_{0.05}O_2$ and half of the number of Ru_1 sites of $Ce_{0.95}Ni_{0.05}O_2$, respectively. In addition, the yield of H_2 over $Ce_{0.95}Ni_{0.025}Ru_{0.025}O_2$ at 600ºC (90%) is much higher than half of total yield of $Ce_{0.95}Ni_{0.05}O_2$ (65%) and $Ce_{0.95}Ru_{0.05}O_2$ (52%), 58.5% ($=\frac{65\%+50\%}{2}$).

To confirm the synergistic effect, three catalysts $Ce_{0.90}Ni_{0.05}Ru_{0.05}O_2$, $Ce_{0.90}Ni_{0.10}O_2$, and $Ce_{0.90}Ru_{0.10}O_2$ with higher doping level of Ni and Ru cations than $Ce_{0.95}Ni_{0.025}Ru_{0.025}O_2$, $Ce_{0.95}Ni_{0.05}O_2$ and $Ce_{0.95}Ru_{0.05}O_2$ were synthesized and their catalytic performances were measured. As shown in **Figures 5.4b1**, the conversion of CH_4 on 50 mg $Ce_{0.90}Ni_{0.05}Ru_{0.05}O_2$ (98%) is obviously higher than half of the total of conversions of 50 mg of $Ce_{0.90}Ru_{0.10}O_2$ (96.5%) and that of 50 mg of $Ce_{0.90}Ni_{0.10}O_2$, (65%), 81% ($=\frac{96.5\%+65.0\%}{2}$). This difference also suggests a synergic effect between Ni and Ru sites on $Ce_{0.90}Ni_{0.05}Ru_{0.05}O_2$ during dry reforming, which is similar to $Ce_{0.95}Ni_{0.025}Ru_{0.025}O_2$.

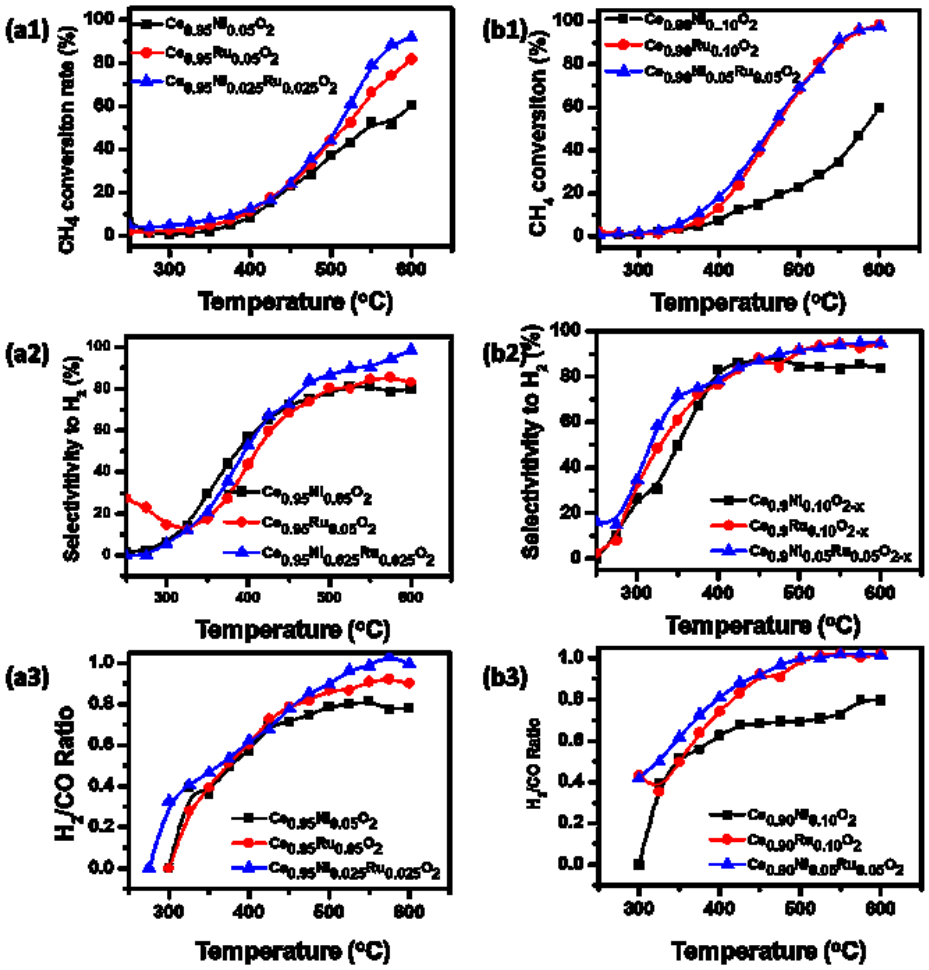

Figure 5.4 Catalytic performance of $Ce_{0.95-x-y}Ni_xRu_yO_2$ catalysts for dry reforming of CH_4. (a) conversion of CH_4, (b) selectivity to product of H_2, and (c) H_2/CO ratio.

To explore whether the observed syndetic effect is an intrinsic phenomenon or just the matter of number of sites of the three catalysts, kinetics of these catalysts was studied in parallel. **Figure 5.5** presents Arrhenius plots of $Ce_{0.95}Ni_{0.05}O_2$ and $Ce_{0.95}Ru_{0.05}O_2$ and $Ce_{0.95}Ni_{0.025}Ru_{0.025}O_2$ in the temperature range of 500°C to 560°C. All conversions are lower than 20% in the temperature range of kinetics studies. Y axis of **Figure 5.5** is the production rate of H_2 or CO (number of molecules produced per site per second). Apparent activation barriers were calculated through the slopes of

these plots in **Figure 5.5**. Notably, based on production of H_2 the measured activation barrier of $Ce_{0.95}Ni_{0.025}Ru_{0.025}O_2$ (51.7 kJ/mol) is obviously lower than those of $Ce_{0.95}Ni_{0.05}O_2$ (66.0 kJ/mol), and $Ce_{0.95}Ru_{0.05}O_2$ (75.6 kJ/mol). Based on production of CO, the measured activation barrier of $Ce_{0.95}Ni_{0.025}Ru_{0.025}O_2$ (41.5 kJ/mol) is obviously lower than those of $Ce_{0.95}Ni_{0.05}O_2$ (61.2 kJ/mol), and $Ce_{0.95}Ru_{0.05}O_2$ (71.3 kJ/mol). This intrinsic difference in dry reforming between $Ce_{0.95}Ni_{0.05}O_2$ (or $Ce_{0.95}Ru_{0.05}O_2$) and $Ce_{0.95}Ni_{0.025}Ru_{0.025}O_2$ confirmed the synergy effect between anchored Ni and Ru cations; this synergy effect of Ni_1 an Ru_1 sites on $Ce_{0.95}Ni_{0.025}Ru_{0.025}O_2$ obviously decreases the activation energy barriers for reforming methane with CO_2.

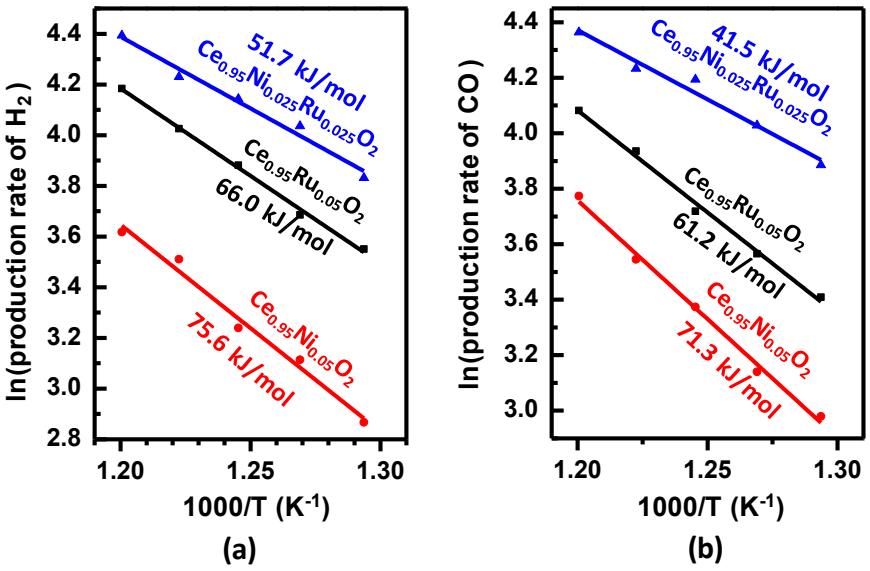

Figure 5.5 the Arrhenius plot of the activation energy barrier in term of the rate to produce (a) H_2 and (b) CO catalyzed by the $Ce_{1-x-y}Ni_xRu_yO_2$ catalysts: (blue) $Ce_{0.95}Ni_{0.025}Ru_{0.025}O_2$, (black) $Ce_{0.95}Ru_{0.05}O_2$ and (red) $Ce_{0.95}Ni_{0.05}O_2$.

Notably, the activation barrier for producing CO and H_2 are different for the same catalyst suggest that some of the rate-determining steps for producing CO and those for producing H_2 are different. For a catalytic cycle, typically there could be more than one rate-determining steps which

exhibits similar barrier. However, how these rate-determining steps collectively give an apparent activation barrier is still a debatable topic in the field of computational and experimental studies. Thus, the complexity of rate-determining steps for CO and H_2 likely results in difference between their measured apparent activation barriers.

It is noted that the selectivity for producing H_2 on $Ce_{0.95}Ru_{0.05}O_2$ at <340°C is higher than on $Ce_{0.95}Ni_{0.05}O_2$ (Figure 4b). It could result from a potential complicated restructuring. For instance, it is possible that Ru atoms of $Ce_{0.95}Ru_{0.05}O_2$ at <340°C are exposed on surface but Ni atoms of $Ce_{0.95}Ni_{0.05}O_2$ are buried in subsurface at <340°C. In other words, the exposed Ru atoms of $Ce_{0.95}Ru_{0.05}O_2$ at <340°C played a role in production of H_2 and thus gave a relatively high selectivity for producing H_2; but the buried Ni atoms of $Ce_{0.95}Ni_{0.05}O_2$ at <340°C did not play a role for producing H_2. Thus, the selectivity for producing H_2 on $Ce_{0.95}Ni_{0.05}O_2$ is lower than $Ce_{0.95}Ni_{0.025}Ru_{0.025}O_2$ at <340°C. For catalysis temperature higher than 340°C, it is possible that the buried Ni of $Ce_{0.95}Ni_{0.05}O_2$ migrates to surface and thus play a role in production of H_2; thus at a temperature higher than 340°C, both Ru of $Ce_{0.95}Ru_{0.05}O_2$ and Ni of $Ce_{0.95}Ni_{0.05}O_2$ are exposed on surface and thus played a role in producing H_2. This is one of the possible explanations. It is noted that the observation of "abnormal" selectivity for producing H_2 at <340°C is not relevant to the synergistic effect at 550-600°C.

As shown in Figure 4c, the ratio of H_2/CO increases as a function of catalysis temperature, which is consistent with the evolution of equilibrium H_2/CO ratio of CH_4 dry reforming as a function of temperature calculated with ASPEN. ASPEN was used to calculate the equilibrium H_2/CO ratio at different temperature when H_2O was considered as a product other than H_2 and CO. In these ASPEN calculations, we built a fixed-bed flow reactor and input the initial concentrations of CH_4, 0.5% and CO_2, 0.5%. Figure S5 plots the calculated conversion of CH_4 as a function of

temperatures in 300-600ºC. At 600ºC, the conversion of CH_4 is 97%. The calculated ratios of H_2/CO were plotted in Figure S6. They increase as a function of catalysis temperature. At 600ºC, it reaches 0.98. The evolution of calculated H_2/CO ratio as a function of temperature (Figure S6) is in agreement with the one measured (Figure 4c). This consistence suggests that reverse water gas shift did participate into the dry reforming.

Turnover frequency (TOF) of reforming methane with CO_2 over these catalysts were calculated with yields of H_2 and CO measured under kinetics-controlled regime. For catalysts $Ce_{0.95}Ni_{0.05}O_2$ and $Ce_{0.95}Ni_{0.05}O_2$, numbers of Ni or Ru atoms on the topmost layer of the catalyst surface was used as denominator in the calculation of TOF. In the case of $Ce_{0.95}Ni_{0.025}Ru_{0.025}O_2$, all Ni and Ru on the topmost layer of this catalyst were counted as active sites of reforming CH_4 in the calculations of TOF. As shown in **Figure 5.6**, the TOF of $Ce_{0.95}Ni_{0.025}Ru_{0.025}O_2$ is definitely higher than $Ce_{0.95}Ni_{0.05}O_2$ and $Ce_{0.95}Ru_{0.05}O_2$ at the same temperature in the temperature range (500-560ºC), further confirming the synergy effect between Ru_1 and Ni_1 sites in reforming CH_4 with CO_2.

The distance between Ni and Ru cations of $Ce_{1-x-y}Ni_xRu_yO_2$ is expected to be a factor influencing catalytic performance. To address how a relative distance between Ni and Ru on CeO_2 influence catalytic performance, a much larger variation in concentration of Ni (or Ru) on two catalysts is necessary. To largely decrease the relative distance, one has to increase the loading largely. Unfortunately, Ni (or Ru) at high loading can readily form metal or oxide nanoparticles, which prevents us from studying synergistic effect between two sets of single atom sites at high loading. To largely increase the relative distance, one has to decrease the loading of single atoms largely. However, it is quietly challenging in characterizing chemical and coordination environments of these single atom sites if the loading of Ni or Ru is too low. Facing

these challenges, how the distance between Ni and Ru cations could influence the synergetic effect was not explored here.

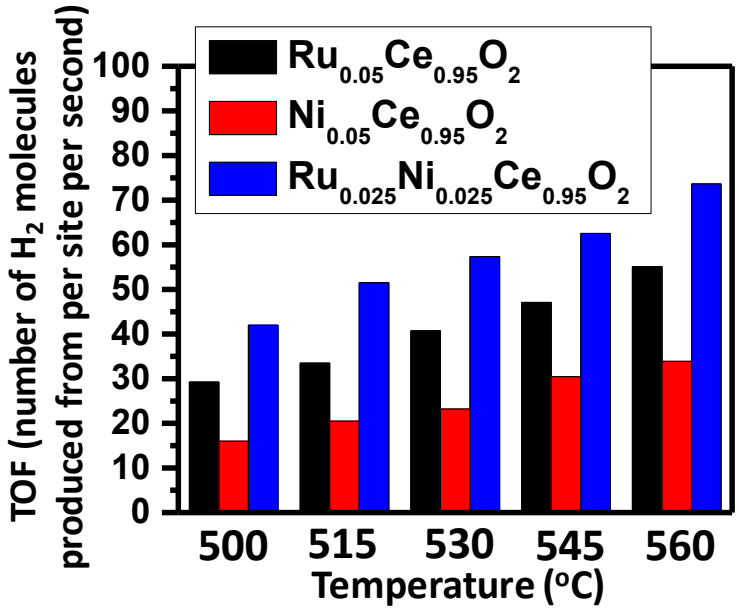

Figure 5.6 Turnover frequency (TOF) of reforming CH_4 with CO_2 in term of hydrogen production

5.3.3 In-situ/operando studies of the surface chemistry

Surface chemistry of catalysts during catalysis was investigated by AP-XPS. Based on literature,[56, 58] one of the photoemission features of Ce^{3+} is at 885.2 eV which does not overlap with photoemission features of Ce^{4+} of CeO_2.[56, 58] As shown in **Figure 5.7a1**, there is lack of this photoemission feature of Ce^{3+} at 885.2 eV. It suggests that the fraction of Ce^{3+} in surface region before catalysis is quite low, forming a valley in the region of 885.2±1.5 eV. Compared to the catalyst before catalysis, the concentrations of Ce^{3+} during catalysis at 450°C and 550°C are obviously higher than that before catalysis, evidenced by the formation of a plateau in the region of 885.2±1.5 eV (**Figures 5.7a2** and **5.7a3**) instead of a valley-like feature (**Figure 5.7a1**). The

$Ce^{3+}/(Ce^{3+}+Ce^{4+})$ is 2.3%, 19.2% and 20.2% at **Figure 5.7a1**, **5.7a2** and **5.7a3**, respectively. In terms of O *1s* feature before catalysis, the majority oxygen species are surface lattice oxygen. A component at 532.0 eV in O1s spectrum of the fresh catalyst (**Figure 5.7b1**) was observed and assigned to surface -OH group.[56, 172] It is formed through dissociative chemisorption of water molecules on oxygen vacancies in the cooling process in air upon calcination at a high temperature during catalyst preparation (**Figures 5.7b2** and **5.7b3**). The atomic fraction of these hydroxyl group species decreased along the increase of catalysis temperature. Because Ru 3d overlaps with C1s, Ru 3p spectra were collected here to analyze Ru. As shown in the **Figure 5.7c1**, Ru is at oxidizing state in the fresh catalyst of $Ce_{0.95}Ni_{0.025}Ru_{0.025}O_2$. When the catalyst was under catalysis conditions (**Figure 5.7c2** and **5.7c3**), binding energies of Ru 3p decreased and downshift to the side of lower binding energy. This downshift of binding energy of Ru 3p indicates increase of electron density of Ru atoms. This is due to a partial reduction of Ru atoms or change of chemical or/and coordination environment of Ru atoms to an environment of Ru with a higher electron density. Notably, the binding energy (462.4 eV) of Ru 3p of Ru atoms during catalysis at 550°C (**Figure 7c3**) is still higher than the metallic Ru 3p, which is 416.7 eV;[173] it suggests that Ru atoms of $Ce_{0.95}Ni_{0.025}Ru_{0.025}O_2$ are at cationic state.

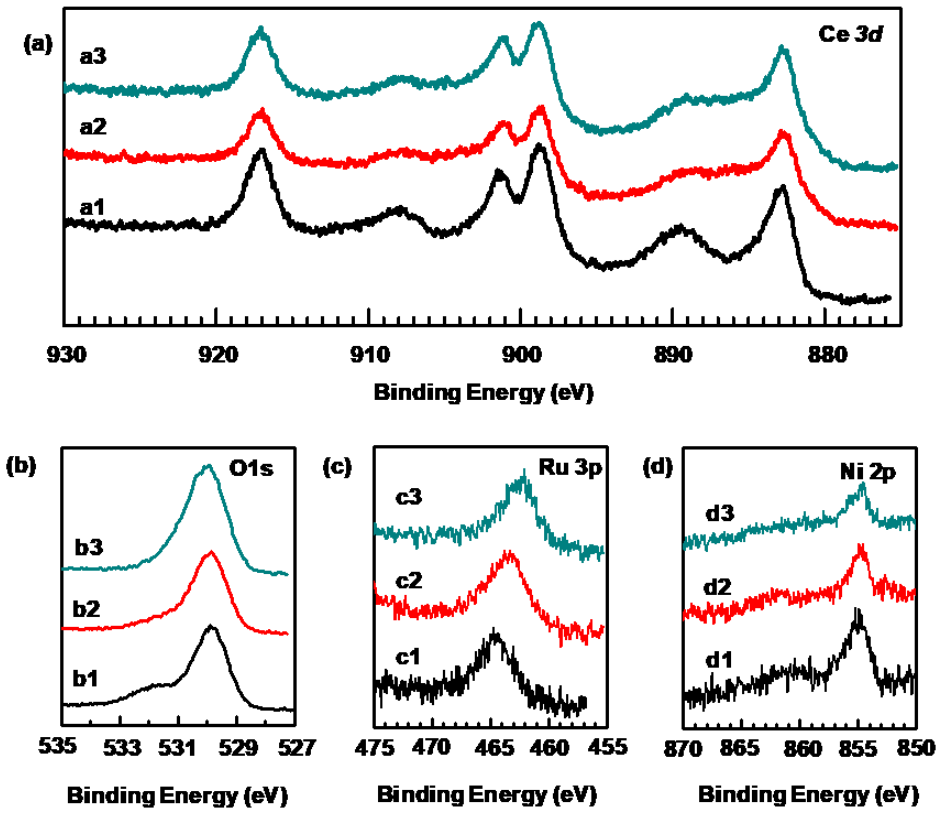

Figure 5.7 Ce3d, O1s, Ru3p, and Ni2p photoemission features from AP-XPS studies of $Ce_{0.95}Ni_{0.025}Ru_{0.025}O_2$ during reforming CH_4 with CO_2: (a1, b1, and c1) before catalysis, (a2, b2, and c2) 450ºC and (a3, b3, and c3) 550ºC. The reactant mixture is composed by 0.5 Torr CO_2 and 0.5 Torr CH_4.

Figure 5.7d presents the Ni 2p 3/2 of $Ce_{0.95}Ni_{0.025}Ru_{0.025}O_2$ collected under different conditions. Photoemission feature of Ni 2p1/2 was not shown in this figure so that photoemission feature of Ni 2p3/2 can be presented clearly. Although a slight down shift of Ni 2p 3/2 was observed during catalysis compared to that before catalysis, Ni atoms of this catalyst during catalysis with Ni 2p3/2 at 854.8 eV remained at an oxidation state based on binding energy of Ni 2p photoelectrons of NiO at 853.8 eV.[55] In the case of NiO nanoparticles, a very strong satellite peak of Ni 2p 3/2 was clearly observed at 861.4 eV[55]; this satellite peak is originated from long

range scattering of structure of .....Ni-O-Ni-O-Ni-O.... in lattice of a NiO nanoparticle whose surface has interdigitated Ni and O atoms.[156, 174-175] It can be used to judge whether there is Ni-O-Ni structure or not. In our previous studies, Ni 2p3/2 of singly dispersed Ni atoms in micropore of ZSM-5[18] and on surface of $Co_{2.25}Ni_{0.75}O_4$ nanoparticles does not exhibit such a satellite peak.[156] Thus, here the lack of satellite peak next to the Ni 2p3/2 main peak (**Figure 5.7d3**) suggests that Ni atoms during catalysis at 550^{o}C are singly dispersed instead of formation of NiO lattice.

These AP-XPS studies clearly suggest that Ni ad Ru atoms in $Ce_{0.95}Ni_{0.025}Ru_{0.025}O_2$ during catalysis are in cationic state instead of metallic state.[65] It was confirmed by in situ/operando studies of chemical and coordination environments of Ni and Ru atoms during catalysis. From the feature of near edge absorption of Ru K edge and Ni K edge collected during catalysis, Ru and Ni atoms of $Ce_{0.95}Ni_{0.025}Ru_{0.025}O_2$ during catalysis are at cations states (**Figures 5.8a** and **5.8b**). ***r***-space spectra of Ni K edge and Ru K edge obtained from EXAFS studies of $Ce_{0.95}Ni_{0.025}Ru_{0.025}O_2$ during catalysis show that Ni and Ru atoms are singly dispersed and coordinated with oxygen atoms during catalysis. The fitting results of the Fourier transformed radical distribution functions (**Figure 5.8c** and **5.8d**) suggest that Ru and Ni are coordinated with O in the first shell and Ce in the second shell during catalysis. As shown in **Figure 5.8i**, the fittings of ***r***-space of Ni K-edge suggest that (1) each Ni atom bonds with three oxygen atoms on average in the first coordination shell, (2) the distance between Ni and O is 1.90±0.02 Å , (3) each Ni atom coordinates with three Ce atoms in the closest second coordination shell (Ni-O-Ce), and (4) the direct distance between Ni and Ce in Ni-(O)-Ce is 3.10±0.07 Å. Similar fitting of ***r***-space of Ru K-edge suggest that (1) each Ru atom bonds with about four oxygen atoms in the first coordination shell, (2) the direct distances between Ru and O are 1.86±0.06 Å or 2.11±0.05 Å, respectively which are close to the 1.90±0.02 Å of Ni-O; (3) each Ru atom coordinates with three Ce atoms in the closest second

coordination shell (Ru-O-Ce), and (4) the direct distance between Ru and Ce in Ru-(O)-Ce is 2.78±0.02 Å which is still a reasonable distance since the ionic radii of Ru and Ce are 0.82 Å and 1.15 Å, respectively[176] and the ∠Ru-O-Ce is about 55°.

The coordination number and bond distance of Ni_1 and Ru_1 uncovered with operando EXAFS studies (**Figure 5.8i**) are consistent with the geometries of Ni_1 and Ru_1 sites on surface of CeO_2 (110) optimized with DFT (**Figure 5.9**). Obviously, the ***r***-space spectra of Ru K edge and Ni K edge do not support the existence of the second shell in terms of Ru-O-Ru or Ni-O-Ni structure. Thus, we concluded that Ru and Ni cations are in the format of single atoms singly dispersed on CeO_2 during catalysis instead of formation of NiO, RuO_2, metallic Ni nanoparticles, or metallic Ru nanoparticles.

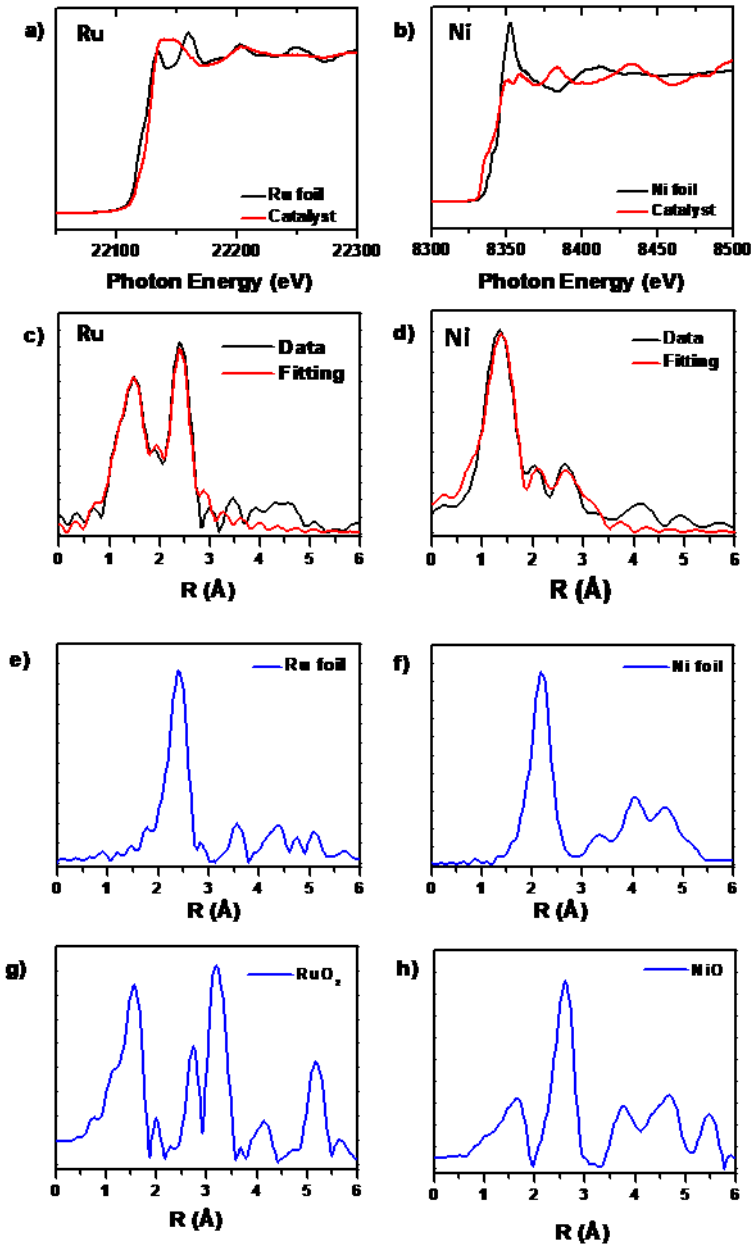

	CN	Distance (Å)	ss
Ru-O	2.08±0.65	1.86±0.06	0.00200
Ru-O	2.41±0.63	2.11±0.05	0.00200
Ru-(O)-Ce	2.73±0.40	2.78±0.02	0.00200
Ni-O	3.38±0.35	1.90±0.02	0.00456
Ni-(O)-Ce	2.80±0.85	3.10±0.07	0.00828

(i)

Figure 5.8. Operando studies of $Ru_{0.025}Ni_{0.025}Ce_{0.95}O_2$ during catalysis and reference samples (Ni foil, Ru foil, NiO powder and RuO_2 powder) using X-ray absorption spectroscopy (XANES and EXAFS) and corresponding Fourier transformed radical distribution function of Ru K edge and Ni Kedge. (a) Energy space of Ru K edge of $Ru_{0.025}Ni_{0.025}Ce_{0.95}O_2$ and Ru foil reference; (b) energy space of Ni K edge of $Ru_{0.025}Ni_{0.025}Ce_{0.95}O_2$ and Ni foil reference. (c) Experimental (black) and fitting (red) **r**-space spectra of Ru K edge of $Ru_{0.025}Ni_{0.025}Ce_{0.95}O_2$. (d) Experimental (black) and fitting (red) **r**-space spectra of Ni K edge of $Ru_{0.025}Ni_{0.025}Ce_{0.95}O_2$. (e) r-space spectrum of reference sample Ru foil. (f) r-space spectrum of reference sample Ni foil. (g) r-space spectrum of reference sample NiO. (h) r-space spectrum of reference sample RuO_2. All r-space spectra are shown without phase correction. (i)Coordination environments of Ni_1 and Ru_1 atoms of $Ru_{0.025}Ni_{0.025}Ce_{0.95}O_2$ during catalysis.

5.4 DFT calculation

5.4.1 Different doping sites of Ni_1 and Ru_1 atoms

(110) of CeO_2 is the preferentially exposed surface of a $Ru_{0.025}Ni_{0.025}Ce_{0.95}O_2$ based on the above HRTEM studies. Thus, (110) surface of CeO_2 nanorods was chosen to build structural model for simulating activation of CH_4 and CO_2 on $Ru_{0.025}Ni_{0.025}Ce_{0.95}O_2$. Four potential doping sites for both Ru_1 and Ni_1 on CeO_2, respectively were optimized. The most stable doping sites are shown in **Figure 5.9**. Chemical and coordination environments of Ni_1 and Ru_1 atoms of the most stable sites from optimization with DFT (**Figure 5.9**) were listed in **Table 5.1**. These bonding parameters (**Table 5.1**) are in good agreement with the coordination environments measured through operando EXAFS studies of Ni K-edge and Ru K-edge (**Figure 5.8i**). Therefore, the optimized surface structure in **Figure 5.9** was used for simulating activations of methane and CO_2 molecules to form CO and H_2 in dry reforming.

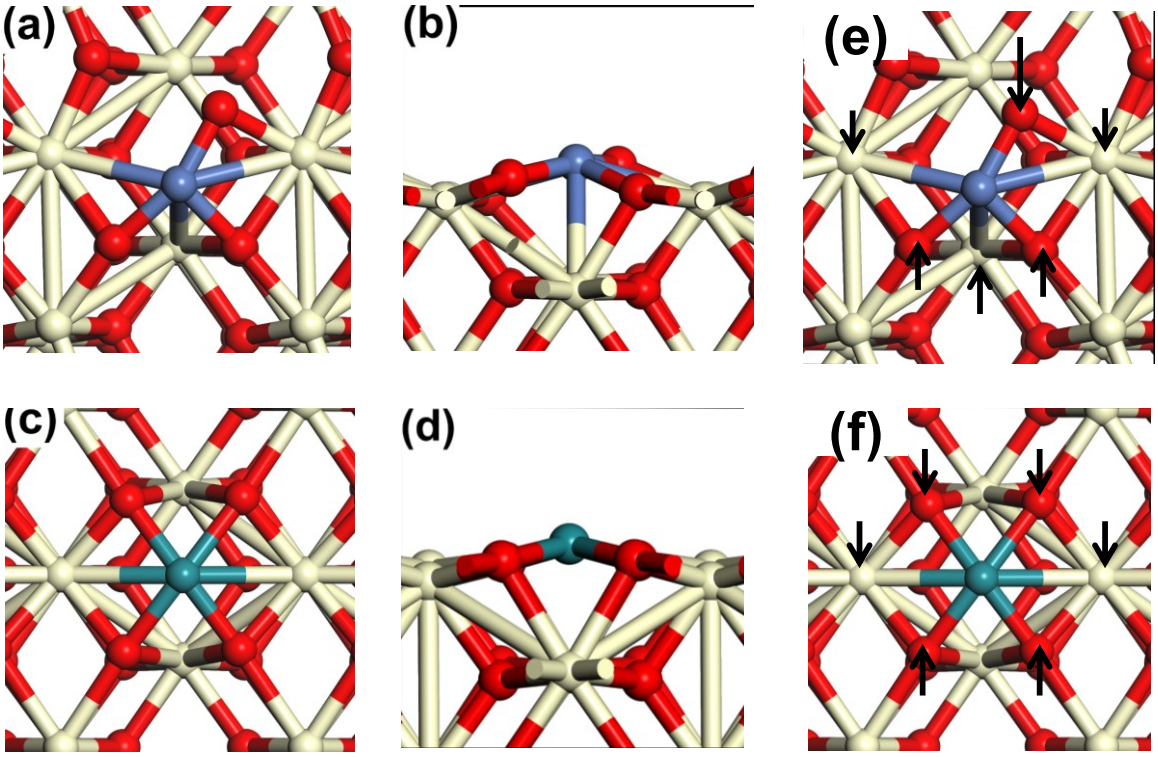

Figure 5.9 The most stable surface structure representing surface of $Ru_{0.025}Ni_{0.025}Ce_{0.95}O_2$ during catalysis. (a) Top view of CeO_2 (110) anchored with a Ni_1 atom. (b) Side view of CeO_2 (110) anchored with the Ni_1 atom. (c) Top view of CeO_2 (110) anchored with a singly dispersed Ru_1 atom. (d) Side view of CeO_2 (110) anchored with the singly dispersed Ru atom. (e) The marked neighbor atoms (black arrows) coordinated with Ni_1 site. (f) The marked neighbor atoms (black arrows) coordinated with Ru_1 site. Ce, Ni, and Ru are shown in yellow, blue, and green, respectively. Red balls stand for oxygen atoms. These notations are used throughout this work. It is the most stable surface among four optimized surface structure with different binding environment of Ni_1 and Ru_1 atoms.

Table 5.1 Coordination number (CN) and distances of Ni-O and Ni-Ce of $Ni@CeO_2$, and Ru-O and Ru-Ce of $Ru@CeO_2$.

		CN	Distance
$Ni@CeO_2$	Ni-O	3	1.89

	Ni-Ce	3	2.94
$Ru@CeO_2$	Ru-O	4	2.15
	Ru-Ce	2	2.82

5.4.2 Activation of the first C-H of CH_4

Activation of methane is one of the most important elementary steps in catalytic transformation of CH_4 according to previous work[177-178]. Based on the models shown in **Figure 5.9**, here dissociative chemisorption of methane on Ru_1 and Ni_1 sites were investigated. Geometries of the most favorable transition states in activation of the first C-H of methane on Ni_1 atom and Ru_1 atom are shown in **Figures 5.10a** and **10b** (for Ni_1), and **Figures 5.10c** and **5.10d** (for Ru_1), respectively. Based on the DFT calculations, Gibbs free energy barriers for activations of the first C-H of CH_4 on Ni_1 and Ru_1 sites are 1.88 eV and 2.01 eV, respectively. These values suggest that Ni_1 is the preferred active site for activating the first C-H of methane since the barrier on Ni_1 is relatively lower in contrast to Ru_1. In fact, the activation barrier of C-H of methane on the Ni_1, 1.88 eV is low in contrast to the activation barriers of the first C-H of methane on other catalysts,[134] which is consistent with the quite high activity of dry reforming at a relatively low temperatures observed in this work. The formed CH_3 and H adsorb on Ni atom and surface lattice oxygen, respectively (**Figures 5.10e-10f**).

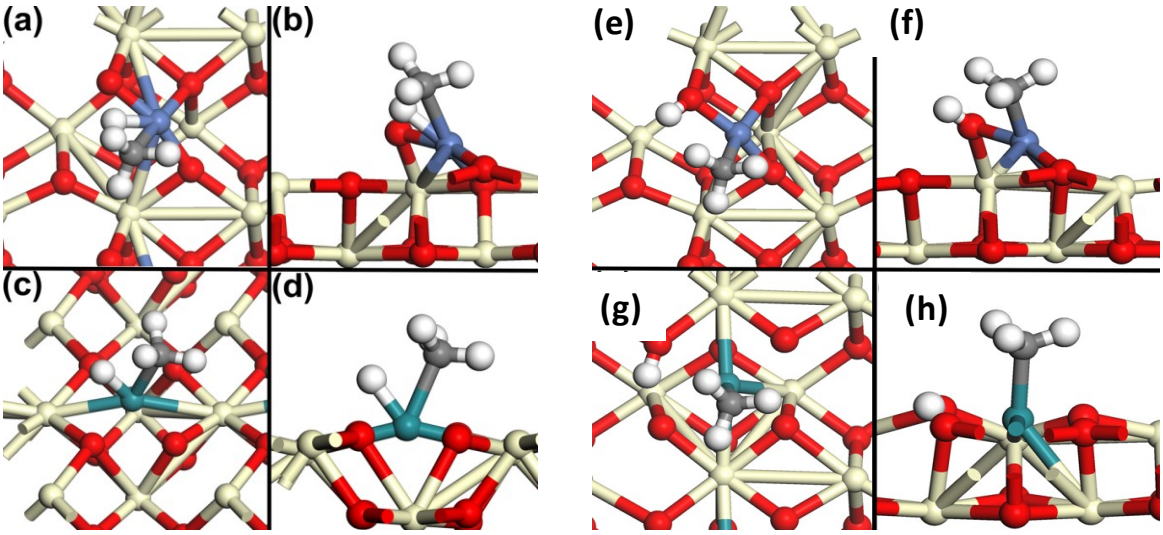

Figure 5.10. Top views and side views of transition state geometries of CH_4 activation and intermediate structures of formed CH_3 and H on Ni_1 and Ru_1 sites on CeO_2. (a and b) Top and side views of transition state geometries of CH_4 activation on Ni_1. (c and d) Top and side views of transition state geometries of CH_4 activation on Ru_1. (e and f) Top and side views of intermediate geometries of CH_3 and H formed on Ni_1 site. (g and h) Top and side views of intermediate geometries of CH_3 and H formed on Ru_1 site.

5.4.3 Transformation of CH_3 to CO and H

In dry reforming, the coupling of surface hydrogen species to form hydrogen molecule are likely to be in equilibrium.[178] Transformation of CH_4 to CO can be done through four dehydrogenation steps to form atomic carbon and then oxidation of atomic carbon to CO. Due to mobility of surface lattice oxygen atoms, the possibility of coupling between oxygen atom of surface lattice and carbon atom formed through activation of methane was considered here.

After the formation of CH_3 species, two different types of reactions including (1) dehydrogenation of CH_3 into CH_2 and H and (2) oxidation of CH_3 to CH_3O are possible pathways to transform CH_3 to CO. Both of them were investigated here. The transition state geometries of

these two potential steps on Ni_1 site and Ru_1 site are shown in **Figure 5.11a-d** and **Figure 5.11e-h**, respectively. The calculated activation energies of CH_3 dehydrogenation performed on Ni_1 site (**Figures 5.11a** and **5.11b**) and CH_3 oxidation on Ni_1 site (**Figure 5.11c** and **5.11d**) are 1.39 eV and 1.33 eV, respectively. Therefore, the dehydrogenation of CH_3 into CH_2 and H on Ni_1 site and oxidation of CH_3 to CH_3O on Ni_1 site are kinetically similar. However, the free energy changes for dehydrogenation of CH_3 on Ni_1 site and oxidation of CH_3 to CH_3O on Ni_1 site are 0.50 eV and -0.03 eV, respectively. Thus, in terms of Ni_1 site, the oxidation of CH_3 to CH_3O on Ni_1 site is likely to be the dominant pathway in contrast to the dehydrogenation of CH_3 into CH_2 and H.

Dehydrogenation of CH_3 to CH_2 or oxidation of CH_3 on Ru_1 site were investigated as well. The activation barrier and enthalpy change of dehydrogenation of CH_3 to CH_2 and H on Ru_1 site are 1.73 eV and 0.69 eV, respectively, while the barrier and free energy change for oxidation of CH_3 to CH_3O on Ru_1 site are 2.22 eV and 0.58 eV, respectively. Thus, obviously the dehydrogenation of CH_3 to CH_2 and H on Ru_1 site are kinetically favorable in contrast to oxidation of CH_3 to CH_3O on Ru_1. Compared to the dehydrogenation of CH_3 to CH_2 on Ru_1 with activation barrier of 1.73 eV and free energy change of 0.69 eV, the oxidation of CH_3 to CH_3O on Ni_1 (with activation barrier of 1.33 eV and free energy change of -0.03 eV) is favorable. Thus, upon the activation of the first C-H of CH_4, a favorable step is the oxidation of CH_3 to CH_3O on Ni_1.

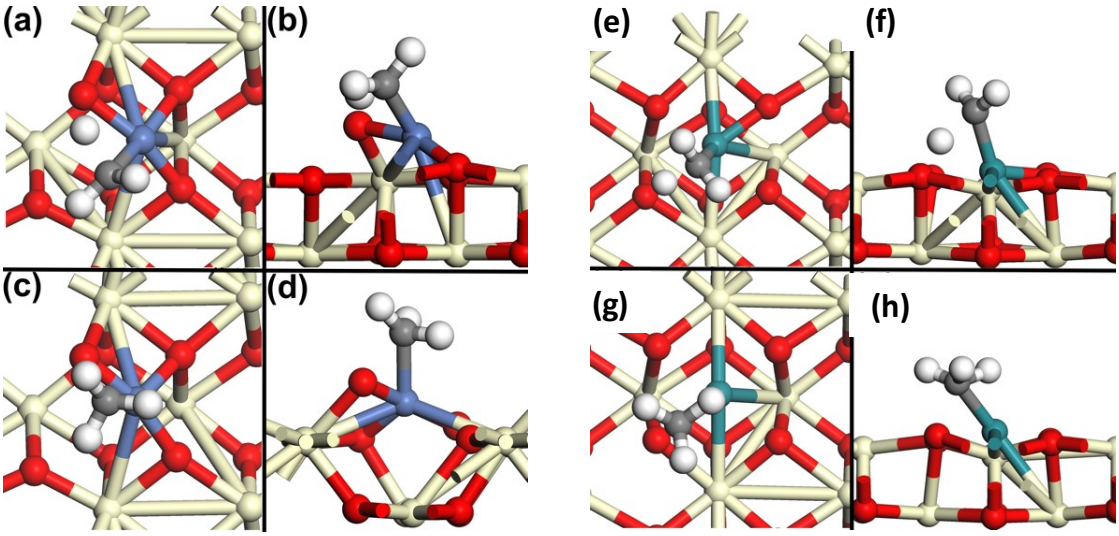

Figure 5.11. Top views and side views of transition state geometries of CH_3 dehydrogenation or CH_3 oxidation on Ni_1 or Ru_1 site on CeO_2. (a and b) Top and side views of transition state geometry of CH_3 dehydrogenation on Ni_1. (c and d) Top and side views of transition state geometry of CH_3 oxidation on Ni_1. (e and f) Top and side views of transition state geometry of CH_3 dehydrogenation on Ru_1. (g and h) Top and side views of transition state geometry of CH_3 oxidation on Ru_1.

With similar methods, all possible dehydrogenation and oxidation steps of CH_2, CH and C to CO on Ni_1 and Ru_1 sites were systematically investigated. The favorable pathways from activation of the first C-H of CH_4 to formation of CO on Ni_1 sites are listed in **Table 5.2**. In addition, **Table 5.2** lists the favorable pathways from activation of CH_4 to the formation of CO on Ru_1 site. As shown in the second column from the left side of **Table 5.2**, CH_3O is further dehydrogenated to CH_2O with a free energy barrier of 1.52 eV and free energy change of 1.04 eV.

After the 3rd step in **Table 5.2**, most of the dehydrogenation steps are favorable with low free energy barriers and negative free energy changes on a Ru_1 site. In addition, the desorption steps of CO from Ni_1 site and Ru_1 site are endothermic and barrierless (step 6 in **Table 5.2**). The bonding of CO on Ru_1 site is much stronger than Ni_1 site, which may result in high coverage of

CO on Ru_1 site and therefore limit the reaction rate. In general, the activation energies of elementary steps on Ni_1 step are lower than those on Ru_1 site as shown in **Table 5.2**, indicating that Ni_1 site is more active in the transformation from CH_4 to CO. Thus, DFT calculations suggest that Ni_1 is responsible for the activation of CH_4 to form CO. In the potential pathways presented in **Table 5.2**, the highest free energy barriers among these elementary steps are the activation of the first C-H of methane on both Ni_1 and Ru_1 sites. It suggests that methane activation is the rate-determining step of reforming CH_4 with CO_2 on $Ru_{0.025}Ni_{0.025}Ce_{0.95}O_2$.

Table 5.2. Free energy barriers (G_a) and free energy changes (ΔG) for the elementary steps in CH_4 dehydrogenation and oxidation on Ni_1 and Ru_1.

	Ni_1			Ru_1		
step	Reaction	G_a	ΔG	Reaction	G_a	ΔG
1	$CH_4(g)+2*\leftrightarrow CH_3*+H*$	1.88	0.94	$CH_4(g)+2*\leftrightarrow CH_3*+H*$	2.01	0.82
2	$CH_3*+O*\leftrightarrow CH_3O*+*$	1.33	-0.03	$CH_3*+*\leftrightarrow CH_2*+H*$	1.73	0.69
3	$CH_3O*+*\leftrightarrow CH_2O*+H*$	1.52	1.04	$CH_2*+O*\leftrightarrow CH_2O*+*$	1.30	-0.34
4	$CH_2O*+*\leftrightarrow CHO*+H*$	0.01	-0.03	$CH_2O*+*\leftrightarrow CHO*+H*$	0.48	-0.28

5	CHO*+*↔CO*+H*	0.17	-0.20	CHO*+*↔CO*+H*	0.00	-0.44
6	CO*↔CO(g)+*		0.64	CO*↔CO(g)+*		1.70

5.4.4 Activation of CO_2 to form CO and O on Ru_1+O_{vac}

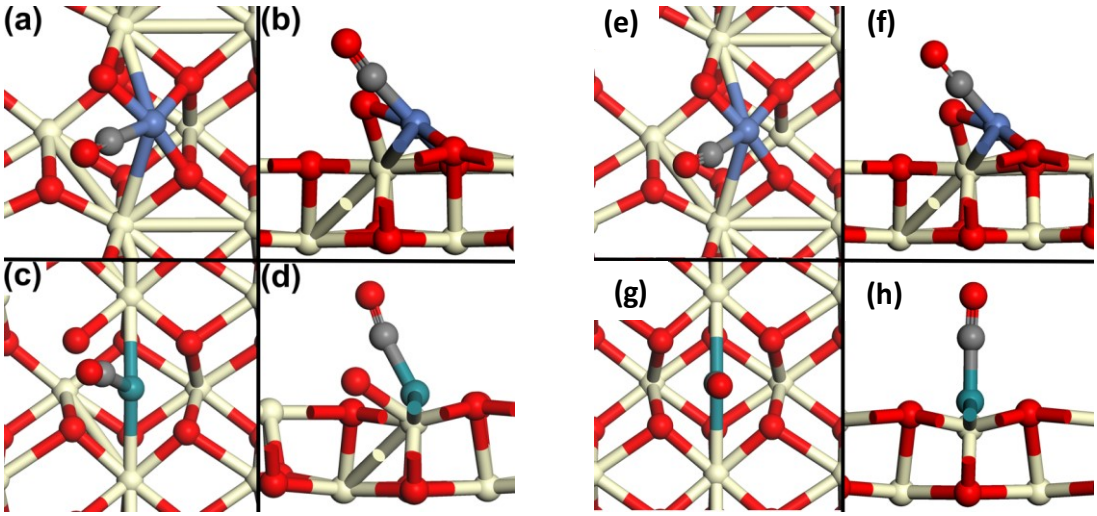

Figure 5.12. Top views and side views of transition state geometries of CO_2 dissociation and the final state geometries on Ni_1 and Ru_1 sites on CeO_2. (a and b) Top and side views of transition state geometries of CO_2 dissociation on Ni_1 site. (c and d) Top and side views of transition state geometries of CO_2 dissociation on Ru_1 site. (e and f) Top and side views of final state of CO_2 dissociation on Ni_1 site. (g and h) Top and side views of final state of CO_2 dissociation on Ru_1 site.

After desorption of CO from the catalyst, a lattice oxygen atom is removed from the surface of CeO_2 and thus an oxygen vacancy is created. The oxygen vacancy needs to be filled so that the surface of CeO_2 continuously provide surface lattice oxygen atoms for oxidation steps of the next catalytic cycle since the transition state is a four-membered ring-like structure involving the

bindings of C and H atoms of CH_4 to Ni and O atoms, respectively. In dry reforming ($CH_4+CO_2=2\ CO + 2\ H_2$), carbon dioxide is the only source to provide oxygen atoms to fill oxygen vacancies of the catalyst surface. Here activations of CO_2 on Ni_1 and Ru_1 sites together with formation and refilling of oxygen vacancies were investigated. It is found that the dissociation free energy barriers (*Ga*) of CO_2 on Ni_1 and

Ru_1 are 1.23 eV and 0.01 eV, respectively. Thus, activation of CO_2 on Ru_1+O_{vac} is much more active than Ni_1+O_{vac}. As shown in Figures **5.12a** and **5.12b**, the activation of CO_2 on Ni_1 and Ru_1 involves oxygen vacancies next to Ni_1 and Ru_1 atoms, respectively. After crossing this transition state (**Figures 5.12a-b**), the formed CO binds to Ni_1 and the formed O to fill O_{vac} next to Ni_1. In addition, it is possible to activate CO_2 to form CO to be adsorbed on Ru_1 and form O to fill to O_{vac} next to Ru_1 (**Figures 5.12c** and **5.12d**). Free energy changes in dissociation of CO_2 on Ni_1+O_{vac} and Ru_1+O_{vac} to form the adsorbed CO and O are 0.76 eV nd -0.99 eV, respectively. Obviously, Ru_1+O_{vac} is favorable for activation of CO_2 in contrast to Ni_1+O_{vac}.

5.4.5 Coupling of H atoms to form H_2 on Ru_1

The activations of CH_4 and CO_2 to form two CO molecules eventually. Other than formation of CO through activation of CH_4 to CH_n (n=0-3) along with progressive oxidation of CH_n (n=0-3) to CO, H atoms are formed in the pathway of transferring CH_4 to CO as shown in **Table 5.2**. Coupling of formed H atoms on surface to form hydrogen molecules is a necessary step. Here it was investigated. Transition states for coupling hydrogen atoms on Ni_1 and Ru_1 sites are shown in **Figure 5.13**. The calculated activation barriers for coupling hydrogen atoms on Ni_1 and Ru_1 sites are 1.96 eV and 0.65 eV, respectively, while the free energies changes for coupling hydrogen

atoms to form a H_2 molecule on Ni_1 and Ru_1 sites are 0.63 eV and 0.26 eV, respectively. Therefore, Ru_1 site should be responsible for coupling atomic hydrogen to form a H_2 molecule.

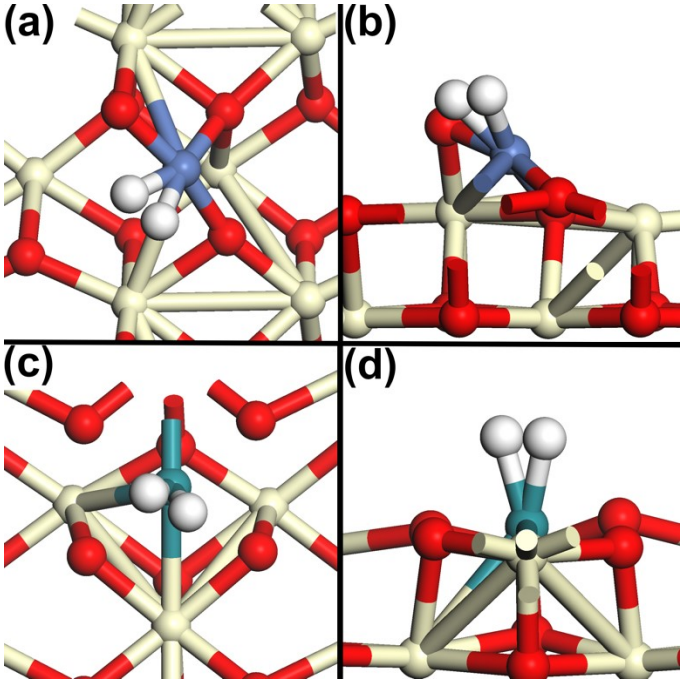

Figure 5.13. Top views and side views of transition state geometries of hydrogen coupling on Ni1 site (a and b) and on Ru_1 site (c and d).

5.4.6 Synergy effect of Ni_1 and Ru_1 in reforming CH_4 with CO_2

The chemical and coordination environments of Ni atoms and Ru atoms of optimized $CeO_2(110)$ with anchored Ni_1 and Ru_1 atoms proposed through DFT calculations well agree with the experiment results, suggesting that our models optimized with DFT are suitable to study the reforming mechanism of CH_4 with CO_2. The activations of methane and CO_2 and coupling of atomic hydrogen were simulated with all the possible elementary steps on Ni_1, Ru_1, Ni_1+Vac, and Ru_1+Vac. It is found that Ni_1 and its adjacent oxygen atom are highly active for the activation of

methane to form CO and oxygen vacancy with a low activation barrier, offering high activity of reforming methane on $Ru_{0.025}Ni_{0.025}Ce_{0.95}O_2$ at low temperature. Ru_1+O_{vac} responsible for activation of CO_2 to form CO and O. The different roles of Ni_1 site (for activation of CH_4) and Ru_1 site (for activation of CO_2) of $Ru_{0.025}Ni_{0.025}Ce_{0.95}O_2$ clearly justified the synergy effect of the dual single-atom sites (Ni_1 and Ru_1) observed experimentally.

As discussed above, the formed hydrogen atoms in the steps of activating CH_4 to form CO on Ni_1 site prefer to couple to form hydrogen molecules on Ru_1 site. In other words, the first formation of atomic hydrogen on Ni_1 site and then coupling H atoms to form H_2 on Ru_1 site is format of synergy role of Ni_1 and Ru_1 sites of $Ru_{0.025}Ni_{0.025}Ce_{0.95}O_2$; in other words, Ni_1 and Ru_1 plays a sequential role in first generation of H atoms on Ni_1 sites and then coupling of H atoms to form H_2 on Ru_1 site in a catalytic cycle. Thus, the DFT calculations provided a molecular picture of synergy effect of two sets of single-atom sites (Ni_1 and Ru_1) on $Ru_{0.025}Ni_{0.025}Ce_{0.95}O_2$.

5.5 Summary

Ru and Ni cations were successfully anchored on the surface of ceria oxide nanorods. It was characterized and tested for methane dry reforming. It was found be an active catalyst for methane dry reforming with CO_2. The synergistic effect between Ru an Ni contributes to decrease the activation energy of the reaction, which was confirmed by the catalytic performance of methane reforming and kinetic analysis. The reaction mechanism was studied by in-situ spectroscopy and DFT calculations. The origination of the synergistic effect is Ni sites are found to be highly active for the activation of methane and formation of oxygen vacancy, while Ru sites are highly active for the hydrogen coupling and CO_2 activation.

Chapter 6 Transition of surface phase of cobalt oxide during CO oxidation

6.1 Introduction

CO oxidation is a probe reaction frequently used in testing catalytic activity in designing new catalytic materials. In these efforts, the correlation between a structural parameter of a series of catalytic materials and their catalytic activities was explored. For instance, CO oxidation on metal nanoparticles with variable sizes or shapes of monometallic nanoparticles or tunable compositions of bimetallic nanoparticles with same size and shape were extensively in the last two decades.[95, 179-180] Most precious metals exhibit high activity for CO oxidation at room temperature or higher.[181-186] From an application point of view, it is probably not realistic to use precious metal-based catalysts at an industrial scale for CO oxidation due to the extremely low abundance of precious metals in the Earth. There are continuous efforts in searching catalysts made of earth-abundant elements for CO oxidation.

The abundances of early transition metals in the Earth are much higher than that of precious metals by several orders of magnitude. Early transition metal oxide-based catalysts are potential catalysts for CO oxidation to be used at an industrial scale.[187-188] Co_3O_4 nanorods with preferentially exposed (110) have been reported to be very active for CO oxidation.[188-190] Co_3O_4 nanorods with diameter of 5-10 nm can catalyze CO oxidation at a temperature as low as -77 ºC.[189] The exceptional catalytic activity of Co_3O_4 nanorods for low-temperature CO oxidation was proposed to be attributed to the predominantly exposed planes, Co_3O_4 (110)[191], which are enriched with Co^{3+} species.[192-193] Furthermore, high activity of surface lattice oxygen and oxygen vacancies on Co_3O_4 were expected to assist the activation of molecular oxygen and thus enhance its activity.[190] To explore the shape-dependent catalysis including CO oxidation on Co_3O_4, many efforts were made in synthesis of Co_3O_4 nanocatalysts with different morphologies through wet

chemistry methods. Various nanostructured Co_3O_4 such as nanoflowers, nanocubes, nanobelts, nanospheres, nanowires, and mesoporous Co_3O_4 were synthesized and CO oxidation was tested on these Co_3O_4 catalysts.[194-202] However, so far the catalytic mechanism of CO oxidation on Co_3O_4 at a molecular level is still not clear. DFT calculations suggested the high catalytic activity of Co_3O_4 results from high activity of surface lattice oxygen in terms of low activation barriers for creating and hopping oxygen vacancies on the surface of Co_3O_4.[190, 203-209] Alternatively, molecular oxygen was proposed to be activated into oxygen superoxide ion (O_2^-) by surface oxygen vacancies, which actively couples with CO molecule adsorbed on cobalt cations of Co_3O_4 to form product CO_2.[210]

Different from Co_3O_4, CoO is another phase of cobalt oxides. It can be generated through reduction of Co_3O_4 with CO or H_2 at a relatively low temperature since Co-O bond is one of the weakest M-O bonds (M=metal) among all transition metal oxides.[211] CoO can also be generated through a thermal-driven phase transition.[211] Recently, the as-synthesized Co_3O_4 was reported as an active phase for reduction of NO with CO.[212] In-situ/operando studies of Co_3O_4 during reduction of NO with CO with AP-XPS uncovered that the active phase at a relatively high temperature is in fact nonstoichiometric CoO_{1-x} instead of Co_3O_4; the formation of cobalt monoxide phase during catalysis was confirmed with TEM studies including diffraction pattern and energy loss spectroscopy;[212] in this reaction Co_3O_4 was progressively reduced to nonstoichiometric CoO_{1-x} in the temperature range of 100-300ºC. The nonstoichiometric CoO_{1-x} is the active phase for reduction of NO with CO at 400ºC;

There is lack of knowledge of whether CoO is active for CO oxidation and how stable CoO surface phase could be although it is highly active for reduction of NO with CO.[212] Here we chose the surface phase CoO as a catalyst to examine its activity for CO oxidation and track any potential

transition of the CoO surface phase during CO oxidation along with the increase of catalysis temperature. We found that CoO surface phase is quite active for CO oxidation in the temperature range of 60-120ºC. In situ/operando studies using AP-XPS suggest that surface phase CoO can progressively restructure to Co_3O_4 surface phase during CO oxidation at a catalysis temperature >140ºC. The newly formed active surface phase Co_3O_4 (formed from CoO in the temperature range of 140-180ºC) exhibits activity for CO oxidation higher than CoO, evidenced by its low activation barrier. The transition of the surface phase of CoO to Co_3O_4 during catalysis along the increase of temperature was supported by TEM studies. The observed transition of the surface phase CoO to Co_3O_4 during CO oxidation suggests that (1) tracking surface phase of transition metal oxide during catalysis at different temperatures is necessary because restructuring of a transition metal oxide could be readily triggered at a relatively low temperature and (2) surface sensitive ambient pressure X-ray photoelectron spectroscopy working in gas phase can track potential evolution of surface phase along the increase of catalysis temperature.

6.2 Experimental section

6.2.1. Synthesis of Co_3O_4 nanoparticles

Co_3O_4 nanoparticles were prepared by ethylene glycol-assisted precipitation of cobalt hydroxide carbonate followed by thermal treatment.[192, 213] In a typical synthesis, 1 mmol of cobalt acetate tetrahydrate ($Co(CH_3COO)_2 \bullet 4H_2O$, Sigma-Aldrich, 98+%) was dissolved in 30 mL ethylene glycol ($C_2H_6O_2$, Fisher Chemical, certified), followed by heating to 160ºC. Then, 100 mL 0.2 M sodium carbonate (Na_2CO_3, Sigma-Aldrich, 99+%) aqueous solution was added to the above mixture of cobalt acetate and ethylene glycol. The resulted slurry was further heated at 160 ºC for

1 h. The solid sample was collected by filtration and washing with deionized water, followed by drying at 70 ^{o}C overnight. Finally, the sample was calcined at 350 ^{o}C for 3 hrs in static air, forming crystallized Co_3O_4 nanoparticles.

6.2.2. Characterization with ex situ and in situ techniques

Images of the representative size, shape and lattice fringes of the prepared Co_3O_4 nanoparticles were collected using a transmission electron microscopy (TEM, Hitachi H9500, Hitachi High Technologies, Inc.). The microscope was operated with a LaB_6 electron source in bright field (BF), high-resolution (HR), and diffraction TEM experiments. Selected area electron diffraction (SAED) patterns were acquired using the smallest selective area aperture (#3) for the area encompassing the field of view in the TEM image. Identification of the spots and rings in the SAED and fast Fourier transform (FFT) of the HRTEM images were analyzed using Digital Micrograph Software v3.10.1002.0 (Gatan, Inc.). Measurements were made to determine the distance in reciprocal space from the center spot to specific spots or rings. These measurements in (nm^{-1}) were then compared with reference d-spacing values for planes of known Co_3O_4 or/and CoO deposited in the Materials Project database.[214]

Transition of surface phase of cobalt oxides was characterized by a lab-based ambient pressure X-ray photoelectron spectrometer system (AP-XPS) built by Tao group. A part of the instrumentation of the second AP-XPS is the design of a new reaction cell which can allow to safely anneal catalyst to a temperature higher than 850^{o}C in gas phase.[215-216] Typically, Co_3O_4 nanoparticles were loaded into the reaction cell which has a gas inlet and outlet continuously introducing and purging a gas or a mixture of all gases of a catalytic reaction. Before analysis, the

Co_3O_4 nanoparticles were firstly reduced with 1 mbar H_2 (Praxair, 99.99%) at 250ºC for 2 hrs to form surface CoO phase. After reduction, the sample was cooled down to room temperature and then the H_2 was purged at 25ºC. The successful formation of CoO surface phase was confirmed by examining the Co 2p photoemission feature. After that, a mixture of 0.4 mbar CO (Praxair, 99.99%) and 1 mbar O_2 (Praxair, 99.99%) flew into the reaction cell, followed by heating the sample from room temperature up to 220ºC. XPS spectra of Co 2p and O 1s were collected at 60, 100, 140, 180, and 220ºC. The gas near to the catalyst was directly sampled to another UHV chamber where a mass spectrometer was installed for analysis of gas composition.

6.2.3. Measurement of catalytic performance of CO oxidation

Catalytic activity and kinetics studies were done in a fixed-bed flow reactor. In a typical test of catalytic activity of the catalyst, Co_3O_4 nanoparticles was loaded into a quartz tube reactor and supported by quartz wool. A K-type thermocouple was used to measure temperature of catalyst bed. Before reaction, the catalyst was pretreated at 250 ºC in 50 mL/min 5%H_2/95%Ar (Praxair) for 2 h. After that, the reactor was cooled to room temperature in 5% H_2, followed by switching the gas to the mixture of 20 mL/min 5%CO/95%Ar (Praxair) and 50 mL/min 5%O_2/95%Ar (Praxair). The reactor was heated stepwise from room temperature to 240ºC at an interval of 20ºC. At each temperature, the gas composition was measured by an online gas chromatography.

For kinetic study, Co_3O_4 nanoparticles were mixed with 100 mg quartz and packed into the reactor. The catalyst was reduced at 250ºC for 2 hrs in 50 mL/min 5%H_2/95%Ar (Praxair), followed by cooling to room temperature. The activation energy was calculated by measuring the CO conversion on CoO in the temperature range of 80 to 120 ºC in a mixture of 20 ml 5% CO and

50 ml 5% O_2 with a molar ratio of 1:2.5. To measure the activation energy on Co_3O_4 in the temperature range of 60 to 200°C, the flow rate of CO and O_2 was increased since the reaction rate of CO oxidation at 160-200°C is much higher than that at 80-120°C, by which the conversion CO in the temperature of 160-200°C is lower than 15%.

Determination of activation energy barrier: for a typical reaction $A + B \rightarrow 2C$, the general rate equation could be expressed as Eq.1, or in the logarithm form of Eq.2. Assume the reaction is in the kinetics control regime (e.g., conversion <20%), equation could be simplified to Eq.3. Given $rate(CO) = Conversion * molar\ flow\ rate$, eventually we can get *Eq.4*. The conversion of CO could be plotted as the function of (1000/T) to evaluate the activation energy barrier as shown in **Figure 6.6**

$$rate = A * \exp(-\frac{Ea}{RT})[A]^m[B]^n \qquad (Eq.\ 1)$$

$$\ln(rate) = lnA + \left(-\frac{Ea}{RT}\right) + m * \ln[A] + n * \ln[B] \qquad (Eq.2)$$

$$\ln(rate) = \left(-\frac{Ea}{RT}\right) + Constant \qquad (Eq.3)$$

$$\ln(Conversion) = \left(-\frac{Ea}{RT}\right) + Constant \qquad (Eq.4)$$

6.3 Results and discussion

6.3.1 Evolution of surface chemistry of Co_3O_4 nanoparticles during catalysis

Surface chemistry of cobalt oxide nanoparticles in the presence of reactants (i.e., CO and O_2) at 60-220 °C was tracked with AP-XPS. Before the analysis, the surface of Co_3O_4 nanoparticles was reduced at 250 °C in 5%H_2/95%Ar for 2 h to form the surface phase CoO. It is noted that Co_3O_4

and CoO can be identified and distinguished with valence spectra collected with ultraviolet photoelectron spectroscopy or high-resolution synchrotron photoelectron spectroscopy. Here X-ray photoelectron spectroscopy was used to identify and distinguish Co_3O_4 and CoO. The formation of surface phase CoO was confirmed by a close examination of photoemission features of Co $2p_{3/2}$. It is reported that CoO and Co_3O_4 can be distinguished by the characteristic satellite peak of Co^{2+} in octahedral coordination with 6 oxygen atoms in CoO. [217-219] [220-223]The observed main peak of Co $2p_{3/2}$ at 780.7 eV and its satellite peaks at 786.7 eV in Figure 6.1a1 suggests that the surface phase of the catalyst at room temperature is cobalt monoxide. The satellite peak of Co $2p_{3/2}$ at 786.7 eV was contributed from a specific type of Co^{2+} cations coordinating with six oxygen atoms in octahedral coordination which is only available in CoO but not Co_3O_4. Co^{2+} and Co^{3+} are in tetrahedral and octahedral coordination shells with four and six oxygen atoms, respectively in spinel Co_3O_4. As Co_3O_4 does not have Co^{2+} in an octahedral coordination with six oxygen atoms, photoemission feature of Co $2p_{3/2}$ of Co_3O_4 does not have any satellite peak at 786.7 eV.

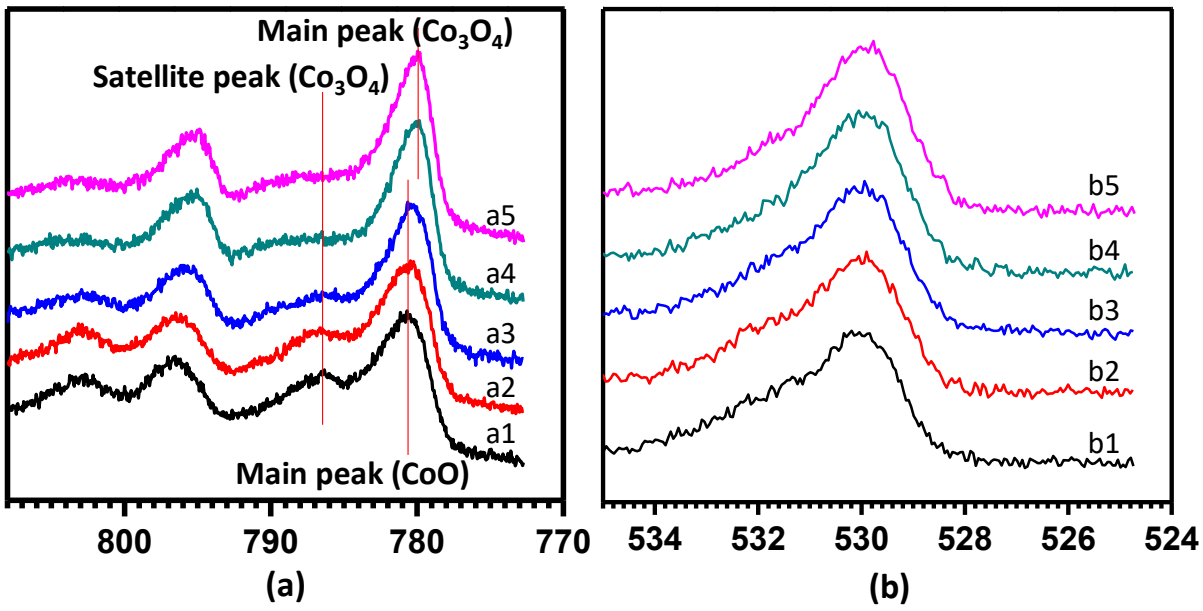

Figure 6.1. Evolution of photoemission feature of (a) Co 2p and (b) O 1s of CoO surface phase during CO oxidation in 0.4 Torr CO and 1.0 Torr O_2 in the temperature range of 60-220 ^oC. (a1, b1) 60 ^oC, (a2, b2) 100 ^oC, (a3, b3) 140 ^oC, (a4, b4) 180 ^oC, and (a5, b5) 220 ^oC.

The clear observation of a peak at 786.7 eV in Figure 6.1a1 marked with a red line confirmed the formation of CoO surface phase. As discussed in the next section, TEM studies of the phases of the cobalt oxide nanoparticles (after the reduction in 5% H_2 at 250^oC) shows that the core of the Co_3O_4 nanoparticles is still Co_3O_4 phase although its surface phase is CoO. Here the term, Co_3O_4@CoO is used to represent the structure of the catalyst nanoparticle. Thus, the formed Co_3O_4@CoO nanoparticle catalyst was used as a model catalyst to explore any potential phase transition of transition metal oxide-based catalysts during catalysis.

A mixture of 0.4 mbar CO and 1 mbar O_2 was introduced to flow through Co_3O_4@CoO in the reaction cell of AP-XPS; then the CoO in the mixture of CO and O_2 was heated to 60 ^oC, 100^oC, 140^oC, 180^oC, and 220^oC. Photoemission features of Co 2p and O 1s of the catalyst in this temperature range in the mixture of CO and O_2 were collected at each temperature. In the temperature range of 60-140 ^oC, the satellite peaks at 786.7 eV and main peak at 780.7 eV of Co $2p_{3/2}$ of Co^{2+} remained, suggesting that the surface CoO phase is stable in the mixture of CO and O_2 in this temperature range. The relative intensity of the satellite peak of Co $2p_{3/2}$ at 786.7 eV in contrast to the main peak at 780.7 eV is progressively decreased along the increase of temperature from 60^oC to 140^oC. In fact. the intensity of the satellite peak of Co $2p_{3/2}$ disappeared at a temperature higher than 140^oC (Figure 6.1a3). As interpreted in literature[217-219 220-223]these satellite peaks are associated with Co^{2+} ions at octahedral coordination with oxygen atoms in CoO. Thus, the disappearance of the satellite peak suggests that the surface CoO was oxidized to Co_3O_4 at 140^oC in the mixture of CO and O_2. In addition, upon increasing the temperature to 180^oC or 220^oC,

the main peak of Co $2p_{3/2}$ at 780.7 eV observed at 60-140ºC (Figures 1a1-1a3) down shifted to 780.0 eV at 180ºC and 220ºC (Figures 1a4 and 1a5). The disappearance of the satellite peak of Co $2p_{3/2}$ of CoO at 786.7 eV and the observed down-shift of the main peak of Co $2p_{3/2}$ suggest that the surface phase of the catalyst Co_3O_4@CoO nanoparticles has been transited to another when the catalysis temperature is higher than 140ºC. The observed binding energies of the main peak of Co $2p_{3/2}$ at 780.0 eV and the lack of a satellite peak at 786.7 eV are consistent with photoemission feature of Co_3O_4 reported in the literature.[212-213, 217-223] Thus, the surface phase CoO transformed to Co_3O_4 surface phase at 140ºC. Obviously, tracking the evolution of Co $2p_{3/2}$ photoemission feature during catalysis along the increase of temperature with AP-XPS allows us find out potential phase transition of oxide during catalysis. It is understandable that other techniques such as valence band spectroscopy including ultraviolet photoelectron spectroscopy or high resolution synchrotron photoelectron spectroscopy could be used to distinguish the Co_3O_4 and CoO [224-228]. In this work, we have mainly used photoemission feature of sub-shell (Co 2p) electrons to distinguish Co_3O_4 and CoO since AP-XPS is the daily available technique in our group. The difference between photoemission features of Co 2p of Co_3O_4 and CoO was reported in literature.[229-242] As mentioned above, the characteristic feature of Co 2p photoemission feature of CoO is the satellite peak at 786.8 eV contributed from Co^{2+} in the octahedral coordination. As Co^{2+} in Co_3O_4 is in tetrahedral coordination, it does not give such a satellite peak. In addition, the main peak of Co2p of CoO is lower than that of Co_3O_4 by 0.9 eV or so. Similar to literatures, [201, 243-246] we have used these characteristic features to distinguish CoO from Co_3O_4 in several of our recent works. [201, 243-246]

Based on the observation of AP-XPS during catalysis, a schematic (Figure 6.2) was proposed to represent the transition of surface phase under these conditions. The surface of Co_3O_4 nanoparticles (Figure 6.2a) was reduced to CoO during reduction in H_2 at 250ºC, forming a

Co_3O_4@CoO structure (Figure 6.2b). The Co_3O_4@CoO core-shell structure is stable during CO oxidation in the temperature range of 60-140°C (Figure 6.2c). At a temperature above 140 °C, the CoO surface phase during catalysis was oxidized to Co_3O_4 (Figure 6.2d). Notably, based on the following TEM studies, the core of these nanoparticles in these evolutions remained the original Co_3O_4 phase (Figure 6.2).

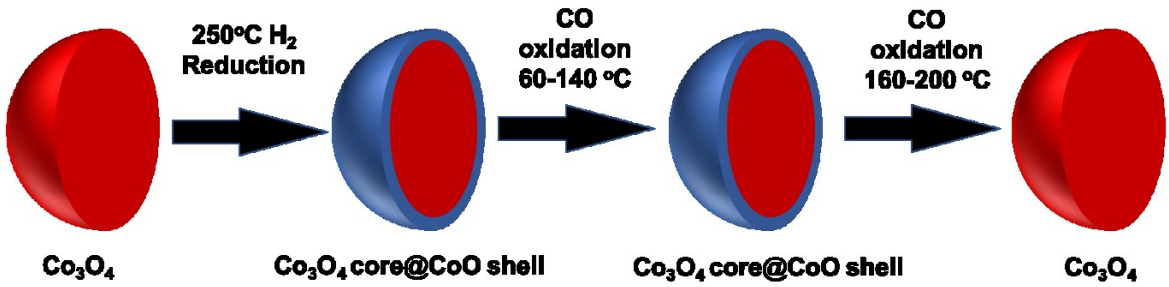

Figure 6.2. Schematics showing the evolution of as-synthesized Co_3O_4 nanoparticles (a), reduced at 250 °C in 5%H_2/Ar for 2 hrs (b), and then used for CO oxidation in the temperature range of 60-140°C (c), followed by CO oxidation in the temperature range of 160-200°C (d).

6.3.2 TEM studies of catalyst structure formed at ≤140°C

The morphology and structure of Co_3O_4@CoO catalyst after CO oxidation at 140 °C were further analyzed by TEM since AP-XPS only provides information on the surface region of Co_3O_4@CoO nanoparticles. Before reduction of Co_3O_4 with 5% H_2 at 250°C for preparing CoO surface phase, the electron diffraction of these catalyst nanoparticles in Figure 6.3b confirmed that the catalyst nanoparticles before reduction in 5% H_2 at 250°C were pure Co_3O_4 phase. Figure 6.3b is a representative diffraction pattern among many selected areas of the TEM sample. All these studies show Co_3O_4 phase instead of CoO. Figure 6.3c is the TEM image of the as-synthesized

Co_3O_4 experienced reduction in 5% H_2 at 250ºC and then catalysis of CO oxidation at 140ºC in the mixture of CO and O_2. Figure 6.3d is the corresponding diffraction pattern of Figure 6.3c. (220) and (100) plane of CoO and (311), (220) and (100) plane of Co_3O_4 were observed in the diffraction pattern. The coexistence of Co_3O_4 and CoO was observed in diffraction patterns of other areas of the same catalyst sample. These studies suggest the core of the catalyst nanoparticles after catalysis at 140ºC remain its Co_3O_4 phase though surface phase is CoO. Thus, both Co_3O_4 and CoO coexist in the catalyst nanoparticles after reduction in 5% H_2 at 250ºC and then catalysis for CO oxidation at 140ºC.

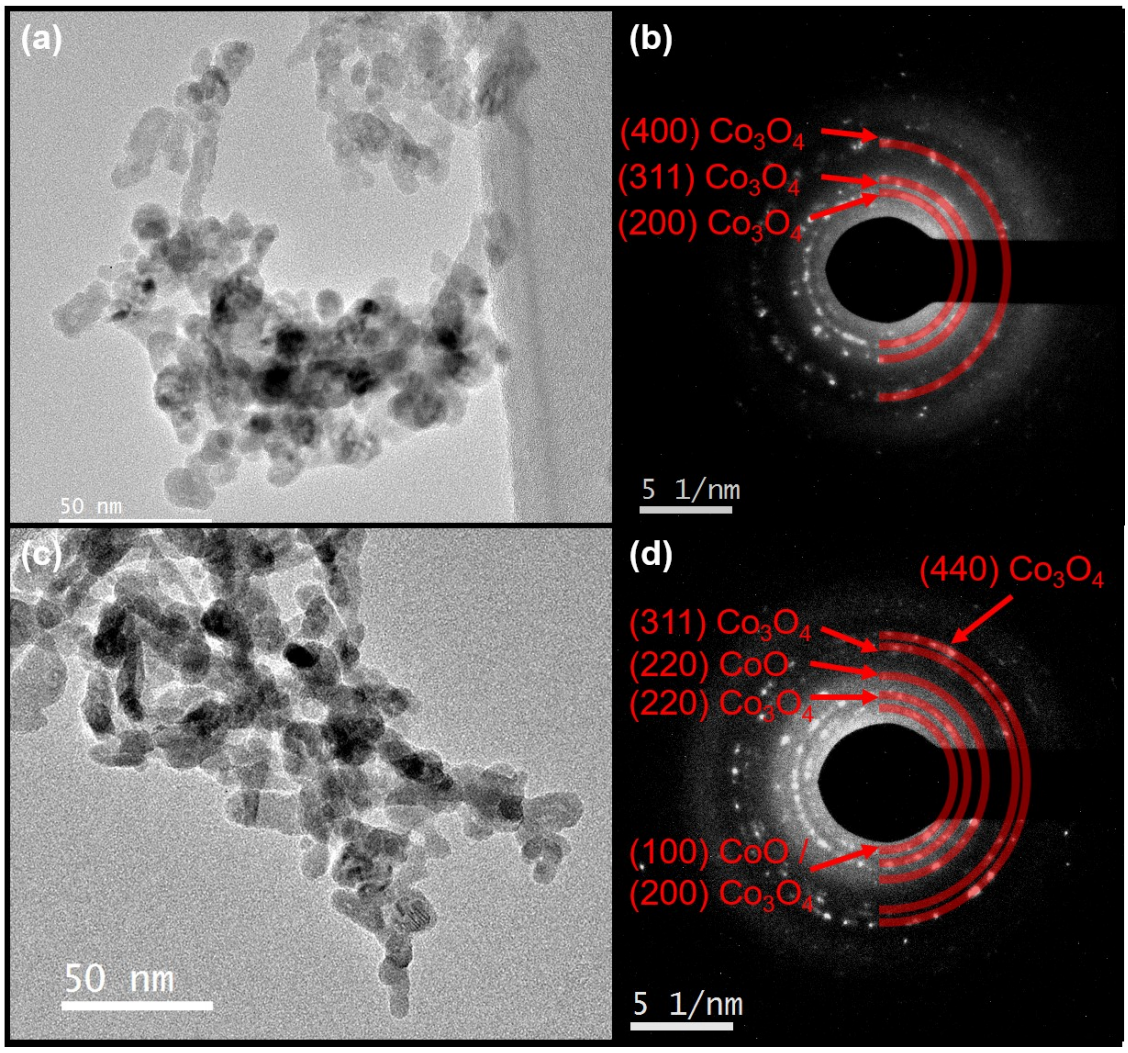

Figure 6.3. TEM studies of Co_3O_4 before and after a treatment including both a reduction in 50 mL/min of 5%H_2/Ar at 250 °C for 2 hrs to form a CoO surface phase and then CO oxidation on the formed CoO in the mixture of 20 mL/min of 5%CO/Ar and 50 mL/min of 5%O_2/Ar at 140 °C. (a) and (b) BFTEM image and SAED pattern of Co_3O_4 before reduction in 5% H_2 at 250ºC. (c) and (d) BFTEM image and SAED pattern of cobalt oxide which experienced two steps: reduction of Co_3O_4 at 250ºC in 5% H_2 for forming CoO surface phase and then catalysis of CO oxidation at 140ºC on the CoO.

The observation of both Co_3O_4 and CoO phases in Figure 6.3d could be contributed from mixture of pure Co_3O_4 and pure CoO nanoparticles, instead of the formation of Co_3O_4 core@CoO shell structure since the diffraction pattern is not contributed from only one nanoparticle. To elucidate whether nanoparticles of Co_3O_4 core@CoO shell were formed or not, we performed further analysis of TEM images and SEAD patterns of cobalt oxide nanoparticles, which experienced both reduction in 5% H_2 at 250ºC and then CO oxidation at 140ºC. Specific deconvolution of the HRTEM image of Figure 6.4a allowed for the mapping of observable lattice fringes to show the location of the CoO nanoparticles from that of Co_3O_4 nanoparticles in the collected HRTEM micrographs. The locations of lattice fringes for these two cobalt oxide phases (Co_3O_4 and CoO) were visualized using FFT filtering and/or masking techniques available in Digital Micrograph software package. First, a bandpass was applied to remove all reciprocal spaces in the FFT of the HRTEM image that were of radii larger than the clearest identifiable spots, this approach reduces noise in the image. The FFT was then further masked by using a bandpass annulus to remove specific radii or rings that correspond to either phase (Co_3O_4 and CoO), thereby, by which the overlapping lattice fringes of Co_3O_4 and CoO were separated. New images were generated from these masked FFTs using an inverse FFT (iFFT) function. The resulting maps suggest the localization from the observable lattice fringes.

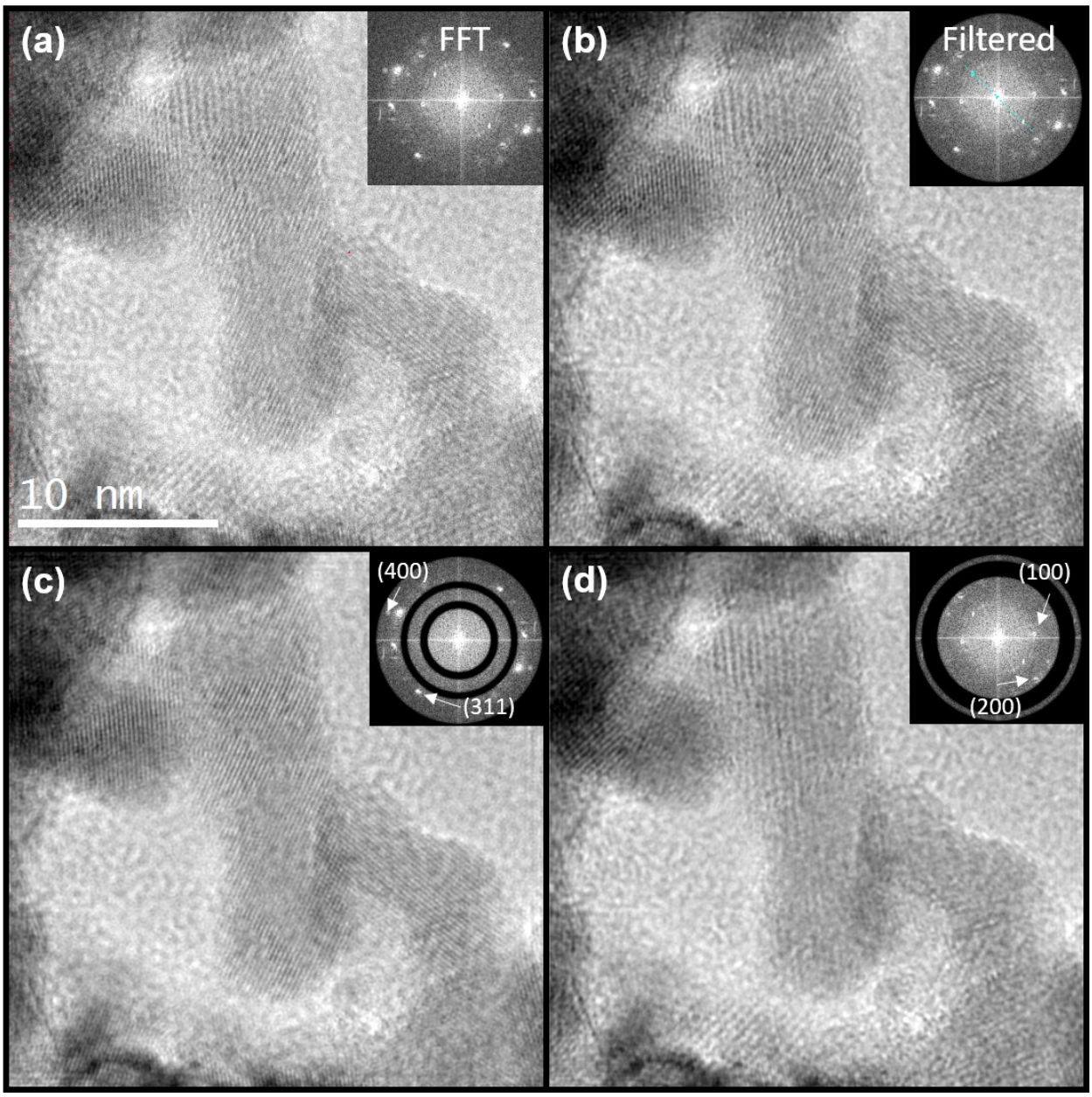

Figure 6.4. Coexistence of surface phase CoO and bulk phase Co_3O_4 in catalyst nanoparticles (formed from two steps: reduction of Co_3O_4 nanoparticles in 5% H_2 at 250ºC for two hours and then CO oxidation at 140ºC) during CO oxidation with 20 mL/min of 5%CO/Ar and 50 mL/min of 5%O_2/Ar at 140 ºC. (a) The unprocessed HRTEM image and corresponding FFT (a inset) of catalyst nanoparticles. (b) The bandpass filtered FFT (inset) and iFFT of image of catalyst nanoparticle in (a). (c) iFFT image of the FFT (c inset) that has been masked to remove the (200) planes of CoO to remain only the fringes of Co_3O_4 phase. (d) iFFT image of the FFT (inset) in which (400) of Co_3O_4 planes were masked to remain only fringes of CoO.

Figure 6.4c is the iFFT image which was obtained by masking all planes of CoO so that only fringes of Co_3O_4 were shown. The existence of Co_3O_4 phase was supported by the iFFT map in Figure 6.4c where the lattice fringe in terms of inter-planar distance, 0.202 nm is attributed to (400) planes of Co_3O_4. In Figure 6.4d, all panes of Co_3O_4 were masked. On the same nanoparticle, the existence of CoO phase was supported by the observation of lattice fringe of CoO in Figure 6.4d, where the measured lattice spacings of the 0.227 nm were attributed to (200) planes of CoO phase. Thus, these TEM images and the corresponding diffraction patterns show that the coexistence of Co_3O_4 and CoO phases in the same cobalt oxide nanoparticles. As the original phase before reduction was pure Co_3O_4, the coexistence of Co_3O_4 and CoO on the same nanoparticle suggests that the surface phase is the reduced phase (CoO) and the core is its original phase (Co_3O_4). Thus, through these deep analyses we concluded that the surface region of these nanoparticles is CoO and their bulk is Co_3O_4. In other words, surface phase CoO and bulk phase Co_3O_4 coexist in the same catalyst nanoparticle as schematically shown in Figures 2b and 2c.

6.3.3 Catalytic performance and kinetics studies at ≤ 140°C

Catalytic performance of CO oxidation was studied with mass spectrometry and gas chromatography. In the mass spectrometry, partial pressures of CO (reactant) and CO_2 (product) were monitored as a function of catalysis temperature as shown in Figure 6.5. The product of CO oxidation, CO_2 formed on CoO surface phase was measured through an on-line mass spectrometer which takes a small amount of gas from cell to mass spectrometer when the sample during catalysis was being characterized with AP-XPS. Figure 6.5 presents the partial pressures of CO (black line) and CO_2 (green line) of the sampled gas from the reaction cell of AP-XPS. Notably, the partial pressures of CO and CO_2 reported in Figure 6.5 are definitely not the in-situ partial pressures in

the reaction cell because only a significantly small portion of gases in the reaction cell was introduced to the UHV chamber installed with the mass spectrometer.

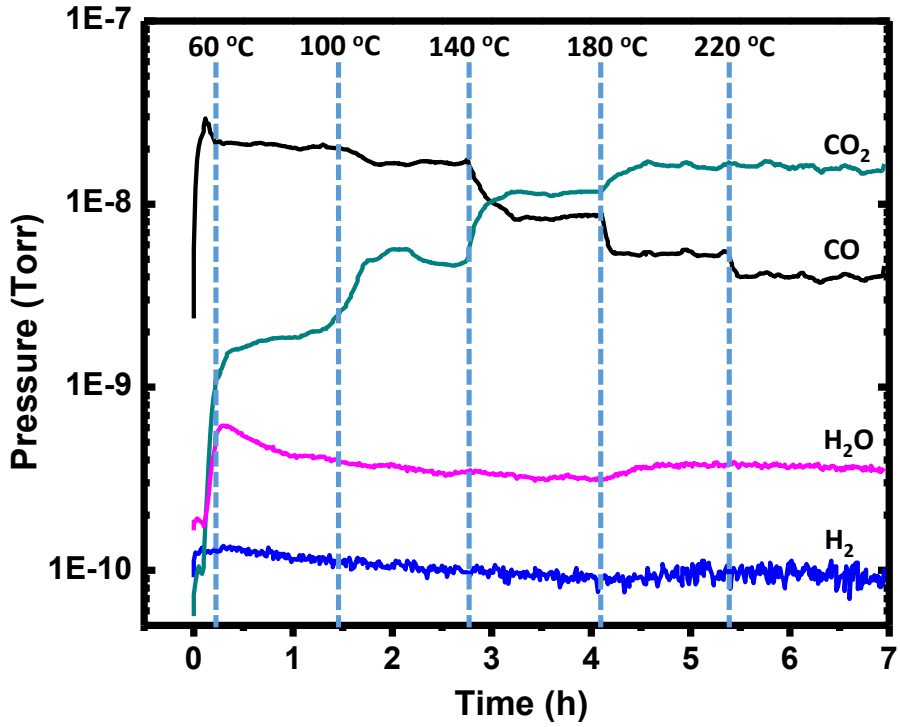

Figure 6.5. Evolution of reactant CO and products CO_2 during CO oxidation (0.4 Torr CO + 1 Torr O_2) on CoO (formed by reduction of Co_3O_4 in 5% at 250ºC) in the temperature range of 60-220ºC when the surface of CoO was simultaneously monitored with AP-XPS. The partial pressures of CO and CO_2 were measured with on-line mass spectrometer. It is noted that these observed partial pressures in the UHV chamber of mass spectrometer are much lower than the actual pressure in the reaction cell since only a tiny amount of gas near to surface of catalysts in the reaction cell was sampled to another UHV chamber where the mass spectrometer was installed.

The evolution of partial pressures of CO and CO_2 and the surface chemistry of cobalt oxide catalyst were studied simultaneously. After increasing the reaction temperature from 60ºC to 100ºC, the partial pressure of CO dropped from ~2.06×10^{-8} to 1.67×10^{-8} Torr; correspondingly, the partial pressure of product CO_2 increases from ~ 1.86×10^{-9} to 5.67×10^{-9} Torr (Figure 6.5). Pressure of

impurities (i.e., H_2O and H_2) were tracked as a reference in Figure 6.5 since their partial pressures didn't obviously change during catalysis in the temperature range of 60-220ºC. The preservation of partial pressure of impurity gas such as H_2O shows that the increase of CO_2 pressure and decrease of CO pressure must result from the catalytic reaction instead of desorption of CO_2 molecules originally adsorbed on the wall of reaction cell or consumption of CO by some metal to form carbonyl, respectively. When increasing the reaction temperature from 100ºC to 140 ºC, the CO partial pressure further dropped from 1.67×10^{-8} to 8.17×10^{-9} Torr. Correspondingly, the CO_2 partial pressure increased from 4.54×10^{-9} to 1.17×10^{-8} Torr. The simultaneous decrease of CO pressure and increase of CO_2 pressure shows that this catalyst is active in the temperature range of 100-140ºC. As the simultaneous characterization of the catalyst surface with AP-XPS shows that surface during CO oxidation at 100-140ºC is CoO, we concluded that CoO is the active phase for CO oxidation in the temperature range of 100-140ºC.

6.3.4 Catalysis and surface phase in the temperature range of 180ºC-220ºC

When the catalysis temperature was increased from 180ºC to 220ºC, CO partial pressure further decreased and CO_2 partial pressure further increased correspondingly. Based on the AP-XPS studies in Figures 1a4 and 1a5, the active surface phases at 180ºC and 220ºC were actually Co_3O_4. Thus, the active surface phase CoO of catalyst Co_3O_4@CoO (up to 140ºC) was transformed to Co_3O_4 during catalysis at a temperature higher than 140ºC. Figures 2c and 2d schematically presents the change of surface phase from CoO to Co_3O_4. In other words, the active phase during CO oxidation at 180-220ºC is Co_3O_4 instead of CoO.

The catalytic performance of the prepared CoO surface phase was further examined by carrying out the CO oxidation reaction in a fixed-bed flow reactor at atmospheric pressure. On-line measurements of the concentration of CO and CO_2 of the downstream gas of the reactor were performed with the gas chromatograph connected to the fixed-bed flow reactor. Conversion of CO was measured with TCD detector of GC.

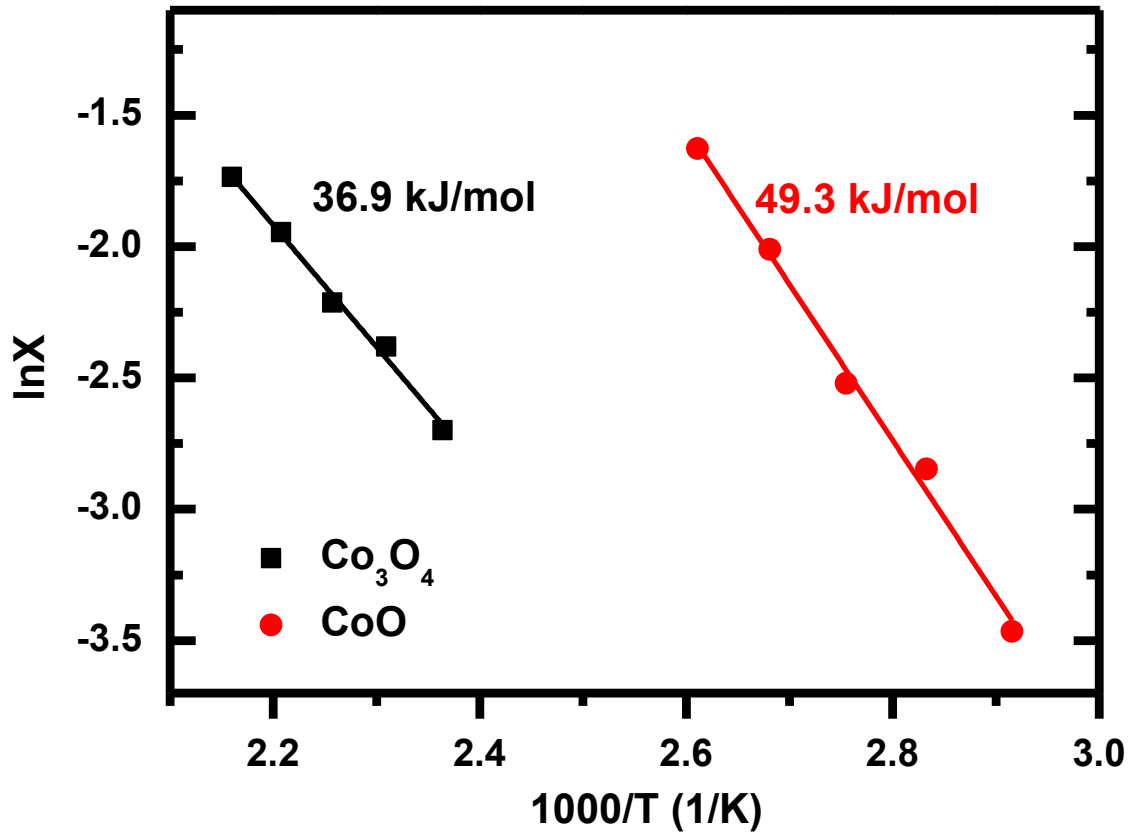

Figure 6.6. Arrhenius plots of CO oxidation over CoO (formed by reducing Co_3O_4 in 5% H_2 at 250°C) at 80-120 °C and Co_3O_4 formed from CoO during catalysis at 160-200 °C. Pretreatment: 5%H_2/Ar, 250 °C, 2 h. Reaction condition: 2.8 mg of Co_3O_4 nanoparticles pellets + 0.1 g of quartz sands, 10 mL/min of CO+O_2 (CO:O_2=1:2.5) at 80-120 °C, 80 mL/min of CO+O_2 (CO:O_2=1:2.5) at 160-200 °C.

Kinetics of CO oxidation on the catalyst at two different temperature range corresponding to two different surface phases were studied. Kinetic studies were carried out on Co_3O_4@CoO in the temperature range of 80ºC-120ºC for CoO (Figure 6.7). A similar kinetic study was done in the temperature range at 160ºC-200ºC for the Co_3O_4@Co_3O_4 surface. As the conversions in the temperature range of 160ºC-200ºC are much higher than those in 80ºC-120ºC, a larger flow rate of CO and O_2 was used for the kinetics of Co_3O_4@Co_3O_4 in the temperature range of 160-200ºC so that the CO conversion could remain at a conversion lower than 15%. Figure 6.6 presents the Arrhenius plots of CoO surface phase of Co_3O_4@CoO catalyst in the temperature range of 80-120ºC (red line) and of formed Co_3O_4 surface phase of Co_3O_4@Co_3O_4catalyst in the temperature range of 160ºC-200ºC (black line). The activation barriers for CO oxidation on CoO and Co_3O_4 were calculated from the slopes of the two Arrhenius plots in Figure 6.6. The activation barrier for CO oxidation on Co_3O_4 in the temperature range of 160-200ºC is 36.9 kJ/mol, obviously lower than 49.3 kJ/mol for CO oxidation on CoO surface in the temperature range of 80-140ºC. The lower activation barrier of Co_3O_4 for CO oxidation than CoO is probably related to the existence of Co^{3+} on Co_3O_4 and the lack of Co^{3+}on CoO since Co^{3+} was proposed to be the favorable site for chemisorbing CO in contrast to CoO.[13]

6.4 Conclusion

CO oxidation on surface CoO phase of Co_3O_4@CoO catalyst nanoparticles was studied with AP-XPS in the mixture of 0.4 mbar CO and 1 mbar O_2 at 60-220ºC. Surface CoO phase was structurally stable during CO oxidation in the temperature range of 60-140ºC. The apparent activation energy for CO oxidation on CoO is 49.3 kJ/mol. At a catalysis temperature higher than

140 ºC, the surface CoO phase was restructured to Co_3O_4 surface phase during catalysis. Compared to surface phase CoO, the formed surface phase Co_3O_4 of Co_3O_4@Co_3O_4 is more active for CO oxidation, evidenced by its low apparent activation energy of 36.9 kJ/mol. Here the reported restructuring of surface phase of CoO to Co_3O_4 during CO oxidation demonstrated (1) possible restructurings of surface region of transition metal oxide-based catalysts and (2) necessity of tracking surface phase of a transition metal oxide-based catalyst during catalysis. This feature that surface of oxide-based catalysts could be potentially restructured during catalysis likely results from the complexity of surface structures of transition metal oxide catalysts rooting from the existence of multiple phases of a transition metal oxide.

List of publications in KU

(1) **Tang, Y**.; Li, Y.; Fung, V.; Jiang, D.-e.; Huang, W.; Zhang, S.; Iwasawa, Y.; Sakata, T.; Nguyen, L.; Zhang, X.; Tao, F. F.; Single rhodium atoms anchored in micropores for efficient transformation of methane under mild conditions. ***Nature communications*** 2018**,** *9* (1), 1231.

(2) Chen, Y.;[ǂ] deGlee, B.;[ǂ] **Tang, Y.**;[ǂ] Wang, Z.; Zhao, B.; Wei, Y.; Zhang, L.; Yoo, S.; Pei, K.; Kim, J. H.; Ding, Y.; Tao, F. F.; A robust fuel cell operated on nearly dry methane at 500° C enabled by synergistic thermal catalysis and electrocatalysis. ***Nature Energy,*** 3, 1042-1050. ([ǂ]=equal contribution)

(3) **Tang, Y.**, *et al* and Tao, F. F.; Synergy Effect of Two Sets of Single-Atom Sites (Ni_1 and Ru_1) on Catalyst Surface for Reforming CH_4, ***Journal of the American Chemical Society***, accepted, manusript ID: ja-2018-10910a.R1

(4) **Tang, Y.**; Ma, L.; Dou, J.; Andolina, C. M.; Li, Y.; Ma, H.; House, S. D.; Zhang, X.; Yang, J.; Tao, F. F., Transition of surface phase of cobalt oxide during CO oxidation. ***Physical Chemistry Chemical Physics*** 2018**,** *20* (9), 6440-6449.

(5) **Tang, Y**.; Nguyen, L.; Li, Y. T.; Wang, N.; Tao, F., Surface of a catalyst in a gas phase. ***Current Opinion in Chemical Engineering*** 2016**,** *12*, 52-61.

(6) Huang, W. X.; Zhang, S. R.; **Tang, Y.;** Li, Y. T.; Nguyen, L.; Li, Y. Y.; Shan, J. J.; Xiao, D. Q.; Gagne, R.; Frenkel, A. I.; Tao, F., Low-Temperature Transformation of Methane to Methanol on Pd1O4 Single Sites Anchored on the Internal Surface of Microporous Silicate. ***Angewandte Chemie-International Edition*** 2016**,** *55* (43), 13441-13445.

(7) Cao, S. W.; Tao, F.; **Tang, Y.**; Li, Y. T.; Yu, J. G., Size- and shape-dependent catalytic performances of oxidation and reduction reactions on nanocatalysts. ***Chemical Society Reviews*** 2016**,** *45* (17), 4747-4765.

(8) Nguyen, L.; Tao, F.; Liu, H.; Dou, J.; **Tang, Y**.; Bao, X.; Understanding of Catalyst Surface during Catalysis through Ambient Pressure X-ray Photoelectron Spectroscopy. ***Chemical Reviews*** 2018, accepted.

(9) Li, Y.; **Tang, Y.**; Nguyen, L.; Tao, F. F., Catalytic oxidation of ethane to carboxylic acids in liquid phase at near room temperature ***ACS Sustainable Chemistry & Engineering*** 2018, accepted.

(10) Li, Y.; Khivantsev, N.; **Tang, Y.**; Nguyen, L.; Liu, J.; Yu, M.; Tao, F., Synthesis of Na@ nanoFAU zeolite catalyst and catalysis for production of formic acid on in Na@ nanoFAU. ***Catalysis Letters*** 2018, accepted.

(11) Li, J.; **Tang, Y**.; Ma, Y.; Zhang, Z.; Tao, F.; Qu, Y., In-Situ Formation of Isolated Bimetallic PtCe Sites of Single-Dispersed Pt on CeO2 for Low Temperature CO Oxidation. ***ACS Applied Materials & Interfaces*** 2018, accepted.

(12) Zhang, X. Y.; Sun, Z. C.; Wang, B.; **Tang, Y.**; Nguyen, L.; Li, Y. T.; Tao, F. F., C-C Coupling on Single-Atom-Based Heterogeneous Catalyst. ***Journal of the American Chemical Society*** 2018**,** *140* (3), 954-962.

(13) Zhang, X. Y.; House, S. D.; **Tang, Y.**; Nguyen, L.; Li, Y. T.; Opalade, A. A.; Yang, J. C.; Sun, Z. C.; Tao, F. F., Complete Oxidation of Methane on NiO Nanoclusters Supported on CeO2 Nanorods through Synergistic Effect. ***ACS Sustainable Chemistry & Engineering*** 2018**,** *6* (5), 6467-6477.

(14) Rawal, T. B.; Acharya, S. R.; Hong, S.; Le, D.; **Tang, Y.**; Tao, F. F.; Rahman, T. S., High Catalytic Activity of Pd1/ZnO (10$\bar{1}$0) toward Methanol Partial Oxidation: A DFT+ KMC Study. ***ACS Catalysis*** 2018**,** *8* (6), 5553-5569.

(15) Phivilay, S. P.; Roberts, C. A.; Gamalski, A. D.; Stach, E. A.; Zhang, S. R.; Nguyen, L.; **Tang, Y**.; Xiong, A. K.; Puretzky, A. A.; Tao, F. F.; Domen, K.; Wachs, I. E., Anatomy of a Visible Light Activated Photocatalyst for Water Splitting. ***ACS Catalysis*** 2018**,** *8* (7), 6650-6658.

(16) Nguyen, L.; Tao, P. P. C.; Liu, H. M.; Al-Hada, M.; Amati, M.; Sezen, H.; Gregoratti, L.; **Tang, Y.**; House, S. D.; Tao, F. F., X-ray Photoelectron Spectroscopy Studies of Nanoparticles Dispersed in Static Liquid. ***Langmuir*** 2018**,** *34* (33), 9606-9616.

(17) Nguyen, L.; Tao, P.; Liu, H. M.; Al-Hada, M.; Amati, M.; Sezen, H.; **Tang, Y.**; Gregoratti, L.; Tao, F., Studies of surface of metal nanoparticles in a flowing liquid with XPS. ***Chemical Communications*** 2018**,** *54* (71), 9981-9984.

(18) Nguyen, L.; **Tang, Y.**; Li, Y.; Zhang, X.; Wang, D.; Tao, F., Dual reactor for in situ/operando fluorescent mode XAS studies of sample containing low-concentration 3d or 5d metal elements. ***Review of Scientific Instruments*** 2018**,** *89* (5), 054103.

(19) Liu, J. J.; Fung, V.; Wang, Y.; Du, K. M.; Zhang, S. R.; Nguyen, L.; **Tang, Y.**; Fan, J.; Jiang, D. E.; Tao, F. F., Promotion of catalytic selectivity on transition metal oxide through restructuring surface lattice. ***Applied Catalysis B-Environmental*** 2018**,** *237*, 957-969.

(20) Khivantsev, K.; Jaegers, N. R.; Kovarik, L.; Hanson, J. C.; Tao, F.; **Tang, Y.**; Zhang, X.; Koleva, I. Z.; Aleksandrov, H. A.; Vayssilov, G. N., Achieving Atomic Dispersion of Highly Loaded Transition Metals in Small-pore Zeolite SSZ-13: A New Class of High-capacity and High-efficiency Low Temperature CO and NOx Adsorbers. ***Angewandte Chemie*** 2018, accepted.

(21) Dou, J.; **Tang, Y.**; Nie, L. H.; Andolina, C. M.; Zhang, X. Y.; House, S.; Li, Y. T.; Yang, J.; Tao, F. F., Complete Oxidation of Methane on Co3O4/CeO2 Nanocomposite: A Synergic Effect. ***Catalysis Today*** 2018**,** *311*, 48-55.

(22) Celik, G.; Ailawar, S. A.; Sohn, H.; **Tang, Y.**; Tao, F. F.; Miller, J. T.; Edmiston, P. L.; Ozkan, U. S., Swellable Organically Modified Silica (SOMS) as a Catalyst Scaffold for Catalytic Treatment of Water Contaminated with Trichloroethylene. ***ACS Catalysis*** 2018**,** *8* (8), 6796-6809.

(23) Cai, W.; Mu, R.; Zha, S.; Sun, G.; Chen, S.; Zhao, Z.-J.; Li, H.; Tian, H.; **Tang, Y**.; Tao, F. F., Subsurface catalysis-mediated selectivity of dehydrogenation reaction. ***Science advances*** 2018, *4* (8), eaar5418.

(24) Bergman, S. L.; Granestrand, J.; **Tang, Y**.; Paris, R. S.; Nilsson, M.; Tao, F. F.; Tang, C. H.; Pennycook, S. J.; Pettersson, L. J.; Bernasek, S. L., In-situ characterization by Near-Ambient Pressure XPS of the catalytically active phase of Pt/Al2O3 during NO and CO oxidation. ***Applied Catalysis B-Environmental*** 2018**,** *220*, 506-511.

(25) Takanabe, K.; Khan, A. M.; **Tang, Y.**; Nguyen, L.; Ziani, A.; Jacobs, B. W.; Elbaz, A. M.; Sarathy, S. M.; Tao, F. F., Integrated In Situ Characterization of a Molten Salt Catalyst Surface: Evidence of Sodium Peroxide and Hydroxyl Radical Formation. ***Angewandte Chemie-International Edition*** 2017**,** *56* (35), 10403-10407.

(26) Shan, J. J.; Zhang, S. R.; Choksi, T.; Nguyen, L.; Bonifacio, C. S.; Li, Y. Y.; Zhu, W.; **Tang, Y**.; Zhang, Y. W.; Yang, J. C.; Greeley, J.; Frenkel, A. I.; Tao, F., Tuning Catalytic Performance through a Single or Sequential Post Synthesis Reaction(s) in a Gas Phase. ***ACS Catalysis*** 2017**,** *7* (1), 191-204.

(27) Mueanngern, Y.; Yang, X.; **Tang, Y.;** Tao, F.; Baker, L. R., Catalysis at Multiple Length Scales: Crotonaldehyde Hydrogenation at Nanoscale and Mesoscale Interfaces in Platinum-Cerium Oxide Catalysts. ***Journal of Physical Chemistry C*** 2017**,** *121* (25), 13765-13776.

(28) Dou, J.; **Tang, Y.**; Nguyen, L.; Tong, X.; Thapa, P. S.; Tao, F. F., Oxidation of Cyclohexene Catalyzed by Nanoporous Au(Ag) in Liquid Phase. ***Catalysis Letters*** 2017**,** *147* (2), 442-452.

(29) Tao, F. F.; Nguyen, L.; Zhang, S. R.; Li, Y. Y.; **Tang, Y.**; Zhang, L.; Frenkel, A. I.; Xia, Y. N.; Salmeron, M., Formation of Second-Generation Nanoclusters on Metal Nanoparticles Driven by Reactant Gases. ***Nano Letters*** 2016**,** *16* (8), 5001-5009.

(30) Tao, F.; **Tang, Y.,** Heterogenous catalysis: more than skimming the surface. ***Nature Chemistry*** 2016**,** *8* (10), 902-903.

Presentation

(1) Yu Tang, Shiran Zhang, Franklin (Feng) Tao, Selective Hydrodeoxygenation of Anisole on a Cobalt Oxide-Based Bi-Functional Catalyst, North American Catalysis Society Meeting (NAM25), 2017, Oral Presentation

(2) Franklin (Feng) Tao, Yu Tang, *et al*, Catalytic transformation of methane to acetic acid under mild conditions, ACS Fall meeting, 2017, Oral Presentation

(3) Yu Tang, Shiran Zhang, Franklin (Feng) Tao, Selective Hydrodeoxygenation of Anisole on a Cobalt Oxide-based Bifunctional Catalyst at Low Temperature, Gordon Research Conference: Catalysis, 2016, Poster

Appendix A: general experiment protocol

Catalytic performance was evaluated in a fixed bed flow reactor as shown in **Figure A1**. The catalyst was installed in the tube reactor in the center of the figure. It was fixed by quartz wool plugs. A K-type thermal couple coated with stainless steel tube was kept contacting with catalyst bed to measure the temperature. The temperature of the catalyst was controlled by a programable PID controller (Omega Engineering, US). The flow rate of reactant gases was controlled by mass flow controller (Dakota Instrument, US). The flow rate was further confirmed by a bubble flowmeter. The gaseous products composition was analyzed by an on-line GC (SRI-8610, SRI Instrument, US) equipped with a TCD detector. There are two columns used for the separation of the gas product, a molecule sieve column (MX-13, 6 ft) and a polymer column (Hayasep-D, 6 ft).

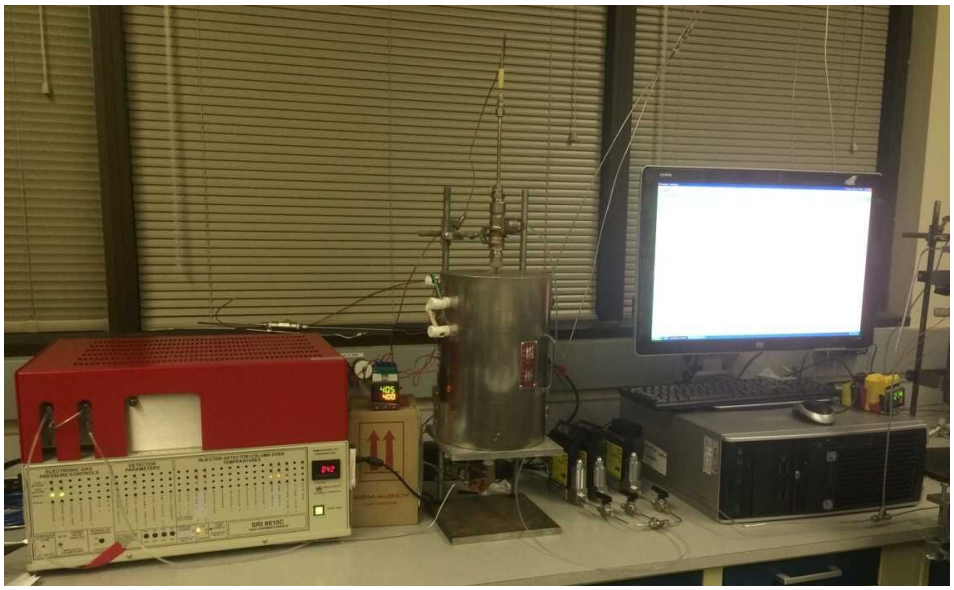

Figure A1 experiment setup to measure catalytic activity and selectivity for methane reforming. From left to right: on-line GC, fixed bed reactor, mass flow controller units and data processing PC.

In a typical catalytic measurement, the catalyst was kept at the desired temperature and the gas product composition was analyzed by GC for at 3 times. The average of the three times

measurement was reported for further analysis. More data entries need be collected to obtain three stable value if the results were not consistent.

The catalytic parameters of methane dry reforming are calculated as the equation below:

$$Conversion = \frac{[CH_4]_{initial} - [CH_4]}{[CH_4]_{initial}} * 100\%$$

$$Selectivity = \frac{1/2 * [H_2]}{[CH_4]_{initial} - [CH_4]} * 100\%$$

To determine the apparent activation energies, kinetic studies were carried out by using certain amount of catalyst diluted with 300 mg purified quartz loaded in the fixed-bed quartz reactor. The catalyst was activated at 300 ºC for 60 min with 10% H_2 balanced with Ar with a flow rate of 30 mL/min. Kinetic experiments were performed by using a relatively higher flow of mixture of CH_4 and CO_2 reactants to obtain lower conversions (<20%) in the temperature range of kinetics studies (500-560 ºC).[68] In the kinetics studies, the reactant feed flows of CH_4 (10% in Ar) and CO_2 (10% in Ar) are 40 mL/min, respectively.

To determine the turnover frequency (TOF) of the methane reforming, the catalytic data in the kinetics-controlled regime were analyzed. TOFs in term of hydrogen production rate (molecules per second) per metal site was calculated by dividing the number of produced H_2 molecules per second by the number of active sites of catalyst. The active sites of these catalysts of this work are Ni_1 for $Ni_{0.05}Ce_{0.95}O_2$, Ru_1 for $Ru_{0.05}Ce_{0.95}O_2$ or Ni_1 together with Ru_1 for $Ni_{0.025}Ru_{0.025}Ce_{0.95}O_2$. The numbers of the surface Ni or Ru sites on surface were estimated through the atomic ratio of Ni or Ru to Ce of the topmost layer of a catalyst with the equation below.

$$TOF = \frac{2 * Yield\ (H_2) * N_A * molar\ flow\ rate(CH_4)}{catalyst\ mass * Surface\ area * Surface\ density(Ce) * \frac{Surface_{metal}}{Surface_{Ce}}}$$

$$\frac{Surface_{metal}}{Surface_{Ce}} = \frac{\frac{Area(Ni2p)}{Cross\ section\ factor(Ni\ 2p)} + \frac{Area(Ru3p)}{Cross\ section\ factor(Ru3p)}}{\frac{Area\ (Ce\ 3d)}{\text{Cross section factor (Ce 3d)}}}$$

Appendix B deconvolution of Ce*3d* XPS spectrum

Ce*3d* XPS spectrum could be readily deconvoluted to ten components, which are assigned to Ce^{3+} and Ce^{4+}. The surface ratio could be evaluated by equation below, where U0, V0, U' and V' are assigned to Ce^{3+} and U, V, U'', V'', U''' and V''' are assigned to Ce^{4+}.[56]

$$surface\ Ce^{3+}\ ratio = \frac{Ce^{3+}}{Ce^{3+} + Ce^{4+}} = \frac{U0 + V0 + U' + V'}{U0 + V0 + U' + V' + U + V + U'' + V'' + U''' + V'''}$$

The deconvolution results of Ce*3d* spectrum of Rh_1/CeO_2 catalyst is shown as **Figure B1** and **Table B1**.

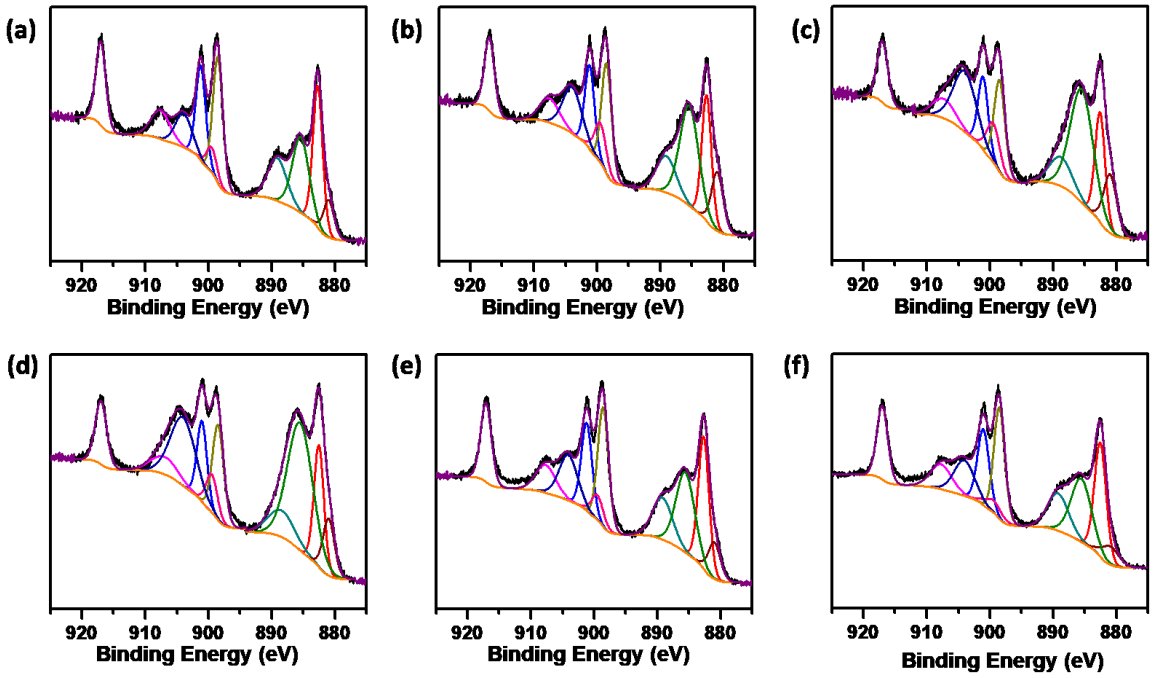

Figure B1 deconvoluted Ce3d spectrum of Rh_1/CeO_2 catalyst. (a) in UHV, (b) reduced at 300°C, in steam reforming at (c) 500 °C and (d) 650°C, in dry reforming at (e) 500°C and (f) 650°C.

Table 1 deconvolution results of Ce3d of Rh_1/CeO_2 catalyst under different conditions.

Conditions	UHV	300°C reduced	500°C SRM	650°C SRM	500°C DRM	650°C DRM
V	1636924	1341897	1045056	1621445	2469626	2647322

U	109128	894603	696707	1080969	1646425	1764890
V''	962838	789304	614702	953734	1452634	1557155
U''	641892	526202	409801	635822	968422	1038103
V'''	1487963	1219785	949956	1473893	2244890	2406416
U'''	991975.47	813190	633304	982596	1496593	1604277
V0	474129	774162	740929	891508	792369	631979
U0	316086	516108	493952	594338	528246	421319
V'	1488528	2074286	2459522	4311553	2599368	2563381
U''	666402	965055	1320568	2315207	1477803	1428996
Ce^{3+} ratio	**0.335596**	**0.436691**	**0.53553**	**0.545897**	**0.344326**	**0.314101**

The deconvolution results of Ce*3d* spectrum of $(Ni_1+Ru_1)/CeO_2$ catalyst is shown as **Figure B2**.

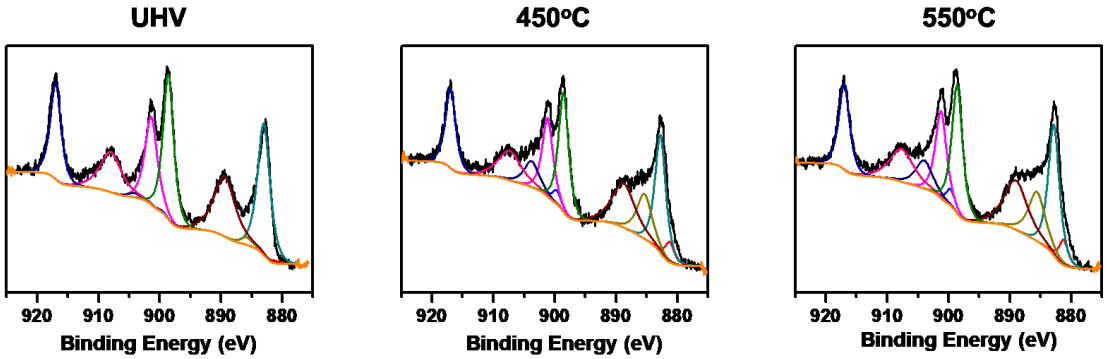

Figure B2 deconvolution of Ce3d spectrum of $(Ni_1+Ru_1)/CeO_2$ catalyst at (a) UHV, dry reforming at (b) 450°C and (c) 550°C. The Ce^{3+} ratio is 2.3%, 19.2% and 20.2%.

Appendix C supplementary data for chapter 5

1) Stability

Stability test of (Ni_1+Ru_1)/CeO_2 catalyst was examined for 60 hrs. 30 mg catalyst was used in the test. As shown in **Figure D1**, the conversion of methane and selectivity to hydrogen were stable during the test of 60 hrs, showing the stability of the catalyst.

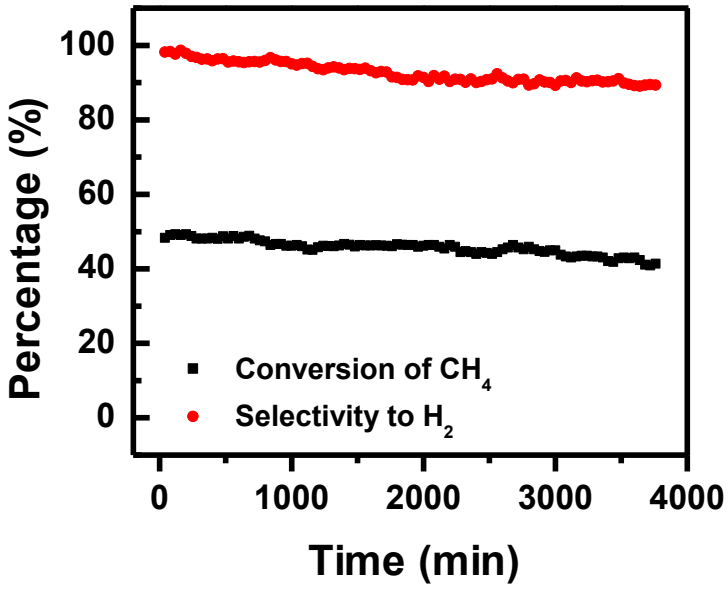

Figure C1 stability test of methane reforming catalyzed by (Ni_1+Ru_1)/CeO_2 catalyst.

2) Carbon balance

Carbon balance during methane dry reforming was examined by the equation below. The carbon balance remains >95% in the 60 hrs test, suggesting there is merely coke formation on the catatlyst.

$$carbon\ balance = \frac{[CH_4] + [CO_2] + [CO]}{[CH_4]_{initial} + [CO_2]_{initial}} * 100\%$$

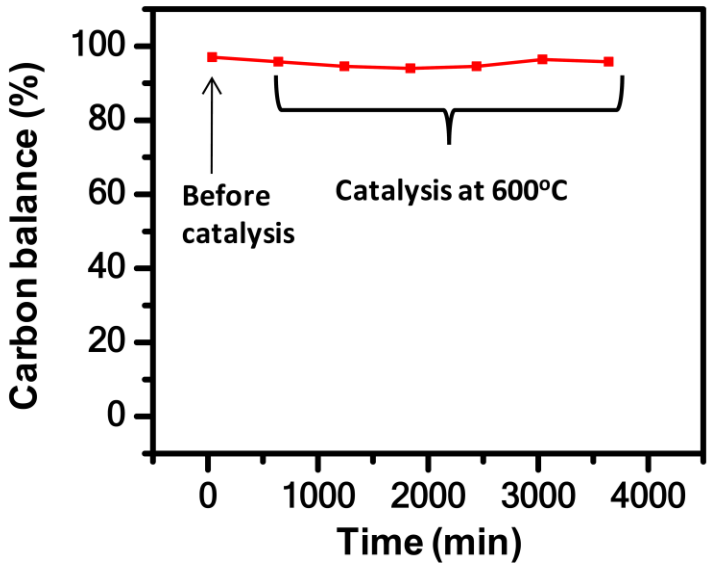

Figure C2 carbon balance of methane reforming catalyzed by $(Ni_1+Ru_1)/CeO_2$ catalyst.

Reference

(1) Hagen, J., *Industrial catalysis: a practical approach*. John Wiley & Sons: 2015.
(2) Ertl, G.; Knözinger, H.; Weitkamp, J., Handbook of heterogeneous catalysis. **1997**.
(3) Ertl, G., *Reactions at solid surfaces*. John Wiley & Sons: 2010; Vol. 14.
(4) Somorjai, G. A.; Li, Y., *Introduction to surface chemistry and catalysis*. John Wiley & Sons: 2010.
(5) Vannice, M. A., An analysis of the Mars–van Krevelen rate expression. *Catalysis Today* **2007,** *123* (1-4), 18-22.
(6) Kim, H. Y.; Henkelman, G., CO oxidation at the interface of Au nanoclusters and the stepped-CeO2 (111) surface by the Mars–van Krevelen mechanism. *The journal of physical chemistry letters* **2012,** *4* (1), 216-221.
(7) Khenkin, A. M.; Weiner, L.; Wang, Y.; Neumann, R., Electron and Oxygen Transfer in Polyoxometalate, H5PV2Mo10O40, Catalyzed Oxidation of Aromatic and Alkyl Aromatic Compounds: Evidence for Aerobic Mars− van Krevelen-Type Reactions in the Liquid Homogeneous Phase. *Journal of the American Chemical Society* **2001,** *123* (35), 8531-8542.
(8) Almeida, A. R.; Moulijn, J. A.; Mul, G., Photocatalytic Oxidation of Cyclohexane over TiO2: Evidence for a Mars− Van Krevelen Mechanism. *The Journal of Physical Chemistry C* **2011,** *115* (4), 1330-1338.
(9) Zhang, S.; Nguyen, L.; Zhu, Y.; Zhan, S.; Tsung, C.-K.; Tao, F., In-situ studies of nanocatalysis. *Accounts of chemical research* **2013,** *46* (8), 1731-1739.
(10) Cai, W.; Mu, R.; Zha, S.; Sun, G.; Chen, S.; Zhao, Z.-J.; Li, H.; Tian, H.; Tang, Y.; Tao, F. F., Subsurface catalysis-mediated selectivity of dehydrogenation reaction. *Science advances* **2018,** *4* (8), eaar5418.
(11) Cao, S. W.; Tao, F.; Tang, Y.; Li, Y. T.; Yu, J. G., Size- and shape-dependent catalytic performances of oxidation and reduction reactions on nanocatalysts. *Chemical Society Reviews* **2016,** *45* (17), 4747-4765.
(12) Ni, B.; Wang, X., Face the edges: catalytic active sites of nanomaterials. *Advanced Science* **2015,** *2* (7), 1500085.
(13) Wang, D.; Li, Y., Bimetallic nanocrystals: liquid-phase synthesis and catalytic applications. *Advanced Materials* **2011,** *23* (9), 1044-1060.
(14) Liu, X.; Wang, D.; Li, Y., Synthesis and catalytic properties of bimetallic nanomaterials with various architectures. *Nano Today* **2012,** *7* (5), 448-466.
(15) Liu, Y.; Zhao, G.; Wang, D.; Li, Y., Heterogeneous catalysis for green chemistry based on nanocrystals. *National Science Review* **2015,** *2* (2), 150-166.
(16) Yan, B.; Yang, X.; Yao, S.; Wan, J.; Myint, M.; Gomez, E.; Xie, Z.; Kattel, S.; Xu, W.; Chen, J. G., Dry reforming of ethane and butane with CO2 over PtNi/CeO2 bimetallic catalysts. *ACS Catalysis* **2016,** *6* (11), 7283-7292.
(17) Liu, J. J.; Fung, V.; Wang, Y.; Du, K. M.; Zhang, S. R.; Nguyen, L.; Tang, Y.; Fan, J.; Jiang, D. E.; Tao, F. F., Promotion of catalytic selectivity on transition metal oxide through restructuring surface lattice. *Applied Catalysis B-Environmental* **2018,** *237*, 957-969.
(18) Qiao, B.; Wang, A.; Yang, X.; Allard, L. F.; Jiang, Z.; Cui, Y.; Liu, J.; Li, J.; Zhang, T., Single-atom catalysis of CO oxidation using Pt 1/FeO x. *Nature chemistry* **2011,** *3* (8), 634.
(19) Yang, X. F.; Wang, A. Q.; Qiao, B. T.; Li, J.; Liu, J. Y.; Zhang, T., Single-Atom Catalysts: A New Frontier in Heterogeneous Catalysis. *Accounts of Chemical Research* **2013,** *46* (8), 1740-1748.

(20) Wang, Y.; Mao, J.; Meng, X.; Yu, L.; Deng, D.; Bao, X., Catalysis with Two-Dimensional Materials Confining Single Atoms: Concept, Design, and Applications. *Chemical Reviews* **2018**.
(21) Wang, A.; Li, J.; Zhang, T., Heterogeneous single-atom catalysis. *Nature Reviews Chemistry* **2018**, 1.
(22) Grabow, L. C.; Gokhale, A. A.; Evans, S. T.; Dumesic, J. A.; Mavrikakis, M., Mechanism of the water gas shift reaction on Pt: First principles, experiments, and microkinetic modeling. *The Journal of Physical Chemistry C* **2008,** *112* (12), 4608-4617.
(23) Zhang, S.; Shan, J.-j.; Zhu, Y.; Frenkel, A. I.; Patlolla, A.; Huang, W.; Yoon, S. J.; Wang, L.; Yoshida, H.; Takeda, S., WGS Catalysis and In Situ Studies of CoO1–x, PtCo n/Co3O4, and Pt m Co m′/CoO1–x Nanorod Catalysts. *Journal of the American Chemical Society* **2013,** *135* (22), 8283-8293.
(24) Ackermann, M. D.; Pedersen, T. M.; Hendriksen, B. L. M.; Robach, O.; Bobaru, S. C.; Popa, I.; Quiros, C.; Kim, H.; Hammer, B.; Ferrer, S.; Frenken, J. W. M., Structure and reactivity of surface oxides on Pt(110) during catalytic CO oxidation. *Phys. Rev. Lett.* **2005,** *95* (25).
(25) Labinger, J. A.; Bercaw, J. E., Understanding and exploiting C-H bond activation. *Nature* **2002,** *417* (6888), 507-514.
(26) Schwach, P.; Pan, X.; Bao, X., Direct Conversion of Methane to Value-Added Chemicals over Heterogeneous Catalysts: Challenges and Prospects. *Chemical reviews* **2017,** *117* (13), 8497-8520.
(27) Behrens, M.; Studt, F.; Kasatkin, I.; Kühl, S.; Hävecker, M.; Abild-Pedersen, F.; Zander, S.; Girgsdies, F.; Kurr, P.; Kniep, B.-L., The active site of methanol synthesis over Cu/ZnO/Al2O3 industrial catalysts. *Science* **2012**, 1219831.
(28) Kattel, S.; Ramírez, P. J.; Chen, J. G.; Rodriguez, J. A.; Liu, P., Active sites for CO2 hydrogenation to methanol on Cu/ZnO catalysts. *Science* **2017,** *355* (6331), 1296-1299.
(29) Schulz, H., Short history and present trends of Fischer–Tropsch synthesis. *Applied Catalysis A: General* **1999,** *186* (1-2), 3-12.
(30) Iglesia, E., Design, synthesis, and use of cobalt-based Fischer-Tropsch synthesis catalysts. *Applied Catalysis A: General* **1997,** *161* (1-2), 59-78.
(31) van Ravenhorst, I. K.; Vogt, C.; Oosterbeek, H.; Bossers, K. W.; Moya-Cancino, J. G.; van Bavel, A. P.; van der Eerden, A. M.; Vine, D.; de Groot, F. M.; Meirer, F., Capturing the Genesis of an Active Fischer–Tropsch Synthesis Catalyst with Operando X-ray Nanospectroscopy. *Angewandte Chemie* **2018,** *130* (37), 12133-12138.
(32) Yang, J.; Pan, X.; Jiao, F.; Li, J.; Bao, X., Direct conversion of syngas to aromatics. *Chemical Communications* **2017,** *53* (81), 11146-11149.
(33) Cheng, K.; Zhou, W.; Kang, J.; He, S.; Shi, S.; Zhang, Q.; Pan, Y.; Wen, W.; Wang, Y., Bifunctional catalysts for one-step conversion of syngas into aromatics with excellent selectivity and stability. *Chem* **2017,** *3* (2), 334-347.
(34) Zhao, B.; Zhai, P.; Wang, P.; Li, J.; Li, T.; Peng, M.; Zhao, M.; Hu, G.; Yang, Y.; Li, Y.-W., Direct transformation of syngas to aromatics over Na-Zn-Fe5C2 and hierarchical HZSM-5 tandem catalysts. *Chem* **2017,** *3* (2), 323-333.
(35) Pappas, I.; Chirik, P. J., Ammonia synthesis by hydrogenolysis of titanium–nitrogen bonds using proton coupled electron transfer. *Journal of the American Chemical Society* **2015,** *137* (10), 3498-3501.
(36) Elkins, T. W.; Hagelin-Weaver, H. E., Characterization of Mn–Na 2 WO 4/SiO 2 and Mn–Na 2 WO 4/MgO catalysts for the oxidative coupling of methane. *Applied Catalysis A: General* **2015,** *497*, 96-106.

(37) Arndt, S.; Otremba, T.; Simon, U.; Yildiz, M.; Schubert, H.; Schomacker, R., Mn-Na2WO4/SiO2 as catalyst for the oxidative coupling of methane. What is really known? *Applied Catalysis a-General* **2012,** *425*, 53-61.
(38) Ji, S. F.; Xiao, T. C.; Li, S. B.; Xu, C. Z.; Hou, R. L.; Coleman, K. S.; Green, M. L. H., The relationship between the structure and the performance of Na-W-Mn/SiO2 catalysts for the oxidative coupling of methane. *Applied Catalysis a-General* **2002,** *225* (1-2), 271-284.
(39) Otsuka, K.; Said, A.; Jinno, K.; Komatsu, T., Peroxide anions as possible active species in oxidative coupling of methane. *Chemistry Letters* **1987,** *16* (1), 77-80.
(40) Ji, S. F.; Xiao, T. C.; Li, S. B.; Chou, L. J.; Zhang, B.; Xu, C. Z.; Hou, R. L.; York, A. P. E.; Green, M. L. H., Surface WO4 tetrahedron: the essence of the oxidative coupling of methane over M-W-Mn/SiO2 catalysts. *Journal of Catalysis* **2003,** *220* (1), 47-56.
(41) Palermo, A.; Vazquez, J. P. H.; Lee, A. F.; Tikhov, M. S.; Lambert, R. M., Critical influence of the amorphous silica-to-cristobalite phase transition on the performance of Mn/Na2WO4/SiO2 catalysts for the oxidative coupling of methane. *Journal of Catalysis* **1998,** *177* (2), 259-266.
(42) Wang, L.; Tao, L.; Xie, M.; Xu, G.; Huang, J.; Xu, Y., Dehydrogenation and aromatization of methane under non-oxidizing conditions. *Catalysis Letters* **1993,** *21* (1), 35-41.
(43) Guo, X.; Fang, G.; Li, G.; Ma, H.; Fan, H.; Yu, L.; Ma, C.; Wu, X.; Deng, D.; Wei, M., Direct, nonoxidative conversion of methane to ethylene, aromatics, and hydrogen. *Science* **2014,** *344* (6184), 616-619.
(44) Liu, Y.; Li, D.; Wang, T.; Liu, Y.; Xu, T.; Zhang, Y., Efficient conversion of methane to aromatics by coupling methylation reaction. *ACS Catalysis* **2016,** *6* (8), 5366-5370.
(45) Xu, T.; Liu, Y.; Wang, T.; Zhang, Y., Methane Conversion. Google Patents: 2018.
(46) Lezcano-González, I.; Oord, R.; Rovezzi, M.; Glatzel, P.; Botchway, S. W.; Weckhuysen, B. M.; Beale, A. M., Molybdenum Speciation and its Impact on Catalytic Activity during Methane Dehydroaromatization in Zeolite ZSM-5 as Revealed by Operando X-Ray Methods. *Angewandte Chemie International Edition* **2016,** *55* (17), 5215-5219.
(47) Kosinov, N.; Coumans, F. J.; Uslamin, E. A.; Wijpkema, A. S.; Mezari, B.; Hensen, E. J., Methane dehydroaromatization by Mo/HZSM-5: mono-or bifunctional catalysis? *ACS Catalysis* **2016,** *7* (1), 520-529.
(48) Periana, R. A.; Mironov, O.; Taube, D.; Bhalla, G.; Jones, C., Catalytic, oxidative condensation of CH4 to CH3COOH in one step via CH activation. *Science* **2003,** *301* (5634), 814-818.
(49) Tang, Y.; Li, Y.; Fung, V.; Jiang, D.-e.; Huang, W.; Zhang, S.; Iwasawa, Y.; Sakata, T.; Nguyen, L.; Zhang, X., Single rhodium atoms anchored in micropores for efficient transformation of methane under mild conditions. *Nature communications* **2018,** *9* (1), 1231.
(50) Lin, M.; Sen, A., Direct catalytic conversion of methane to acetic acid in an aqueous medium. *Nature* **1994,** *368* (6472), 613-615.
(51) Lin, M. R.; Hogan, T. E.; Sen, A., Catalytic carbon-carbon and carbon-hydrogen bond cleavage in lower alkanes. Low-temperature hydroxylations and hydroxycarbonylations with dioxygen as the oxidant. *Journal of the American Chemical Society* **1996,** *118* (19), 4574-4580.
(52) Huang, W. X.; Zhang, S. R.; Tang, Y.; Li, Y. T.; Nguyen, L.; Li, Y. Y.; Shan, J. J.; Xiao, D. Q.; Gagne, R.; Frenkel, A. I.; Tao, F., Low-Temperature Transformation of Methane to Methanol on Pd1O4 Single Sites Anchored on the Internal Surface of Microporous Silicate. *Angewandte Chemie-International Edition* **2016,** *55* (43), 13441-13445.

(53) Watts, J. F.; Wolstenholme, J., An introduction to surface analysis by XPS and AES. *An Introduction to Surface Analysis by XPS and AES, by John F. Watts, John Wolstenholme, pp. 224. ISBN 0-470-84713-1. Wiley-VCH, May 2003.* **2003**, 224.
(54) Dupin, J.-C.; Gonbeau, D.; Vinatier, P.; Levasseur, A., Systematic XPS studies of metal oxides, hydroxides and peroxides. *Physical Chemistry Chemical Physics* **2000,** *2* (6), 1319-1324.
(55) Chastain, J.; King, R. C.; Moulder, J., *Handbook of X-ray photoelectron spectroscopy: a reference book of standard spectra for identification and interpretation of XPS data*. Physical Electronics Division, Perkin-Elmer Corporation Eden Prairie, Minnesota: 1992.
(56) Mullins, D.; Overbury, S.; Huntley, D., Electron spectroscopy of single crystal and polycrystalline cerium oxide surfaces. *Surface Science* **1998,** *409* (2), 307-319.
(57) Bêche, E.; Charvin, P.; Perarnau, D.; Abanades, S.; Flamant, G., Ce 3d XPS investigation of cerium oxides and mixed cerium oxide (CexTiyOz). *Surface and Interface Analysis* **2008,** *40* (3-4), 264-267.
(58) Paparazzo, E., On the curve-fitting of XPS Ce (3d) spectra of cerium oxides. *Materials Research Bulletin* **2011,** *46* (2), 323-326.
(59) Bunker, G., *Introduction to XAFS: a practical guide to X-ray absorption fine structure spectroscopy*. Cambridge University Press: 2010.
(60) Newville, M., Fundamentals of XAFS. *Reviews in Mineralogy and Geochemistry* **2014,** *78* (1), 33-74.
(61) Calvin, S., *XAFS for Everyone*. CRC press: 2013.
(62) Stern, E., Musings about the development of XAFS. *Journal of synchrotron radiation* **2001,** *8* (2), 49-54.
(63) Penner-Hahn, J. E., X-ray absorption spectroscopy in coordination chemistry. *Coordination Chemistry Reviews* **1999,** *190*, 1101-1123.
(64) Iwasawa, Y.; Asakura, K.; Tada, M., *XAFS techniques for catalysts, nanomaterials, and surfaces*. Springer: 2017.
(65) Ravel, B.; Newville, M., ATHENA, ARTEMIS, HEPHAESTUS: data analysis for X-ray absorption spectroscopy using IFEFFIT. *Journal of synchrotron radiation* **2005,** *12* (4), 537-541.
(66) Tang, Y.; Pattengale, B.; Ludwig, J.; Atifi, A.; Zinovev, A. V.; Dong, B.; Kong, Q.; Zuo, X.; Zhang, X.; Huang, J., Direct Observation of Photoinduced Charge Separation in Ruthenium Complex/Ni (OH) 2 Nanoparticle Hybrid. *Scientific reports* **2015,** *5*, 18505.
(67) Zhang, S.; Nguyen, L.; Liang, J.-X.; Shan, J.; Liu, J.; Frenkel, A. I.; Patlolla, A.; Huang, W.; Li, J.; Tao, F., Catalysis on singly dispersed bimetallic sites. *Nature communications* **2015,** *6*, 7938.
(68) Tang, Y.; Ma, L.; Dou, J.; Andolina, C. M.; Li, Y.; Ma, H.; House, S. D.; Zhang, X.; Yang, J.; Tao, F. F., Transition of surface phase of cobalt oxide during CO oxidation. *Physical Chemistry Chemical Physics* **2018,** *20* (9), 6440-6449.
(69) Liu, J., Catalysis by supported single metal atoms. *Acs Catalysis* **2016,** *7* (1), 34-59.
(70) Liu, J., Advanced electron microscopy characterization of nanostructured heterogeneous catalysts. *Microscopy and microanalysis* **2004,** *10* (1), 55-76.
(71) Tao, F.; Dag, S.; Wang, L.-W.; Liu, Z.; Butcher, D. R.; Salmeron, M.; Somorjai, G. A., Restructuring of hex-Pt (100) under CO gas environments: formation of 2-D nanoclusters. *Nano letters* **2009,** *9* (5), 2167-2171.
(72) Tao, F.; Dag, S.; Wang, L. W.; Liu, Z.; Butcher, D. R.; Bluhm, H.; Salmeron, M.; Somorjai, G. A., Break-Up of Stepped Platinum Catalyst Surfaces by High CO Coverage. *Science* **2010,** *327* (5967), 850-853.

(73) Roy, K.; Artiglia, L.; van Bokhoven, J. A., Ambient Pressure Photoelectron Spectroscopy: Opportunities in Catalysis from Solids to Liquids and Introducing Time Resolution. *ChemCatChem* **2018,** *10* (4), 666-682.
(74) Bordiga, S.; Groppo, E.; Agostini, G.; van Bokhoven, J. A.; Lamberti, C., Reactivity of surface species in heterogeneous catalysts probed by in situ X-ray absorption techniques. *Chemical Reviews* **2013,** *113* (3), 1736-1850.
(75) Nguyen, L.; Tao, F.; Liu, H.; Dou, J.; Tang, Y. B., X, Understanding of Catalyst Surface during Catalysis through Ambient Pressure X-ray Photoelectron Spectroscopy. *Chemical Reviews* **2018**, In revision.
(76) Dou, J.; Sun, Z.; Opalade, A. A.; Wang, N.; Fu, W.; Tao, F. F., Operando chemistry of catalyst surfaces during catalysis. *Chemical Society Reviews* **2017,** *46* (7), 2001-2027.
(77) Tang, Y.; Nguyen, L.; Li, Y. T.; Wang, N.; Tao, F., Surface of a catalyst in a gas phase. *Current Opinion in Chemical Engineering* **2016,** *12*, 52-61.
(78) Salmeron, M.; Schlögl, R., Ambient pressure photoelectron spectroscopy: A new tool for surface science and nanotechnology. *Surface Science Reports* **2008,** *63* (4), 169-199.
(79) Nguyen, L.; Tao, F., Development of a reaction cell for in-situ/operando studies of surface of a catalyst under a reaction condition and during catalysis. *Review of Scientific Instruments* **2016,** *87* (6), 064101.
(80) Kerherve, G.; Regoutz, A.; Bentley, D.; Hood, C.; Feeley, K.; Knight, S.; Robson, A.; Turner, C.; Singh, N.; Pontefract, J., Laboratory-based high pressure X-ray photoelectron spectroscopy: A novel and flexible reaction cell approach. *Review of Scientific Instruments* **2017,** *88* (3), 033102.
(81) Clausen, B. S.; Steffensen, G.; Fabius, B.; Villadsen, J.; Feidenhans'l, R.; Topsøe, H., In situ cell for combined XRD and on-line catalysis tests: Studies of Cu-based water gas shift and methanol catalysts. *Journal of Catalysis* **1991,** *132* (2), 524-535.
(82) Nguyen, L.; Tang, Y.; Li, Y.; Zhang, X.; Wang, D.; Tao, F., Dual reactor for in situ/operando fluorescent mode XAS studies of sample containing low-concentration 3d or 5d metal elements. *Review of Scientific Instruments* **2018,** *89* (5), 054103.
(83) Karim, A. M.; Howard, C.; Roberts, B.; Kovarik, L.; Zhang, L.; King, D. L.; Wang, Y., In situ X-ray absorption fine structure studies on the effect of pH on Pt electronic density during aqueous phase reforming of glycerol. *ACS Catalysis* **2012,** *2* (11), 2387-2394.
(84) Clausen, B. S.; Topsøe, H.; Frahm, R., Application of Combined X-Ray Diffraction and Absorption Techniques for in Situ Catalyst Characterization. 1998; pp 315-344.
(85) Grunwaldt, J.-D.; Clausen, B. S., Combining XRD and EXAFS with on-Line Catalytic Studies for in situ Characterization of Catalysts. *Topics in Catalysis* **2002,** *18* (1/2), 37-43.
(86) Meitzner, G.; Iglesia, E., New insights into methanol synthesis catalysts from X-ray absorption spectroscopy. *Catalysis Today* **1999,** *53* (3), 433-441.
(87) Kawai, T.; Bando, K. K.; Lee, Y. K.; Oyama, S. T.; Chun, W. J.; Asakura, K., EXAFS measurements of a working catalyst in the liquid phase: An in situ study of a Ni2P hydrodesulfurization catalyst. *Journal of Catalysis* **2006,** *241* (1), 20-24.
(88) Kawai, T.; Chun, W.-J.; Asakura, K.; Koike, Y.; Nomura, M.; Bando, K. K.; Ted Oyama, S.; Sumiya, H., Design of a high-temperature and high-pressure liquid flow cell for x-ray absorption fine structure measurements under catalytic reaction conditions. *The Review of scientific instruments* **2008,** *79*, 014101-014101.
(89) Seifert, F.; Paris, E.; Dingwell, D.; Davoli, I.; Mottana, A., *A high-temperature device for in situ measurement of X-ray adsorption spectra*. 1994.

(90) Nashner, M. S.; Frenkel, A. I.; Adler, D. L.; Shapley, J. R.; Nuzzo, R. G., Structural characterization of carbon-supported platinum-ruthenium nanoparticles from the molecular cluster precursor PtRu5C(CO)(16). *Journal of the American Chemical Society* **1997,** *119* (33), 7760-7771.
(91) Jentoft, R.; Deutsch, S.; Gates, B., Low-cost, heated, and/or cooled flow-through cell for transmission x-ray absorption spectroscopy. *Review of scientific instruments* **1996,** *67* (6), 2111-2112.
(92) Odzak, J.; Argo, A.; Lai, F.; Gates, B.; Pandya, K.; Feraria, L., A flow-through x-ray absorption spectroscopy cell for characterization of powder catalysts in the working state. *Review of Scientific Instruments* **2001,** *72* (10), 3943-3945.
(93) Hannemann, S.; Casapu, M.; Grunwaldt, J.-D.; Haider, P.; Trüssel, P.; Baiker, A.; Welter, E., A versatile in situ spectroscopic cell for fluorescence/transmission EXAFS and X-ray diffraction of heterogeneous catalysts in gas and liquid phase. *Journal of synchrotron radiation* **2007,** *14* (4), 345-354.
(94) Li, Y.; Zakharov, D.; Zhao, S.; Tappero, R.; Jung, U.; Elsen, A.; Baumann, P.; Nuzzo, R. G.; Stach, E.; Frenkel, A., Complex structural dynamics of nanocatalysts revealed in Operando conditions by correlated imaging and spectroscopy probes. *Nature communications* **2015,** *6*, 7583.
(95) Tao, F.; Crozier, P. A., Atomic-Scale Observations of Catalyst Structures under Reaction Conditions and during Catalysis. *Chemical Reviews* **2016,** *116* (6), 3487-3539.
(96) Marton, L., La microscopie electronique des objets biologiques. *Bull Classe Sci Acad Roy Belgique* **1935,** *21*, 553-564.
(97) Takeda, S.; Yoshida, H., Atomic-resolution environmental TEM for quantitative in-situ microscopy in materials science. *Microscopy* **2013,** *62* (1), 193-203.
(98) Hansen, T. W.; Wagner, J. B.; Dunin-Borkowski, R. E., Aberration corrected and monochromated environmental transmission electron microscopy: challenges and prospects for materials science. *Materials Science and Technology* **2010,** *26* (11), 1338-1344.
(99) Wu, Y. M. A.; Li, L.; Li, Z.; Kinaci, A.; Chan, M. K. Y.; Sun, Y. G.; Guest, J. R.; McNulty, I.; Rajh, T.; Liu, Y. Z., Visualizing Redox Dynamics of a Single Ag/AgCl Heterogeneous Nanocatalyst at Atomic Resolution. *Acs Nano* **2016,** *10* (3), 3738-3746.
(100) Wu, J. B.; Shan, H.; Chen, W. L.; Gu, X.; Tao, P.; Song, C. Y.; Shang, W.; Deng, T., In Situ Environmental TEM in Imaging Gas and Liquid Phase Chemical Reactions for Materials Research. *Advanced Materials* **2016,** *28* (44), 9686-9712.
(101) Ganzler, A. M.; Casapu, M.; Vernoux, P.; Loridant, S.; Aires, F.; Epicier, T.; Betz, B.; Hoyer, R.; Grunwaldt, J. D., Tuning the Structure of Platinum Particles on Ceria InSitu for Enhancing the Catalytic Performance of Exhaust Gas Catalysts. *Angewandte Chemie-International Edition* **2017,** *56* (42), 13078-13082.
(102) Kamiuchi, N.; Sun, K.; Aso, R.; Tane, M.; Tamaoka, T.; Yoshida, H.; Takeda, S., Self-activated surface dynamics in gold catalysts under reaction environments. *Nature Communications* **2018,** *9*.
(103) Chenna, S.; Banerjee, R.; Crozier, P. A., Atomic-Scale Observation of the Ni Activation Process for Partial Oxidation of Methane Using In Situ Environmental TEM. *Chemcatchem* **2011,** *3* (6), 1051-1059.
(104) Jinschek, J. R., Advances in the environmental transmission electron microscope (ETEM) for nanoscale in situ studies of gas-solid interactions. *Chemical Communications* **2014,** *50* (21), 2696-2706.

(105) DeLaRiva, A. T.; Hansen, T. W.; Challa, S. R.; Datye, A. K., In situ Transmission Electron Microscopy of catalyst sintering. *Journal of Catalysis* **2013,** *308*, 291-305.
(106) Gai, P. L.; Boyes, E. D.; Helveg, S.; Hansen, P. L.; Giorgio, S.; Henry, C. R., Atomic-resolution environmental transmission electron microscopy for probing gas-solid reactions in heterogeneous catalysis. *Mrs Bulletin* **2007,** *32* (12), 1044-1050.
(107) Wang, R.; Crozier, P. A.; Sharma, R.; Adams, J. B., Measuring the redox activity of individual catalytic nanoparticles in cerium-based oxides. *Nano Letters* **2008,** *8* (3), 962-967.
(108) Rodriguez, J. A.; Hanson, J. C.; Stacchiola, D.; Senanayake, S. D., In situ/operando studies for the production of hydrogen through the water-gas shift on metal oxide catalysts. *Physical Chemistry Chemical Physics* **2013,** *15* (29), 12004-12025.
(109) Alayoglu, S.; Beaumont, S. K.; Zheng, F.; Pushkarev, V. V.; Zheng, H. M.; Iablokov, V.; Liu, Z.; Guo, J. H.; Kruse, N.; Somorjai, G. A., CO2 Hydrogenation Studies on Co and CoPt Bimetallic Nanoparticles Under Reaction Conditions Using TEM, XPS and NEXAFS. *Topics in Catalysis* **2011,** *54* (13-15), 778-785.
(110) Gai, P. L., Developments in in situ environmental cell high-resolution electron microscopy and applications to catalysis. *Topics in Catalysis* **2002,** *21* (4), 161-173.
(111) Creemer, J. F.; Helveg, S.; Hoveling, G. H.; Ullmann, S.; Molenbroek, A. M.; Sarro, P. M.; Zandbergen, H. W., Atomic-scale electron microscopy at ambient pressure. *Ultramicroscopy* **2008,** *108* (9), 993-998.
(112) Dou, J.; Bao, Z.; Yu, F., Mesoporous Ni (OH) 2/CeNixOy composites derived Ni/CeNixOy catalysts for dry reforming of methane. *ChemCatChem* **2018,** *10* (1), 250-258.
(113) Lunsford, J. H., Catalytic conversion of methane to more useful chemicals and fuels: a challenge for the 21st century. *Catalysis Today* **2000,** *63* (2-4), 165-174.
(114) Liu, Z.; Grinter, D. C.; Lustemberg, P. G.; Nguyen-Phan, T. D.; Zhou, Y.; Luo, S.; Waluyo, I.; Crumlin, E. J.; Stacchiola, D. J.; Zhou, J., Dry Reforming of Methane on a Highly-Active Ni-CeO2 Catalyst: Effects of Metal-Support Interactions on C− H Bond Breaking. *Angewandte Chemie International Edition* **2016,** *55* (26), 7455-7459.
(115) Li, S.; Gong, J., Strategies for improving the performance and stability of Ni-based catalysts for reforming reactions. *Chemical Society Reviews* **2014,** *43* (21), 7245-7256.
(116) Trovarelli, A., Catalytic properties of ceria and CeO2-containing materials. *Catalysis Reviews-Science and Engineering* **1996,** *38* (4), 439-520.
(117) Liu, X. W.; Zhou, K. B.; Wang, L.; Wang, B. Y.; Li, Y. D., Oxygen Vacancy Clusters Promoting Reducibility and Activity of Ceria Nanorods. *Journal of the American Chemical Society* **2009,** *131* (9), 3140-+.
(118) Mai, H.-X.; Sun, L.-D.; Zhang, Y.-W.; Si, R.; Feng, W.; Zhang, H.-P.; Liu, H.-C.; Yan, C.-H., Shape-selective synthesis and oxygen storage behavior of ceria nanopolyhedra, nanorods, and nanocubes. *The Journal of Physical Chemistry B* **2005,** *109* (51), 24380-24385.
(119) Zhang, S.; Chang, C.-R.; Huang, Z.-Q.; Li, J.; Wu, Z.; Ma, Y.; Zhang, Z.; Wang, Y.; Qu, Y., High catalytic activity and chemoselectivity of sub-nanometric Pd clusters on porous nanorods of CeO2 for hydrogenation of nitroarenes. *Journal of the American Chemical Society* **2016,** *138* (8), 2629-2637.
(120) Nguyen, L.; Tao, F., Reactor for tracking catalyst nanoparticles in liquid at high temperature under a high-pressure gas phase with X-ray absorption spectroscopy. *Review of Scientific Instruments* **2018,** *89* (2), 024102.
(121) Lang, R.; Li, T.; Matsumura, D.; Miao, S.; Ren, Y.; Cui, Y. T.; Tan, Y.; Qiao, B.; Li, L.; Wang, A., Hydroformylation of Olefins by a Rhodium Single-Atom Catalyst with Activity

Comparable to RhCl (PPh3) 3. *Angewandte Chemie International Edition* **2016,** *55* (52), 16054-16058.
(122) Atkins, P.; Overton, T., *Shriver and Atkins' inorganic chemistry*. Oxford University Press, USA: 2010.
(123) Yates Jr, J.; Duncan, T.; Worley, S.; Vaughan, R., Infrared spectra of chemisorbed CO on Rh. *The Journal of Chemical Physics* **1979,** *70* (3), 1219-1224.
(124) Kwon, Y.; Kim, T. Y.; Kwon, G.; Yi, J.; Lee, H., Selective activation of methane on single-atom catalyst of rhodium dispersed on zirconia for direct conversion. *Journal of the American Chemical Society* **2017,** *139* (48), 17694-17699.
(125) Zhang, S.; Tang, Y.; Nguyen, L.; Zhao, Y.-F.; Wu, Z.; Goh, T.-W.; Liu, J. J.; Li, Y.; Zhu, T.; Huang, W., Catalysis on Singly Dispersed Rh Atoms Anchored on an Inert Support. *ACS Catalysis* **2017,** *8* (1), 110-121.
(126) Guan, H.; Lin, J.; Qiao, B.; Miao, S.; Wang, A. Q.; Wang, X.; Zhang, T., Enhanced performance of Rh1/TiO2 catalyst without methanation in water-gas shift reaction. *AIChE Journal* **2017,** *63* (6), 2081-2088.
(127) Fung, V.; Tao, F. F.; Jiang, D.-e., Low-temperature activation of methane on anchored single atoms: descriptor and prediction. *Physical Chemistry Chemical Physics* **2018**.
(128) Wei, J. M.; Iglesia, E., Isotopic and kinetic assessment of the mechanism of reactions of CH4 with CO2 or H2O to form synthesis gas and carbon on nickel catalysts. *Journal of Catalysis* **2004,** *224* (2), 370-383.
(129) Wei, J. M.; Iglesia, E., Structural requirements and reaction pathways in methane activation and chemical conversion catalyzed by rhodium. *Journal of Catalysis* **2004,** *225* (1), 116-127.
(130) Yamaguchi, A.; Iglesia, E., Catalytic activation and reforming of methane on supported palladium clusters. *Journal of Catalysis* **2010,** *274* (1), 52-63.
(131) Wei, J. M.; Iglesia, E., Mechanism and site requirements for activation and chemical conversion of methane on supported Pt clusters and turnover rate comparisons among noble metals. *Journal of Physical Chemistry B* **2004,** *108* (13), 4094-4103.
(132) Wei, J. M.; Iglesia, E., Reaction pathways and site requirements for the activation and chemical conversion of methane on Ru-based catalysts. *Journal of Physical Chemistry B* **2004,** *108* (22), 7253-7262.
(133) Wei, J. M.; Iglesia, E., Isotopic and kinetic assessment of the mechanism of methane reforming and decomposition reactions on supported iridium catalysts. *Physical Chemistry Chemical Physics* **2004,** *6* (13), 3754-3759.
(134) Wang, Z.; Cao, X.-M.; Zhu, J.; Hu, P., Activity and coke formation of nickel and nickel carbide in dry reforming: a deactivation scheme from density functional theory. *Journal of Catalysis* **2014,** *311*, 469-480.
(135) Gayen, A.; Priolkar, K.; Sarode, P.; Jayaram, V.; Hegde, M.; Subbanna, G.; Emura, S., Ce1-x Rh x O2-δ Solid Solution Formation in Combustion-Synthesized Rh/CeO2 Catalyst Studied by XRD, TEM, XPS, and EXAFS. *Chemistry of materials* **2004,** *16* (11), 2317-2328.
(136) Wei, J.; Iglesia, E., Reaction pathways and site requirements for the activation and chemical conversion of methane on Ru− based catalysts. *The Journal of Physical Chemistry B* **2004,** *108* (22), 7253-7262.
(137) Wei, J.; Iglesia, E., Structural and mechanistic requirements for methane activation and chemical conversion on supported iridium clusters. *Angewandte Chemie International Edition* **2004,** *43* (28), 3685-3688.

(138) Wei, J.; Iglesia, E., Structural requirements and reaction pathways in methane activation and chemical conversion catalyzed by rhodium. *Journal of Catalysis* **2004,** *225* (1), 116-127.
(139) Spivey, J. J.; Hutchings, G., Catalytic aromatization of methane. *Chemical Society Reviews* **2014,** *43* (3), 792-803.
(140) Yi, N.; Cao, Y.; Liu, Y.-M.; Dai, W.-L.; He, H.-Y.; Fan, K.-N., Highly Efficient Ni–Ce–O Mixed Oxide Catalysts via Gel-coprecipitation of Oxalate Precursors for Catalytic Combustion of Methane. *Chemistry letters* **2005,** *34* (1), 108-109.
(141) Pena, M. A.; Gomez, J. P.; Fierro, J. L. G., New catalytic routes for syngas and hydrogen production. *Applied Catalysis a-General* **1996,** *144* (1-2), 7-57.
(142) Song, C. S.; Wei, P., Tri-reforming of methane: a novel concept for catalytic production of industrially useful synthesis gas with desired H-2/CO ratios. *Catalysis Today* **2004,** *98* (4), 463-484.
(143) Pakhare, D.; Spivey, J., A review of dry (CO 2) reforming of methane over noble metal catalysts. *Chemical Society Reviews* **2014,** *43* (22), 7813-7837.
(144) Gonzalez-delaCruz, V. M.; Pereñiguez, R.; Ternero, F.; Holgado, J. P.; Caballero, A., In situ XAS study of synergic effects on Ni–Co/ZrO2 methane reforming catalysts. *The Journal of Physical Chemistry C* **2012,** *116* (4), 2919-2926.
(145) Fan, M. S.; Abdullah, A. Z.; Bhatia, S., Catalytic technology for carbon dioxide reforming of methane to synthesis gas. *ChemCatChem* **2009,** *1* (2), 192-208.
(146) Hansen, T. W.; DeLaRiva, A. T.; Challa, S. R.; Datye, A. K., Sintering of catalytic nanoparticles: particle migration or Ostwald ripening? *Accounts of chemical research* **2013,** *46* (8), 1720-1730.
(147) Trimm, D. L., Coke formation and minimisation during steam reforming reactions. *Catalysis Today* **1997,** *37* (3), 233-238.
(148) Trimm, D. L., Catalysts for the control of coking during steam reforming. *Catalysis Today* **1999,** *49* (1-3), 3-10.
(149) Ginsburg, J. M.; Piña, J.; El Solh, T.; De Lasa, H. I., Coke formation over a nickel catalyst under methane dry reforming conditions: thermodynamic and kinetic models. *Industrial & engineering chemistry research* **2005,** *44* (14), 4846-4854.
(150) Lustemberg, P. G.; Ramírez, P. J.; Liu, Z.; Gutiérrez, R. A.; Grinter, D. G.; Carrasco, J.; Senanayake, S. D.; Rodriguez, J. A.; Ganduglia-Pirovano, M. V., Room-Temperature Activation of Methane and Dry Re-forming with CO2 on Ni-CeO2(111) Surfaces: Effect of Ce3+ Sites and Metal–Support Interactions on C–H Bond Cleavage. *ACS Catal.* **2016,** *6* (12), 8184-8191.
(151) Rodriguez, J. A.; Grinter, D. C.; Liu, Z.; Palomino, R. M.; Senanayake, S. D., Ceria-based model catalysts: fundamental studies on the importance of the metal–ceria interface in CO oxidation, the water–gas shift, CO 2 hydrogenation, and methane and alcohol reforming. *Chemical Society Reviews* **2017,** *46* (7), 1824-1841.
(152) Xu, W.; Liu, Z.; Johnston-Peck, A. C.; Senanayake, S. D.; Zhou, G.; Stacchiola, D.; Stach, E. A.; Rodriguez, J. A., Steam reforming of ethanol on Ni/CeO2: reaction pathway and interaction between Ni and the CeO2 support. *ACS Catalysis* **2013,** *3* (5), 975-984.
(153) Tao, F. F.; Shan, J.-j.; Nguyen, L.; Wang, Z.; Zhang, S.; Zhang, L.; Wu, Z.; Huang, W.; Zeng, S.; Hu, P., Understanding complete oxidation of methane on spinel oxides at a molecular level. *Nature communications* **2015,** *6*, 7798.
(154) Nguyen, L.; Zhang, S.; Wang, L.; Li, Y.; Yoshida, H.; Patlolla, A.; Takeda, S.; Frenkel, A. I.; Tao, F., Reduction of Nitric Oxide with Hydrogen on Catalysts of Singly Dispersed Bimetallic Sites Pt1Co m and Pd1Co n. *ACS Catalysis* **2016,** *6* (2), 840-850.

(155) Fung, V.; Tao, F.; Jiang, D. E., Low-temperature activation of methane on doped single atoms: descriptor and prediction. *Physical Chemistry Chemical Physics* **2018,** *20* (35), 22909-22914.
(156) Shan, J.; Huang, W.; Nguyen, L.; Yu, Y.; Zhang, S.; Li, Y.; Frenkel, A. I.; Tao, F., Conversion of methane to methanol with a bent mono (μ-oxo) dinickel anchored on the internal surfaces of micropores. *Langmuir* **2014,** *30* (28), 8558-8569.
(157) Zhu, Y.; Zhang, S.; Shan, J.-j.; Nguyen, L.; Zhan, S.; Gu, X.; Tao, F., In situ surface chemistries and catalytic performances of ceria doped with palladium, platinum, and rhodium in methane partial oxidation for the production of syngas. *Acs Catalysis* **2013,** *3* (11), 2627-2639.
(158) Xie, Z. H.; Yan, B. H.; Kattel, S.; Lee, J. H.; Yao, S. Y.; Wu, Q. Y.; Rui, N.; Gomez, E.; Liu, Z. Y.; Xu, W. Q.; Zhang, L.; Chen, J. G. G., Dry reforming of methane over CeO2-supported Pt-Co catalysts with enhanced activity. *Applied Catalysis B-Environmental* **2018,** *236*, 280-293.
(159) Chen, Y.; Tang, Y.; Wang, Z.; Zhao, B.; Wei, Y.; Zhang, L.; Yoo, S.; Pei, K.; Kim, J. H.; Ding, Y., A robust fuel cell operated on nearly dry methane at 500° C enabled by synergistic thermal catalysis and electrocatalysis. *Nature Energy* **2018**, accepted.
(160) Kresse, G.; Furthmüller, J., Efficient iterative schemes for ab initio total-energy calculations using a plane-wave basis set. *Phys. Rev. B* **1996,** *54* (16), 11169-11186.
(161) Kresse, G.; Furthmuller, J., Efficiency of ab-initio total energy calculations for metals and semiconductors using a plane-wave basis set. *Comp. Mater. Sci.* **1996,** *6* (1), 15-50.
(162) Kresse, G.; Hafner, J., Ab-Initio Molecular-Dynamics Simulation of the Liquid-Metal Amorphous-Semiconductor Transition in Germanium. *Phys. Rev. B* **1994,** *49* (20), 14251-14269.
(163) Kresse, G.; Hafner, J., Ab initio molecular dynamics for liquid metals. *Phys. Rev. B* **1993,** *47* (1), 558-561.
(164) Perdew, J. P.; Burke, K.; Ernzerhof, M., Generalized Gradient Approximation Made Simple. *Phys. Rev. Lett.* **1996,** *77* (18), 3865-3868.
(165) Kresse, G.; Joubert, D., From ultrasoft pseudopotentials to the projector augmented-wave method. *Phys. Rev. B* **1999,** *59* (3), 1758-1775.
(166) Blöchl, P. E., Projector augmented-wave method. *Phys. Rev. B* **1994,** *50* (24), 17953-17979.
(167) Dudarev, S. L.; Botton, G. A.; Savrasov, S. Y.; Humphreys, C. J.; Sutton, A. P., Electron-energy-loss spectra and the structural stability of nickel oxide:An LSDA+U study. *Phys. Rev. B* **1998,** *57* (3), 1505-1509.
(168) Grimme, S.; Antony, J.; Ehrlich, S.; Krieg, H., A consistent and accurate ab initio parametrization of density functional dispersion correction (DFT-D) for the 94 elements H-Pu. *The Journal of Chemical Physics* **2010,** *132* (15), 154104.
(169) Michaelides, A.; Liu, Z. P.; Zhang, C. J.; Alavi, A.; King, D. A.; Hu, P., Identification of general linear relationships between activation energies and enthalpy changes for dissociation reactions at surfaces. *J. Am. Chem. Soc.* **2003,** *125* (13), 3704-3705.
(170) Liu, Z. P.; Hu, P., General rules for predicting where a catalytic reaction should occur on metal surfaces: A density functional theory study of C-H and C-O bond breaking/making on flat, stepped, and kinked metal surfaces. *J. Am. Chem. Soc.* **2003,** *125* (7), 1958-1967.
(171) Alavi, A.; Hu, P. J.; Deutsch, T.; Silvestrelli, P. L.; Hutter, J., CO oxidation on Pt(111): An ab initio density functional theory study. *Phys. Rev. Lett.* **1998,** *80* (16), 3650-3653.

(172) Newberg, J. T.; Starr, D. E.; Yamamoto, S.; Kaya, S.; Kendelewicz, T.; Mysak, E. R.; Porsgaard, S.; Salmeron, M. B.; Brown, G. E.; Nilsson, A., Formation of hydroxyl and water layers on MgO films studied with ambient pressure XPS. *Surface Science* **2011,** *605* (1), 89-94.
(173) Morgan, D. J., Resolving ruthenium: XPS studies of common ruthenium materials. *Surface and Interface Analysis* **2015,** *47* (11), 1072-1079.
(174) Grosvenor, A. P.; Biesinger, M. C.; Smart, R. S. C.; McIntyre, N. S., New interpretations of XPS spectra of nickel metal and oxides. *Surface Science* **2006,** *600* (9), 1771-1779.
(175) Sangaletti, L.; Depero, L.; Parmigiani, F., On the non-local screening mechanisms in the 2p photoelectron spectra of NiO and La2NiO4. *Solid state communications* **1997,** *103* (7), 421-424.
(176) Shannon, R. D., *Acta Cryst. A* **1976,** *32*, 751.
(177) Wang, Z.; Cao, X. M.; Zhu, J.; Hu, P., Activity and coke formation of nickel and nickel carbide in dry reforming: A deactivation scheme from density functional theory. *J. Catal.* **2014,** *311* (0), 469-480.
(178) Jones, G.; Jakobsen, J. G.; Shim, S. S.; Kleis, J.; Andersson, M. P.; Rossmeisl, J.; Abild-Pedersen, F.; Bligaard, T.; Helveg, S.; Hinnemann, B.; Rostrup-Nielsen, J. R.; Chorkendorff, I.; Sehested, J.; Norskov, J. K., First principles calculations and experimental insight into methane steam reforming over transition metal catalysts. *J. Catal.* **2008,** *259* (1), 147-160.
(179) Qadir, K.; Joo, S. H.; Mun, B. S.; Butcher, D. R.; Renzas, J. R.; Aksoy, F.; Liu, Z.; Somorjai, G. A.; Park, J. Y., Intrinsic relation between catalytic activity of CO oxidation on Ru nanoparticles and Ru oxides uncovered with ambient pressure XPS. *Nano letters* **2012,** *12* (11), 5761-8.
(180) Cao, S.; Tao, F. F.; Tang, Y.; Li, Y.; Yu, J., Size- and shape-dependent catalytic performances of oxidation and reduction reactions on nanocatalysts. *Chemical Society reviews* **2016,** *45* (17), 4747-65.
(181) Nguyen, L.; Liu, L.; Assefa, S.; Wolverton, C.; Schneider, W. F.; Tao, F. F., Atomic-Scale Structural Evolution of Rh(110) during Catalysis. *ACS Catal* **2017,** *7* (1), 664-674.
(182) Butcher, D. R.; Grass, M. E.; Zeng, Z.; Aksoy, F.; Bluhm, H.; Li, W. X.; Mun, B. S.; Somorjai, G. A.; Liu, Z., In situ oxidation study of Pt(110) and its interaction with CO. *J Am Chem Soc* **2011,** *133* (50), 20319-25.
(183) Miller, D.; Sanchez Casalongue, H.; Bluhm, H.; Ogasawara, H.; Nilsson, A.; Kaya, S., Different reactivity of the various platinum oxides and chemisorbed oxygen in CO oxidation on Pt(111). *J Am Chem Soc* **2014,** *136* (17), 6340-7.
(184) Toyoshima, R.; Yoshida, M.; Monya, Y.; Kousa, Y.; Suzuki, K.; Abe, H.; Mun, B. S.; Mase, K.; Amemiya, K.; Kondoh, H., In Situ Ambient Pressure XPS Study of CO Oxidation Reaction on Pd(111) Surfaces. *J. Phys. Chem. C* **2012,** *116* (35), 18691-18697.
(185) Tao, F.; Dag, S.; Wang, L.-W.; Liu, Z.; Butcher, D. R.; Bluhm, H.; Salmeron, M.; Somorjai, G. A., Break-Up of Stepped Platinum Catalyst Surfaces by High CO Coverage. *Science* **2010,** *327* (5967), 850.
(186) Okumura, M.; Haruta, M., Interplay of theoretical calculations and experiments for a study of catalysis by gold. *Catal. Today* **2016,** *259*, 81-86.
(187) Royer, S.; Duprez, D., Catalytic oxidation of carbon monoxide over transition metal oxides. *ChemCatChem* **2011,** *3* (1), 24-65.
(188) Nguyen, L.; Zhang, S. R.; Yoon, S. J.; Tao, F., Preferential Oxidation of CO in H-2 on Pure Co3O4-x and Pt/Co3O4-x. *Chemcatchem* **2015,** *7* (15), 2346-2353.

(189) Jansson, J.; Palmqvist, A. E. C.; Fridell, E.; Skoglundh, M.; Österlund, L.; Thormählen, P.; Langer, V., On the Catalytic Activity of Co3O4 in Low-Temperature CO Oxidation. *J. Catal.* **2002,** *211* (2), 387-397.
(190) Jiang, D. E.; Dai, S., The role of low-coordinate oxygen on Co3O4(110) in catalytic CO oxidation. *Physical Chemistry Chemical Physics* **2011,** *13* (3), 978-984.
(191) Binning, G.; Rohrer, H.; Gerber, C.; Weibel, E., SURFACE STUDIES BY SCANNING TUNNELING MICROSCOPY. *Physical Review Letters* **1982,** *49* (1), 57-61.
(192) Xie, X.; Li, Y.; Liu, Z. Q.; Haruta, M.; Shen, W., Low-temperature oxidation of CO catalysed by Co(3)O(4) nanorods. *Nature* **2009,** *458* (7239), 746-9.
(193) Iablokov, V.; Barbosa, R.; Pollefeyt, G.; Van Driessche, I.; Chenakin, S.; Kruse, N., Catalytic CO Oxidation over Well-Defined Cobalt Oxide Nanoparticles: Size-Reactivity Correlation. *ACS Catal.* **2015,** *5* (10), 5714-5718.
(194) Ren, Y.; Ma, Z.; Qian, L. P.; Dai, S.; He, H. Y.; Bruce, P. G., Ordered Crystalline Mesoporous Oxides as Catalysts for CO Oxidation. *Catalysis Letters* **2009,** *131* (1-2), 146-154.
(195) Xie, X. W.; Li, Y.; Liu, Z. Q.; Haruta, M.; Shen, W. J., Low-temperature oxidation of CO catalysed by Co3O4 nanorods. *Nature* **2009,** *458* (7239), 746-749.
(196) Sun, Y.; Lv, P.; Yang, J. Y.; He, L.; Nie, J. C.; Liu, X. W.; Li, Y. D., Ultrathin Co3O4 nanowires with high catalytic oxidation of CO. *Chemical Communications* **2011,** *47* (40), 11279-11281.
(197) Sun, H. Q.; Ang, H. M.; Tade, M. O.; Wang, S. B., Co3O4 nanocrystals with predominantly exposed facets: synthesis, environmental and energy applications. *Journal of Materials Chemistry A* **2013,** *1* (46), 14427-14442.
(198) Hu, L. H.; Sun, K. Q.; Peng, Q.; Xu, B. Q.; Li, Y. D., Surface Active Sites on Co3O4 Nanobelt and Nanocube Model Catalysts for CO Oxidation. *Nano Research* **2010,** *3* (5), 363-368.
(199) Lv, Y. G.; Li, Y.; Shen, W. J., Synthesis of Co3O4 nanotubes and their catalytic applications in CO oxidation. *Catalysis Communications* **2013,** *42*, 116-120.
(200) Lv, Y. G.; Li, Y.; Ta, N.; Shen, W. J., Co3O4 nanosheets: synthesis and catalytic application for CO oxidation at room temperature. *Science China-Chemistry* **2014,** *57* (6), 873-880.
(201) Choi, Y. I.; Yoon, H. J.; Kim, S. K.; Sohn, Y., Crystal-facet dependent CO oxidation, preferential oxidation of CO in H-2-rich, water-gas shift reactions, and supercapacitor application over Co3O4 nanostructures. *Applied Catalysis a-General* **2016,** *519*, 56-67.
(202) Gao, C. Y.; Dou, Z. F.; Liu, H.; Song, W. G., Low Cost Synthesis of 3D Flowerlike Co3O4 Nanostructures as Active Catalyst for CO Oxidation. *Chinese Journal of Catalysis* **2012,** *33* (8), 1334-1339.
(203) Jiang, D. E.; Dai, S., The role of low-coordinate oxygen on Co3O4(110) in catalytic CO oxidation. *Phys. Chem. Chem. Phys.* **2011,** *13* (3), 978-84.
(204) Broqvist, P.; Panas, I.; Persson, H., A DFT study on CO oxidation over Co3O4. *Journal of Catalysis* **2002,** *210* (1), 198-206.
(205) Xu, X. L.; Chen, Z. H.; Li, Y.; Chen, W. K.; Li, J. Q., Bulk and surface properties of spinel Co3O4 by density functional calculations. *Surface Science* **2009,** *603* (4), 653-658.
(206) Xu, X. L.; Yang, E.; Li, J. Q.; Li, Y.; Chen, W. K., A DFT Study of CO Catalytic Oxidation by N2O or O-2 on the Co3O4(110) Surface. *Chemcatchem* **2009,** *1* (3), 384-392.

(207) Wang, H. F.; Kavanagh, R.; Guo, Y. L.; Guo, Y.; Lu, G. Z.; Hu, P., Origin of extraordinarily high catalytic activity of Co3O4 and its morphological chemistry for CO oxidation at low temperature. *Journal of Catalysis* **2012,** *296*, 110-119.
(208) Pang, X. Y.; Liu, C.; Li, D. C.; Lv, C. Q.; Wang, G. C., Structure Sensitivity of CO Oxidation on Co3O4: A DFT Study. *Chemphyschem* **2013,** *14* (1), 204-212.
(209) Nagarajan, V.; Chandiramouli, R., A DFT study on adsorption behaviour of CO on Co3O4 nanostructures. *Applied Surface Science* **2016,** *385*, 113-121.
(210) Yu, Y.; Takei, T.; Ohashi, H.; He, H.; Zhang, X.; Haruta, M., Pretreatments of Co3O4 at moderate temperature for CO oxidation at −80°C. *J. Catal.* **2009,** *267* (2), 121-128.
(211) Henrich, V. E.; Cox, P. A., *The Surface Science of Metal Oxides*. Cambridge University Press: 1996.
(212) Zhang, S.; Shan, J.; Zhu, Y.; Nguyen, L.; Huang, W.; Yoshida, H.; Takeda, S.; Tao, F. F., Restructuring transition metal oxide nanorods for 100% selectivity in reduction of nitric oxide with carbon monoxide. *Nano. Lett.* **2013,** *13* (7), 3310-4.
(213) Nguyen, L.; Zhang, S.; Yoon, S. J.; Tao, F. F., Preferential Oxidation of CO in H2on Pure Co3O4−xand Pt/Co3O4−x. *ChemCatChem* **2015,** *7* (15), 2346-2353.
(214) Jain, A.; Ong, S. P.; G., H.; Chen, W.; Richards, W. D.; Dacek, S.; Cholia, S.; Gunter, D.; Skinner, D.; Ceder, G.; A., P. K., The Materials Project: A materials genome approach to accelerating materials innovation. *APL Materials* **2013,** *1*, 011002.
(215) Nguyen, L.; Tao, F. F., Development of a reaction cell for in-situ/operando studies of surface of a catalyst under a reaction condition and during catalysis. *The Review of scientific instruments* **2016,** *87* (6), 064101.
(216) Takanabe, K.; Khan, A. M.; Tang, Y.; Nguyen, L.; Ziani, A.; Jacobs, B. W.; Elbaz, A. M.; Sarathy, S. M.; Tao, F., *Angew. Chem. Int. Ed.* **2017,** *56*, DOI: 10.1002/anie.201704758.
(217) Zhu, Y.; Zhang, S.; Ye, Y.; Zhang, X.; Wang, L.; Zhu, W.; Cheng, F.; Tao, F., Catalytic Conversion of Carbon Dioxide to Methane on Ruthenium–Cobalt Bimetallic Nanocatalysts and Correlation between Surface Chemistry of Catalysts under Reaction Conditions and Catalytic Performances. *ACS Catal* **2012,** *2* (11), 2403-2408.
(218) Wang, L.; Zhang, S.; Zhu, Y.; Patlolla, A.; Shan, J.; Yoshida, H.; Takeda, S.; Frenkel, A. I.; Tao, F., Catalysis and In Situ Studies of Rh1/Co3O4Nanorods in Reduction of NO with H2. *ACS Catal* **2013,** *3* (5), 1011-1019.
(219) Zhang, S.; Shan, J. J.; Zhu, Y.; Frenkel, A. I.; Patlolla, A.; Huang, W.; Yoon, S. J.; Wang, L.; Yoshida, H.; Takeda, S.; Tao, F. F., WGS catalysis and in situ studies of CoO(1-x), PtCo(n)/Co3O4, and Pt(m)Co(m')/CoO(1-x) nanorod catalysts. *J Am Chem Soc* **2013,** *135* (22), 8283-93.
(220) Sohn, H.; Soykal, I. I.; Zhang, S.; Shan, J.; Tao, F.; Miller, J. T.; Ozkan, U. S., Effect of Cobalt on Reduction Characteristics of Ceria under Ethanol Steam Reforming Conditions: AP-XPS and XANES Studies. *J. Phys. Chem. C* **2016,** *120* (27), 14631-14642.
(221) Liu, J.; Zhang, S.; Zhou, Y.; Fung, V.; Nguyen, L.; Jiang, D.-e.; Shen, W.; Fan, J.; Tao, F. F., Tuning Catalytic Selectivity of Oxidative Catalysis through Deposition of Nonmetallic Atoms in Surface Lattice of Metal Oxide. *ACS Catal.* **2016,** *6* (7), 4218-4228.
(222) Zhang, S.; Nguyen, L.; Liang, J. X.; Shan, J.; Liu, J. J.; Frenkel, A. I.; Patlolla, A.; Huang, W.; Li, J.; Tao, F. F., Catalysis on singly dispersed bimetallic sites. *Nature communications* **2015,** *6*, 7938.

(223) Tao, F. F.; Shan, J. J.; Nguyen, L.; Wang, Z.; Zhang, S.; Zhang, L.; Wu, Z.; Huang, W.; Zeng, S.; Hu, P., Understanding complete oxidation of methane on spinel oxides at a molecular level. *Nature communications* **2015,** *6*, 7798.
(224) Jain, R.; Gnanakumar, E. S.; Gopinath, C. S., Mechanistic Aspects of Wet and Dry CO Oxidation on Co3O4 Nanorod Surfaces: A NAP-UPS Study. *Acs Omega* **2017,** *2* (3), 828-834.
(225) Huang, P.-C.; Chen, H.-S.; Liu, Y.-T.; Chen, I.-L.; Huang, S.-Y.; Nguyen, H. M.; Wang, K.-W.; Hu, C.-C.; Chen, T.-Y., Oxidation triggered atomic restructures enhancing the electrooxidation activities of carbon supported platinum–ruthenium catalysts. *CrystEngComm* **2014,** *16* (43), 10066-10079.
(226) Entani, S.; Kiguchi, M.; Saiki, K.; Koma, A., Epitaxial growth of CoO films on semiconductor and metal substrates by constructing a complex heterostructure. *Journal of Crystal Growth* **2003,** *247* (1-2), 110-118.
(227) Wang, F.; Hu, F.; Zhang, X. A.; Xu, H., IN SITU PHOTOELECTRON SPECTROSCOPY INVESTIGATION OF INTERFACE COUPLING BETWEEN METALS AND MoO3 THIN FILMS. *Surface Review and Letters* **2017,** *24* (4).
(228) Entani, S.; Kiguchi, M.; Saiki, K., Fabrication of polar CoO(111) thin films on Pt(111). *Surface Science* **2004,** *566*, 165-169.
(229) Zhou, M.; Pasquale, F. L.; Dowben, P. A.; Boosalis, A.; Schubert, M.; Darakchieva, V.; Yakimova, R.; Kong, L. M.; Kelber, J. A., Direct graphene growth on Co3O4(111) by molecular beam epitaxy. *Journal of Physics-Condensed Matter* **2012,** *24* (7).
(230) Wang, Y.; Kong, L. M.; Pasquale, F. L.; Cao, Y.; Dong, B.; Tanabe, I.; Binek, C.; Dowben, P. A.; Kelber, J. A., Graphene mediated domain formation in exchange coupled graphene/Co3O4(111)/Co(0001) trilayers. *Journal of Physics-Condensed Matter* **2013,** *25* (47).
(231) Petitto, S. C.; Marsh, E. M.; Carson, G. A.; Langell, M. A., Cobalt oxide surface chemistry: The interaction of CoO(100), Co3O4(110) and Co3O4(111) with oxygen and water. *Journal of Molecular Catalysis a-Chemical* **2008,** *281* (1-2), 49-58.
(232) Petitto, S. C.; Langell, M. A., Cu2O(110) formation on Co3O4(110) induced by copper impurity segregation. *Surface Science* **2005,** *599* (1-3), 27-40.
(233) Petitto, S. C.; Langell, M. A., Surface composition and structure of Co3O4(110) and the effect of impurity segregation. *Journal of Vacuum Science & Technology A* **2004,** *22* (4), 1690-1696.
(234) Marsh, E. M.; Petitto, S. C.; Harbison, G. S.; Wulser, K. W.; Langell, M. A., Deconvolution of the Co3O4(110) Fuchs-Kliewer phonon spectrum. *Journal of Vacuum Science & Technology A* **2005,** *23* (4), 1061-1066.
(235) Nydegger, M. W.; Couderc, G.; Langell, M. A., Surface composition of CoxNi1-xO solid solutions by X-ray photoelectron and Auger spectroscopies. *Applied Surface Science* **1999,** *147* (1-4), 58-66.
(236) Langell, M. A.; Pugmire, D. L.; McCarroll, W. H., Surface characterization of single crystal CO3O4 and CoO(100)/CO3O4 thin-film epitaxy. *Abstracts of Papers of the American Chemical Society* **2000,** *219*, U517-U517.
(237) Langell, M. A.; Gevrey, F.; Nydegger, M. W., Surface composition of MnxCo1-xO solid solution by X-ray photoelectron and Auger spectroscopies. *Applied Surface Science* **2000,** *153* (2-3), 114-127.
(238) Langell, M. A.; Anderson, M. D.; Carson, G. A.; Peng, L.; Smith, S., Valence-band electronic structure of Co3O4 epitaxy on CoO(100). *Physical Review B* **1999,** *59* (7), 4791-4798.

(239) Kim, J. G.; Pugmire, D. L.; Battaglia, D.; Langell, M. A., Analysis of the NiCo2O4 spinel surface with Auger and X-ray photoelectron spectroscopy. *Applied Surface Science* **2000,** *165* (1), 70-84.
(240) Carson, G. A.; Nassir, M. H.; Langell, M. A., Epitaxial growth of Co3O4 on CoO(100). *Journal of Vacuum Science & Technology a-Vacuum Surfaces and Films* **1996,** *14* (3), 1637-1642.
(241) Tenretnoel, C.; Verbist, J. J., XPS STUDIES OF COBALT(II) AND COBALT(III) MIXED OXIDES. *Abstracts of Papers of the American Chemical Society* **1979,** (SEP), 198-198.
(242) Lycourghiotis, A.; Defosse, C.; Delmon, B., XPS AND DRS INVESTIGATION OF THE EFFECT OF NA ON GAMMA-AL2O3 SUPPORTED COBALT OXIDE. *Revue De Chimie Minerale* **1979,** *16* (5), 473-476.
(243) Zhu, Y.; Zhang, S. R.; Ye, Y. C.; Zhang, X. Q.; Wang, L.; Zhu, W.; Cheng, F.; Tao, F., Catalytic Conversion of Carbon Dioxide to Methane on Ruthenium-Cobalt Bimetallic Nanocatalysts and Correlation between Surface Chemistry of Catalysts under Reaction Conditions and Catalytic Performances. *Acs Catalysis* **2012,** *2* (11), 2403-2408.
(244) Zhang, S. R.; Shan, J. J.; Zhu, Y.; Nguyen, L.; Huang, W. X.; Yoshida, H.; Takeda, S.; Tao, F., Restructuring Transition Metal Oxide Nanorods for 100% Selectivity in Reduction of Nitric Oxide with Carbon Monoxide. *Nano Letters* **2013,** *13* (7), 3310-3314.
(245) Tao, F. F.; Shan, J. J.; Nguyen, L.; Wang, Z. Y.; Zhang, S. R.; Zhang, L.; Wu, Z. L.; Huang, W. X.; Zeng, S. B.; Hu, P., Understanding complete oxidation of methane on spinel oxides at a molecular level. *Nature communications* **2015,** *6*.
(246) Liu, J. J.; Zhang, S. R.; Zhou, Y.; Fung, V.; Nguyen, L.; Jiang, D. E.; Shen, W. J.; Fan, J.; Tao, F. F., Tuning Catalytic Selectivity of Oxidative Catalysis through Deposition of Nonmetallic Atoms in Surface Lattice of Metal Oxide. *Acs Catalysis* **2016,** *6* (7), 4218-4228.